ELECTROCHEMICAL STUDY ON THE CORROSION PROTECTION BEHAVIOR OF CONDUCTING POLYMER NANOCOMPOSITES

MAGAJI LADAN

FACULTY OF SCIENCE
UNIVERSITY OF MALAYA
KUALA LUMPUR

2017

ELECTROCHEMICAL STUDY ON THE CORROSION PROTECTION BEHAVIOR OF CONDUCTING POLYMER NANOCOMPOSITES

MAGAJI LADAN

THESIS SUBMITTED IN FULFILMENT OF THE REQUIREMENTS FOR THE DEGREE OF DOCTOR OF PHILOSOPHY

DEPARTMENT OF CHEMISTRY
FACULTY OF SCIENCE
UNIVERSITY OF MALAYA
KUALA LUMPUR

2017

UNIVERSITY OF MALAYA

Original literary work declaration

Name of Candidate: **Magaji Ladan**

Matric No: **SHC140055**

Name of Degree: **Doctor of Philosophy**

Title of Thesis: **Electrochemical study on the corrosion protection behavior of conducting polymer nanocomposites**

Field of Study: **Computational Simulation and Electrochemistry**

I do solemnly and sincerely declare that:

(1) I am the sole author/writer of this Work;
(2) This Work is original;
(3) Any use of any work in which copyright exists was done by way of fair dealing and for permitted purposes and any excerpt or extract from, or reference to or reproduction of any copyright work has been disclosed expressly and sufficiently and the title of the Work and its authorship have been acknowledged in this Work;
(4) I do not have any actual knowledge nor do I ought reasonably to know that the making of this work constitutes an infringement of any copyright work;
(5) I hereby assign all and every right in the copyright to this Work to the University of Malaya ("UM"), who henceforth shall be owner of the copyright in this Work and that any reproduction or use in any form or by any means whatsoever is prohibited without the written consent of UM having been first had and obtained;
(6) I am fully aware that if in the course of making this Work I have infringed any copyright whether intentionally or otherwise, I may be subject to legal action or any other action as may be determined by UM.

Candidate's Signature Date:

Subscribed and solemnly declared before,

Witness's Signature Date:

Name:

Designation:

ABSTRACT

Corrosion is a persistent issue faced by human-made structures made from metals and metal alloys. Steel is used in many structural applications; however, it undergoes severe corrosion when exposed to corrosive media. Coatings are among the best methods to prevent metals and its alloys from the corrosion. However, traditional coating systems such as barrier coatings, metal-rich coatings, and coatings incorporating inhibitors have their setbacks. Conductive polymers such as polypyrrole and polyaniline were used for the corrosion protection of metals. Redox activity and the corrosion-inhibiting ion release ability of conducting polymers make them a good choice in place of hexavalent chromium compounds. However, conducting polymers are porous, stiff, inherent insoluble and low mechanical properties which make them inferior corrosion resistance materials. To tackle the problems associated with the conducting polymers and to harness maximum functionality out of them, conducting polymer nanocomposites (CPNs) were developed. CPNs combine conducting polymers and inorganic pigments in unique methods which exhibit excellent corrosion resistance properties. In this research, nanocomposites of polypyrrole and polyaniline were synthesized by an eco-friendly chemical oxidative polymerization. Core and shell of polyaniline and polypyrrole with titanium dioxide and graphene oxide were prepared and applied for safeguarding steel substrate from corrosion. These nanocomposites were analyzed by Fourier transform infrared spectroscopy (FTIR), X-ray diffraction (XRD), Field emission scanning electron microscopy (FESEM), energy dispersion X-ray (EDX), Raman spectroscopy, Transmission electron microscopy (TEM) and thermogravimetric analysis (TGA). The TEM results confirmed that the Co-doped TiO_2/PPy NTCs, Co-doped TiO_2/GO/PANI, and PANI/GO/Zn-doped TiO_2 nanocomposites were smaller than TiO_2/PPy NTCs, Co-doped TiO_2/PANI, and

PANI/Zn-doped TiO_2, thereby increasing the interaction between the PPy and PANI and the steel surfaces. The corrosion protection ability of the coatings was studied by electrochemical impedance spectroscopy (EIS) and potentiodynamic polarization measurements in 3.5% NaCl solution. The EIS results show that the log |Z| of steel coated with Co-doped TiO_2/PPy NTCs, Co-doped TiO_2/GO/PANI and PANI/GO/Zn-doped TiO_2 NCs reached about 8.2, 9.2 and 9.01, respectively, after 30 days of immersion in 3.5 % NaCl solution. Whereas the log |Z| values of TiO_2/PPy, Co-doped TiO_2/PANI, and PANI/Zn-doped TiO_2 NCs was around 6.0, 7.4 and 7.15, respectively, for the same immersion period. This is likely due to the increased surface areas of the PPy and PANI synthesized in the presence of Co-doped TiO_2 NPs, Zn-doped TiO_2 and GO respectively. The EIS results are confirmed by the potentiodynamic polarization and open circuit potential values of the Co-doped TiO_2/PPy, Co-doped TiO_2/PANI, and PANI/Zn-doped TiO_2 NCs, which indicated little changes between 1 to 30 days of immersion confirming the protection ability of these coatings. It is evident that the presence of Co-doped TiO_2 NPs, Zn-doped TiO_2 NPs and GO can enhance the resistance against corrosion at the steel/electrolyte interface**.**

ABSTRAK

Pengaratan adalah masalah berterusan yang dihadapi oleh struktur-struktur buatan manusia yang diperbuat daripada logam dan aloi logam. Keluli digunakan dalam banyak aplikasi struktur; walau bagaimanapun, ia mengalami pengaratan teruk apabila terdedah kepada media penghakis. Saduran adalah diantara kaedah terbaik untuk melindungi logam dan aloi daripada pengaratan. Sistem saduran tradisional seperti lapisan halangan, lapisan logam yang kaya, dan lapisan yang mengandungi perencat pengaratan mempunyai mekanisma halangan mereka sendiri. Polimer konduktif seperti polyaniline dan polypyrrole telah digunakan sebagai bahan perlindungan pengaratan logam. Aktiviti redoks dan halangan pengaratan kebolehan perlepasan ion menjadikan polimer konduktif sebagai pengganti yang baik untuk sebatian heksavalen kromium. Walau bagaimanapun, polimer konduktif adalah poros, kaku, tidak larut dengan kekuatan mekanikal yang rendah, yang menyebabkan rintangan pengaratan yang rendah. Dalam usaha untuk menangani masalah yang berkaitan dengan polimer konduktif dan untuk memanfaatkan fungsi maksimum mereka, nanokomposit polimer konduktif (NPK) telah dibangunkan. NPK menggabungkan bahan polimer konduktif dengan pigmen bukan organik di dalam kaedah unik yang mempunyai ciri-ciri yang terbaik. Dalam kajian ini, nanokomposit daripada polypyrrole dan polyaniline telah disintesis melalui kaedah pempolimeran kimia oksidatif yang mesra alam. Lapisan teras dan luar yang terdiri daripada polyaniline dan polypyrrole dengan titanium dioksida dan graphene oksida telah disediakan dan digunakan sebagai bahan perlindungan pengaratan untuk lapisan keluli. Bahan nanokomposit polimer konduktif telah dicirikan oleh pembelauan sinar-X (XRD), transformasi Fourier infra-merah spektroskopi (FTIR), medan pelepasan imbasan mikroskop elektron (FESEM), serakan tenaga sinar-X (EDX), spektroskopi Raman, transmisi elektron mikroskop (TEM), dan analisis termogravimetri (TGA). Keputusan TEM mengesahkan bahawa nanokomposit tersebut iaitu TiO_2 Co-

didopkan/PPy NTCs, Co-didopkan TiO_2/GO/PANI, dan PANI/GOZn-didopkan TiO_2 mempunyai saiz yang lebih kecil daripada TiO_2/PPy, Co-didopkan TiO_2/PANI dan PANI/Zn-didopkan TiO_2, oleh itu dapat meningkatkan interaksi antara PPy dan PANI dengan permukaan keluli AISI. Prestasi pengaratan salutan telah dinilai oleh spektroskopi impedans elektrokimia (EIS) dan ukuran polarisasi keupayaan dinamik dalam larutan 3.5% NaCl. Keputusan EIS menunjukkan bahawa log | Z | AISI 1018 keluli yang disalut dengan TiO_2 Co-didopkan/PPy NTCs, Co-didopkan TiO_2/GO/PANI dan PANI/GO/Zn-didopkan TiO_2 NCs mencapai kira-kira 8.2, 9.2 dan 9.01 masing-masing, selepas 30 hari rendaman dalam larutan 3.5% NaCl. Manakala log | Z | nilai-nilai TiO_2 / PPy, Co-didopkan TiO_2 / PANI, dan PANI/Zn-didopkan TiO_2 NCs adalah sekitar 6.0, 7.4 dan 7.15 masing-masing, untuk masa rendaman yang sama. Ini mungkin disebabkan oleh kawasan permukaan yang meningkat daripada PPy dan PANI yang disintesis dengan kehadiran Co-didopkan TiO_2 NPS, TiO_2 Zn-didopkan dan GO masing-masing. Keputusan EIS disahkan oleh polarisasi keupayaan dinamik dan nilai keupayaan litar terbuka Co-didopkan TiO_2 / PPy, Co-didopkan TiO_2 / PANI, dan PANI/Zn-didopkan TiO_2 / NCs, yang menunjukkan perubahan kecil antara 1 hingga 30 hari selepas rendaman yang mengesahkan keupayaan perlindungan lapisan ini. Adalah jelas bahawa kehadiran Co-didopkan TiO_2 NPS, Zn-didopkan TiO_2 NPS dan GO telah meningkatkan rintangan terhadap pengaratan pada permukaan keluli / elektrolit.

ACKNOWLEDGEMENTS

All thanks go to Allah, the Creator and sustainer for giving me the ability and opportunity to keep on breathing in good health up to the level I am writing my final remarks at the completion of writing this thesis.

I am deeply indebted to my revered supervisor Prof. Dr Wan Jeffrey Basirun for his constant guidance and support throughout the program. The fingerprint of his professional input in my research is conspicuously consistent with his creative traits. I sincerely appreciate the cognitive and practical guidance of my supervisor Dr Kazi Salim Newaz who, together with Prof. Dr Wan Jeffrey kept on searching for a solution to any problem I faced during my study. It is no doubt that the rare combination of these gentle, intelligent and concerned professional supervisors helped in facilitating the completion of my research on time.

My deepest gratitude goes to my Parents, for good upbringing and support from my childhood to date. My sincere thanks go to my wife and our living five children.

The unequivocal contribution of my sponsors (BUK through TETFUND) is at this moment acknowledged with appreciation. I gratefully acknowledge funding for this research project provided by the University of Malaya Postgraduate program aid with grant No PG184-2015A. The grant helped immensely in securing all the materials needed for the successful completion of this project. The psychological and professional input of fellow researchers like Dr Reza and all my labmates is acknowledged. Also, my sincere thanks go to all the staff of chemistry department.

Finally, I thank Almighty Allah for giving me life, strength, wisdom and knowledge to see to the completion of this project.

TABLE OF CONTENTS

LIST OF FIGURES

LIST OF TABLES

LIST OF SYMBOLS AND ABBREVIATIONS

An	:	Aniline
C_c	:	Capacitance of coatings
CE	:	Counter electrode
CNTs	:	Carbon nanotubes
CPE	:	Constant phase element
CPNCs	:	Conducting polymer nanocomposites
CPs	:	Conducting polymers
CR	:	Corrosion rate
DBSA	:	Dodecylbenzene sulfonic acid
DMF	:	N,N-dimethylformamide
E_{corr}	:	Corrosion potential
EDX	:	Energy dispersive X-ray analysis
EIS	:	Electrochemical impedance spectroscopy
FESEM	:	Field emission scanning electron microscopy
FRA	:	Frequency response analyzer
FT-IR	:	Fourier transform infrared spectroscopy
GO	:	Graphene oxide
GPES	:	General purpose electrochemical software
i_{corr}	:	Corrosion current density
ICPs	:	Intrinsically conducting polymers
MO	:	Methyl orange
NCs	:	Nanocomposites
NMP	:	N-methyl-2-pyrrolidone
NPs	:	Nanoparticles

NTCs	:	Nanotube composites
NTs	:	Nanotubes
OCP	:	Open circuit potential
PANI	:	Polyaniline
PPy	:	Polypyrrole
R_c	:	Resistance of Coatings
RE	:	Reference electrode
SCE	:	Saturated calomel electrode
TEM	:	Transmission electron microscopy
TGA	:	Thermogravimetric analysis
THF	:	Tetrahydrofuran
TTIP	:	Titanium tetraisopropoxide
WE	:	Working electrode
XRD	:	X-ray diffraction
Z_{im}	:	Imaginary Impedance
Z_{re}	:	Real impedance

CHAPTER 1: INTRODUCTION

1.1 Study background

Corrosion is the deterioration or oxidation of a refined metal to its original states. It is the progressive damage of materials (in most cases metals) by means of chemical reaction with their environments (Abdollahi et al., 2014). In the most regular use of the term, corrosion is the electrochemical oxidation process of steel in the presence of oxygen or sulfur. The iron oxides formation is an example of an electrochemical process of corrosion. This sort of destruction yields oxide(s) or salt(s) of the initial metal, and produces a clear orange coloration. Other materials like polymers or ceramics can also undergo corrosion, even though the term "degradation" is often used for these materials. Corrosion destroys the valuable properties of materials and structures such as appearance, strength, and porosity to the possible gases and liquid (Shaw & Kelly, 2006). Materials like ceramics contain some metals that satisfy their chemical reactivity by the bonds formed with other reactive ions, such as silicates and oxides. Therefore, these materials are considered as chemically non-reactive, and they undergo degradation by either mechanical wear or physical breakdown or sometimes by erosion. Also, plastic polymers are relatively unreactive due to their covalent bonding, mainly between carbon atoms which are considered as highly stable. In most cases, the destruction of such materials does not come under the corrosion definition.

1.2 Chemistry of corrosion

As mention earlier, the term corrosion refers to the electrochemical reaction between a metal or its alloy and the environment, leading to the gradual destruction. This corrosion reaction in an aqueous solution involves electron or charge transfer. Corrosion takes place when metals, are exposed to environments (with the presence of atmospheric oxygen). In the case of iron, the overall reaction is represented by Equation (1.1);

$$4Fe + 2H_2O + 3O_2 \rightarrow 4FeO(OH) \quad (1.1)$$

With $FeO(OH)$ being the rust deposits which is a sign of corrosion of iron. By close examination of the above reaction, it can be observed that separate reactions occur at different locations on the steel surface. Fe^{2+} Ions are being produced by the oxidation reaction of the iron metal, and the surplus electrons enter the metal. This reaction, written as;

$$Fe \rightarrow Fe^{2+} + 2e^- \quad (1.2)$$

occurs at the anodic regions. In the cathodic regions, oxygen will get reduced by accepting electrons from the metal based on Equation 1.3.

$$O_2 + 2H_2O + 2e^- \rightarrow 4OH^- \quad (1.3)$$

The above reaction is called a cathodic reaction, and the regions where it occurs is referred as cathodic regions.

Both cathodic and anodic reactions must be simultaneous to maintain the charge neutrality in the steel surface. Also, there must be electrons movement from the anodic regions to the cathodic areas; this happens via the metal. The flow of the electrons is affected by the area of more electrical resistance between the anode and cathode areas. The anodic reaction can occur at the metal surface beneath the film, the cathodic reaction at the outer surface of the film and the electron must pass through the high resistance film when going from the cathodic to anodic regions. During the corrosion process, positive ions are generated at the anodic regions, and negative ions (anions) are generated at the cathodic regions as shown Figure 1.1. Also, to achieve charge neutrality in the solution, there must be a net diffusion of cations to the cathodic areas and anions to the anodic regions. This diffusion occurs quite readily in solutions of high ionic conductivity (e.g., seawater). This is one of the reasons why metals corrode in seawater.

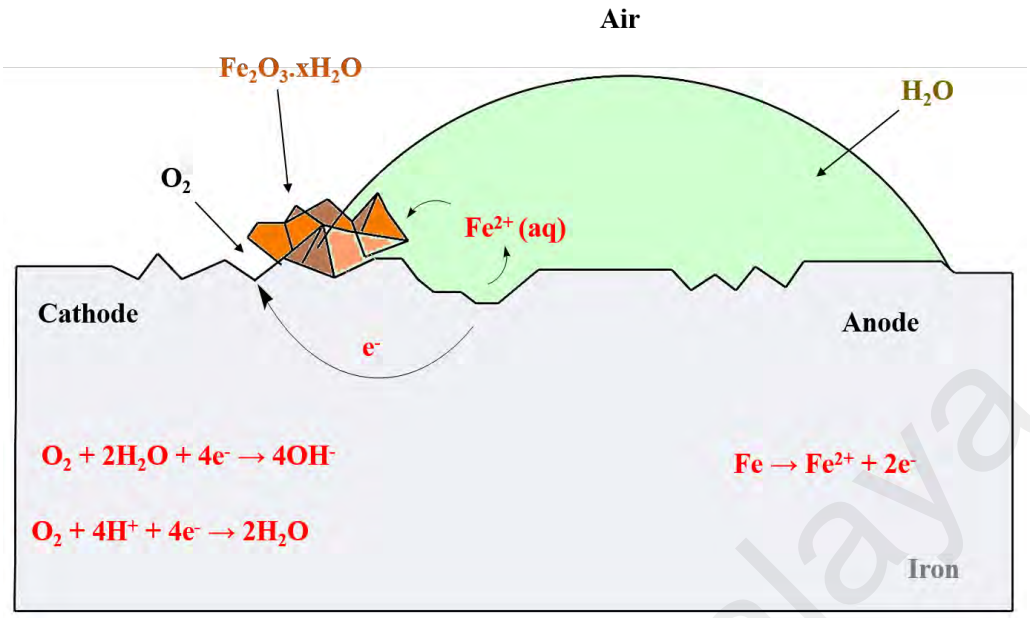

Figure 1.1: Schematic diagram of metal dissolution (iron)

Corrosion can be said to form a pit or crack locally, or it can spread through a wide area more or less reliably deteriorating the surface. Since corrosion process is a diffusion-controlled, it happens on uncovered surfaces. The previous study has estimated the cost of corrosion in the USA alone to stand at $276 billion per year (Thompson et al., 2007). The study further equates the cost to represent 3.1% out of US gross domestic product (GDP). Thus, based on economic and environmental perspective, it is of importance to invest in research on corrosion protection and minimization. Accordingly, techniques to lessen the activity of the exposed surface, such as chromate conversion and passivation, can be employed to increase the corrosion protection performance of the material (Bardal, 2007). Nonetheless, many mechanisms of corrosion are less predictable and visible in some cases.

1.3 Economic and environmental aspects of corrosion

Corrosion has huge economic and environmental effect on infrastructures worldwide like bridges, highways, chemical processing, chemical processing, oil and gas industries, as well as water and wastewater systems. The effect of corrosion cannot be

fully eliminated but can be lessened by using different methods of protection (Bardal, 2007). The direct cost of corrosion damage has been estimated to be around 3 to 4% of industrialized countries' gross national product (GNP) (Cramer & Covino, 2005; Cramer & Covino, 2006).

Based on the data available from National Association of Corrosion Engineers (NACE), the total global corrosion cost was $US 552 billion in 2001, which raised to $US 1.3 trillion in 2009 (Smith, 2009). From the estimation, about 25 – 30% of this cost could be avoided if present corrosion prevention techniques were effectively utilized (Revie, 2008). The environmental damage will be more when corrosion-related issues are ignored mostly in oil/gas industries and nuclear power plants. For instance, radiation and toxic gas spillage due to extreme pitting in nuclear power stations can put employees' wellbeing at risk (Villalobos, 2005).

1.4 Corrosion control

Previous studies have estimated the cost of corrosion in the USA to stands at around $275 billion each year representing more than 3 % of the US gross domestic product (GDP) (Koch, 2002; Thompson et al., 2007). Thus, research on corrosion protection and mitigation are critical long-term investments due to the economic and environmental concerns. Despite the existence of many corrosion prevention techniques, it is still important to develop new approaches to decrease the effect of corrosion. In the past, corrosion prevention depends widely on the use of hexavalent chromium compounds as added substances to protective coatings. However, because of the toxicity level of chromium (VI) compounds, safer alternatives have been investigated (Bai et al., 2015; Clark et al., 2002; Wei et al., 2015).

The finding of electrically conducting polymers in the past 3 to 4 decades (Li et al., 2010; Skotheim, 1997; Stenger-Smith, 1998) has been the opening point for powerful theoretical and experimental work in chemistry and physics. Recently, research on

conducting polymers, particularly aromatic ones have gained much consideration as advanced materials due to their excellent characteristics (Yavuz et al., 2005; Kim et al., 2005; Asan et al., 2005). Among these polymers, polyaniline (PANI) and polypyrrole (PPy) are the most frequently studied conducting polymers because of their excellent conductivity. Polypyrrole (PPy) and polyaniline (PANI) have been principally examined as corrosion-resistant coatings for diverse metal substrates, including steel, aluminum and copper (Chang et al., 2012; Kamaraj et al., 2010; Merisalu et al., 2015; Yuan et al., 2016b).

The chemical and electronic characteristics of the conducting polymers demonstrate many features that have not only led to new theories of chemistry and physics but have also made them potential candidates for many interesting applications including diodes, battery electrodes, sensors, and electrochromic displays (Skotherm, 1986). A standout amongst the most vital uses of these materials, which are drawing an impressive consideration, is the corrosion prevention study of metals (Schauer et al., 1998; Wei et al., 1995). The conducting properties of the polymer films solely depend on the method of preparation and parameters like synthesis temperature, electrolytes, pH of the electrolyte, deposition time, solvent, etc. (Huijs & Lang, 2000; Martins et al., 2009). Therefore, to enhance conducting properties of polymer films appropriate for a specific use, it is required to control and optimize the various synthesis parameters critically. The incorporation of functionalized protonic acid, for example, dodecyl benzene sulphonic acid (DBSA) to the polymer, prompts predominant homogeneity of the polymer films and enhances the solubility and processability (Reghu et al., 1993). Moreover, also the dispersion of conductive polymer particles in resins (Jia et al., 2003).

In recent years, polypyrrole based nanocomposites are the most utilized due to their high stability, environmentally benign and facile preparation in aqueous media (Mahmoudian et al., 2013). The polymers prepared in the vicinity of nanoparticles have

increased surface area (Mahmoudian et al., 2011b; Zeybek et al., 2015b). This increases their capability of interaction with the released ions in the process of corrosion. Recent studies on polypyrrole/TiO_2 nanocomposites as anticorrosive coatings have shown that the presence of TiO_2 can improve charge transfer resistance of coatings. The anticorrosion properties of polypyrrole nanocomposite coatings on steel is as a result of the formation of stable passive oxide layers such as α-Fe_3O_4, α-Fe_2O_3 and γ-Fe_2O_3 at the polymer-metal interface (Lenz et al., 2003).

1.5 Research objectives

The objectives of this research are as below:

1) To synthesize Co-doped TiO_2/PPy nanotube nanocomposites (NTCs) and investigate its corrosion resistance properties.
2) To chemically synthesize nanocomposites of Co-doped TiO_2/graphene oxide/polyaniline as efficient anticorrosion agent for the protection of steel
3) To prepare PANI/GO/Zn-doped TiO_2 nanocomposites and evaluate its corrosion protection abilities.

1.6 Thesis design

This thesis is divided into five chapters:

Chapter one introduces a brief history of corrosion and its process, corrosion control and the objectives of this research.

Chapter two deals with a literature review of previous and current research related to the application of nanocomposites of conducting polymers, conduction mechanisms, synthesis and mechanisms of the conductive polymers. At the end of this chapter, the application of nanotechnology in corrosion control is described.

Chapter three outlines a detailed account of the synthesis of the conducting polymers nanocomposites (Co-doped TiO_2/PPy, Co-doped TiO_2/graphene oxide/polyaniline, and

PANI/GO/Zn-doped TiO_2) as anti-corrosion agents for the protection of steel. Also, the fundamental principles of the analytical techniques used for the characterization of the synthesized nanocomposites are explained.

Chapter four presents a detailed explanation of the results obtained through characterizations and precise application of the outcomes.

Chapter five provides the conclusions of the research findings and recommendations for future studies.

CHAPTER 2: LITERATURE REVIEW

2.1 Introduction to conducting polymers

In 1977 researchers at the University of Pennsylvania startled the world by demonstrating "Conducting Polymers" simply by doping polyacetylene which then showed excellent metallic properties (Chiang et al., 1977; Shirakawa et al., 1977). The extent of excitement and interest generated by this discovery can be estimated by the research publications, which amount to thousands, during the last two decades. Since then this field of the investigation has been on the path of constant progress.

Conductive polymers are polymers that are equipped for transmitting and holding a charge because of their conjugated double bond. Conducting polymers are primarily different from redox polymers, in that they possess conjugated backbones and the monomeric units interact via the π-electron system. Although redox polymers contain electro-active centres, their backbones are not conjugated, and the polymers are non-conducting electronically.

The call for electrically conducting polymers in the hardware industries has at one time been met by utilizing high amounts of conductive powders, for example, silver, gold and graphite (at some point as high as 80 wt%) with the polymer matrix (Chan et al., 1989). However, there are many setbacks to this method which include high cost and deterioration of some of the properties of the polymer. In recent years, the ability of new intrinsically conductive polymers (ICPs) which combine high conductivity with properties such as low cost, flexibility, lightweight and processability has created keen interest among the industrial and academic researchers. Conducting polymers (ICPs) have been extensively explored as revealed by the published articles and citation data obtained.

Many ICPs exist today, and although the chemical makeup of each is quite different, the conjugation that each possess gives rise to a delocalization of electrons which upon

doping enable these organic polymers to conduct electricity (MacDiarmid, 2001). Conducting polymers (CPs) such as polyacetylene, polypyrrole, polyaniline, polythiophene (see Figure 2.1) and their derivatives, have been broadly studied due to their intrinsic conductivity, fast doping-undoping process, high charge density, facile synthesis, physical and chemical stability against many environmental factors. These exceptional properties of conducting polymers have attracted the interest of researchers (Ates, 2011; Li et al., 2009; Tripathi et al., 2006). The interests in CPs, especially PPy and PANI is due to their environmental stability, they are compatible with a variety of materials, and they can be synthesized at a lower cost with minimum resources (Kim et al., 2005; Mahmoudian et al., 2013). Thus, PPy is synthesized from a range of aqueous and non-aqueous solvents. Basically, PPy is among the few electronically conducting polymers that are synthesized in aqueous solutions (Mahmoudian et al., 2011b; Sazou et al., 2007). Polyaniline and its derivatives are usually prepared from acidic aqueous solutions, but in most cases, polythiophene is developed from organic solvents in which the monomer is soluble.

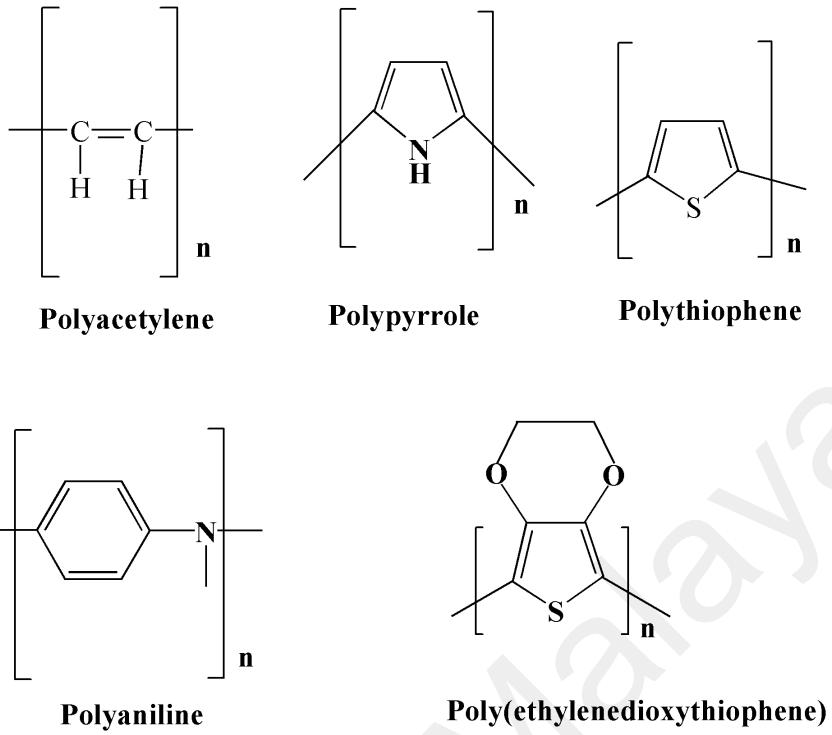

Figure 2.1: Molecular structures of some conducting polymers

2.2 Concept of doping of conducting polymers

The word doping on account of conducting polymers refers to oxidation/reduction reactions and not in the same way it is used in the inorganic semiconductors field. On a result of an inorganic semiconductor, doping is simply the incorporation of impurities into the lattice of semiconductors. Perhaps, when a small amount of five valence electrons phosphorous is added into the four valence electrons, silicon semiconductor produces one extra electron for each phosphorous atom (Deshpande & Sazou, 2016). The produced electron is allowed to travel in the conduction band of the silicon crystal at high temperature. In this case, the impurity is recognized as a donor while the semiconductor that contains the donors is termed as an n-type semiconductor. Alternatively, adding a trace amount of boron having three valence electron into the semiconductor of silicon produces one vacant electron for each boron atom, which is allowed (by thermal ionization) to travel in the valence band (VB) of the silicon crystal.

This type of impurity is known as acceptor, and therefore the semiconductors containing acceptors are termed as p-type semiconductors (Deshpande & Sazou, 2016; Sato, 1998).

On account of conducting polymers (CPs), the oxidation reaction involves the removal of electrons from the valence band (VB) and the presence of charges on the polymer conduction band. The charges are delocalized over several polymer units, causing a relaxation of the geometry of the charged polymer to a more energetically favored conformation. This oxidation process resulting in the existence of positive charges and linked anions as counterions in the polymer chain is called p-type doping. The oxidation of CPs can be illustrated in Equation (2.1).

However, the reduction of conducting polymers involves the addition of electrons to the CP conduction band, resulting in the occurrence of negative charges in the CP chain and associated cations as the counterions. This method is known as n-type doping.

$$(CP)_n + nyMClO4 \leftrightarrow [(CP)^{+y}\,(ClO_4^-)y]_n + nyM^+ + nye^- \quad (2.1)$$

$$(CP)_n + nyNaA + nye^- \leftrightarrow [(CP)^{-y}\,(Na^+)_y]_n + nyA^- \quad (2.2)$$

The terms M and A in Equations (2.1) and (2.2) represent the cation and anion, respectively.

The anions/cations inserted popularly called counter ions during the CPs oxidation/reduction are known as dopants. Counterions (dopants) can be added into the CP concurrently with the synthesis. Dopants can also be integrated at a later step or substituted by other desired counterions. The oxidizing or reducing agents can convert conjugated polymer to its salt form by the charge transfer reaction. It has been acknowledged that the inclusion of a donor or an acceptor types to the conjugated polymer rises the conductivity of the polymer by several times.

Reversible doping may be accomplished through electrochemical, chemical, interfacial, and photo processes, depending largely on the application for which conducting polymers have been synthesized to serve (Das & Prusty, 2012; Günes et al.,

2007; Janata & Josowicz, 2003; Long et al., 2011). On account of interfacial charge infusion and photo-doping, dopant ions are not involved. The nature of doping process and the chemical type of dopants establish a means for controlling the properties of conducting polymers, such as optical and redox properties, processability, environmental stability, and morphology.

Table 2.1: List of dopant used for CP with conductivity, doping method and type of doping

Conducting polymer	Dopant	Counterion	Conductivity (S/cm)	Doping method	Type of dopant	Ref.
Polyaniline	HCl	Cl^-	12	Chemical (solution)	p-type, inorganic, neutral	(Dominis et al., 2002)
Polyaniline	Tartaric acid	$C_4H_5O^-_6$	11	Chemical (solution)	p-type, organic, neutral	(Dominis et al., 2002)
Polyaniline	DBSA	DBS^-	300	Chemical (solution)	p-type, organic, neutral	(Kar, 2013)
Polyaniline	Poly(2-methoxyaniline-5-sulfonate) (PMSH)	PMS^-	13	Chemical (solution)	p-type, polymeric, neutral	(Kar, 2013)
Polyaniline	HCl	Cl^-	2.09×10^{-2}	In-situ	p-type, inorganic, neutral	(Athawale et al., 2002; Khanna et al., 2006)
Polyaniline	Acrylic acid	$C_3H_3O_2$	6.20×10^{-3}	In-situ	p-type, organic, neutral	(Athawale et al., 2002)
Polyaniline	Citric acid	$C_6H_7O_7^-$	80.43×10^{-2}	In-situ	p-type, organic, neutral	(Arasi et al., 2009; Kulkarni et al., 2004b)

Table 2.1: continued.

Conducting polymer	Dopant	Counterion	Conductivity (S/cm)	Doping method	Type of dopant	Ref.
Polyaniline	Acetic acid	CH_3COO^-	4.21×10^{-2}	In-situ	p-type, organic, neutral	(Arasi et al., 2009)
Polyaniline	HCl	Cl^-	200	In-situ	p-type, inorganic, redox	(Kumar & Sharma, 1998)
Polyaniline	Tartaric acid	$C_4H_5O^-_6$	24.53×10^{-2}	In-situ	p-type, organic, neutral	(Dominis et al., 2002)
Polyaniline	Oxalic acid	$C_2HO^-_4$	18.17	In-situ	p-type, organic, neutral	(Dominis et al., 2002)
Polyaniline	HCl	Cl^-	43.29×10^{-2}	In-situ	p-type, inorganic, neutral	(Kulkarni et al., 2004a)
Polyaniline	H_2SO_4	HSO_4^-	134.5×10^{-2}	In-situ	p-type, inorganic, neutral	(Kulkarni et al., 2004a)
Polyaniline	HNO_3	HNO_3^-	94.59×10^{-2}	In-situ	p-type, inorganic, neutral	(Kulkarni et al., 2004a)
Polyaniline	$HClO_4$	ClO_4^-	25.37	In-situ	p-type, inorganic, neutral	(Kulkarni et al., 2004a)
Polyaniline	H_3PO_4	$H_2PO_4^-$	2.14×10^{-2}	In-situ	p-type, inorganic, neutral	(Kulkarni et al., 2004a)
Polypyrrole	p-toluenesulfonic acid	Tosylate	500-7500	Electrochemical	p-type, inorganic, redox	(Kumar & Sharma, 1998)
Polypyrrole	R_4N, BF_4 or MBF_4	BF_4^-, ClO_4^-	500-7500	Electrochemical	p-type, inorganic, redox	(Kumar & Sharma, 1998)

Table 2.1: continued.

Conducting polymer	Dopant	Counterion	Conductivity (S/cm)	Doping method	Type of dopant	Ref.
Polypyrrole	p-Methylbenzene sulfonic acid (MSAH)	MSA^-	16	In-situ	p-type, organic, neutral	(Wang et al., 2001)
Polypyrrole	p-Hydroxybenzene sulfonic acid (HSAH)	HSA^-	11	In-situ	p-type, organic, neutral	(Wang et al., 2001)
Polypyrrole	p-Dodecylbenzene sulfonic acid (DBSH)	DBS^-	2	In-situ	p-type, organic, neutral	(Wang et al., 2001)
Polypyrrole	Alizarin red acid (ARH)	AR^-	8	In-situ	p-type, organic, neutral	(Wang et al., 2001)
Polypyrrole	p-Naphthalene sulfonic acid (NSH)	NS^-	18	In-situ	p-type, organic, neutral	(Wang et al., 2001)
Polypyrrole	5-n-Butyl-naphthalene sulfonic acid (BNSH)	BNS^-	0.5	In-situ	p-type, organic, neutral	(Wang et al., 2001)

Table 2.1:, continued.

Conducting polymer	Dopant	Counterion	Conductivity (S/cm)	Doping method	Type of dopant	Ref.
Polypyrrole	5-Sulfo-isophthalic sulfonic acid (SISH)	SIS^-	3	In-situ	p-type, organic, neutral	(Wang et al., 2001)
Polypyrrole	Camphor sulfonic acid (CSH)	CS^-	18	In-situ	p-type, organic, neutral	(Wang et al., 2001)
Polypyrrole	$CF_3SO_3R_4N$ or CF_3SO_3M	$CF_3SO_3^-$	150	Electrochemical	p-type, organic, redox	(MacDiarmid, 1997a)
Polypyrrole	R_4NClO_4 or $MClO_4$	ClO_4^-	10	Electrochemical	p-type, inorganic, redox	(MacDiarmid, 1997a)
Polythiophene	R_4NBF_4 or MBF_4, R_4NClO_4 or $MClO_4$, $FeCl_3$, $6H_2O$	BF_4^-, ClO_4^-, $FeCl_4^-$	1000	Electrochemical	p-type, inorganic, redox	(Kulkarni et al., 2004a; MacDiarmid, 1997a)
Polythiophene	p-toluenesulfonic acid	Tosylate	1000	Electrochemical	p-type, organic, redox	(Kumar & Sharma, 1998)

2.3 Charge transport mechanisms of conducting polymers

For the past few decades, many researchers have tried to describe the mechanism of charge carriage of various conducting polymers. However, no convincing mechanism has emerged (Singh et al., 1996; Su et al., 1980). The common features of all conducting polymers are the presence of πe^- localization in their polymer backbone. Conversely, the non-existence of well-defined conduction band and valence band edges in the forbidden gap determines the intrinsic electrical properties of these polymers by the models developed for amorphous semiconductors (Su et al., 1980). Polymers such as PPy and PTh have a nondegenerate ground state, and it has been presumed that polarons and bipolarons may be the main charge carriers in these two polymers. The transport mechanism of polarons and other defects has been extensively investigated (Mott & Davis, 2012; Su et al., 1980). The charge transport mechanism of polypyrrole family is yet to be conclusively established due to their persistent structural disorder and the fact that the electrical properties exhibit both metallic and semiconducting behavior. In PPy, one-dimensional chains of same monomer units have π-electrons, but upon polymerization, the spatial level of these electrons are influenced by a major overlap integral, and the electrons become delocalized along the polymer chain in the form of bands analogous to that of a semiconductor (Maddison & Tansley, 1992).

Band theory is one of the theories that interpret the electronic structure of materials. The principles of quantum mechanics state that electrons in an atom can only have specific or quantized energy levels. In the crystal lattice, the electronic energy of individual atoms is altered, but when the atoms are spaced closely, both valence and conductions bands are formed from the energy levels. Now, the valence and the conduction bands are presented. The electrons are usually present at an absolute temperature in the valence band which is considered to be the highest range of electron

energies. While the conduction band is the lowermost range of vacant electronic states as presented in Figure 2.3.

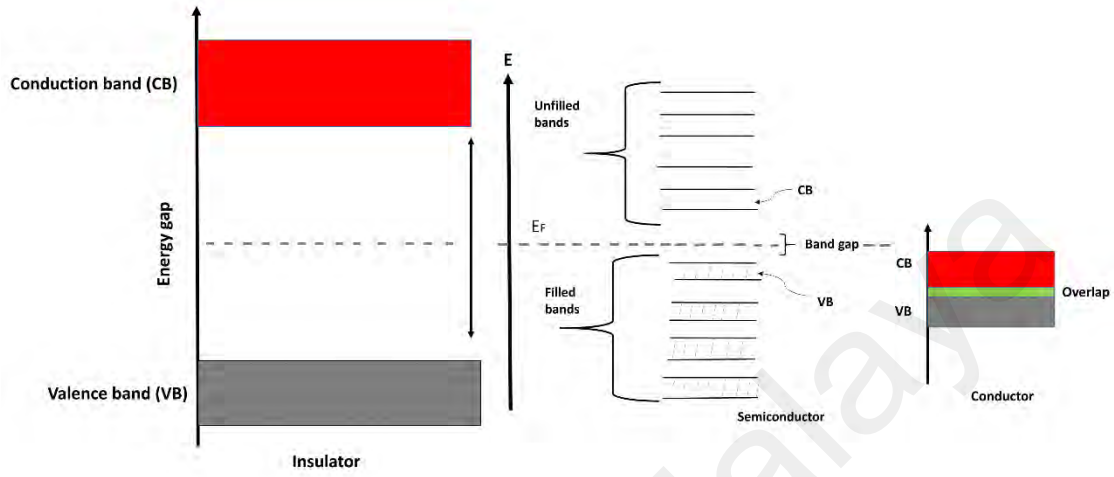

Figure 2.2: A simple schematic diagram explaining the difference between the band energies of an insulator, semiconductor and a conductor

The electronic conductivity of conducting polymers is as a result of the mobile charge carriers present in the conjugated π-system through doping.

In order to account for the electronic wonders in these organic conducting polymers, new concepts of solitons, polarons and bipolarons were proposed (Bredas & Street, 1985; Freund & Deore, 2007; Hany et al., 1989; Heeger et al., 1988; Hua et al., 2000; Ito et al., 1998; Lin & Chen, 2000). The electronic structures of π-conjugated polymers with degenerate and nondegenerate ground states are different. Solitons are the highly powerful and dominant charge storage species in π-conjugated polymers with degenerate ground states (Bredas & Street, 1985). In the field of physics, a charge related to a domain wall or a boundary is named a soliton, since it has the characteristics of a solitary wave that can move with no dissipation and deformation (Han et al., 2001). A soliton can also be observed as an excitation of the system that leads from one potential well to another one of the same energy as depicted in Figure 2.4.

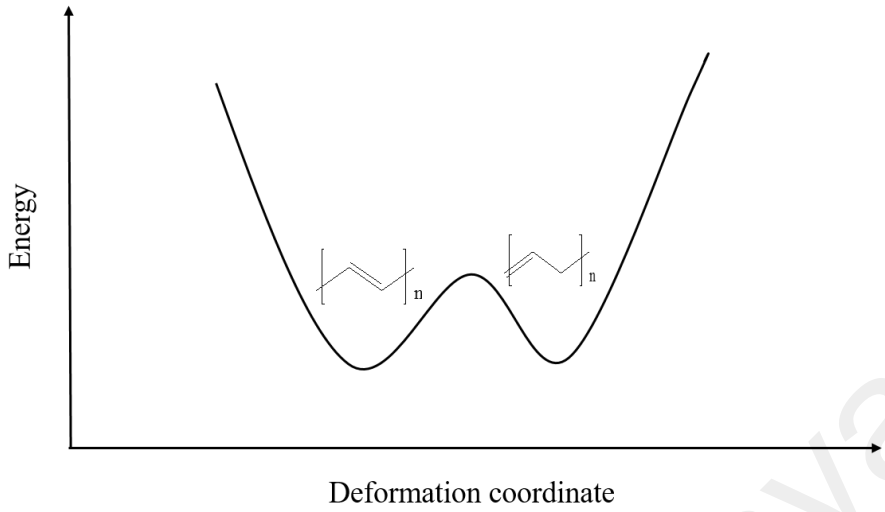

Figure 2.3: Energetically equivalent forms of degenerate polyacetylene. (Lin & Chen, 2000; Moliton & Hiorns, 2004)

A neutral soliton occurs in pristine *trans*-polyacetylene when a chain contains an odd number of conjugated carbon where there remains an unpaired π-electron, a radical, which corresponds to a soliton (Figure 2.4).

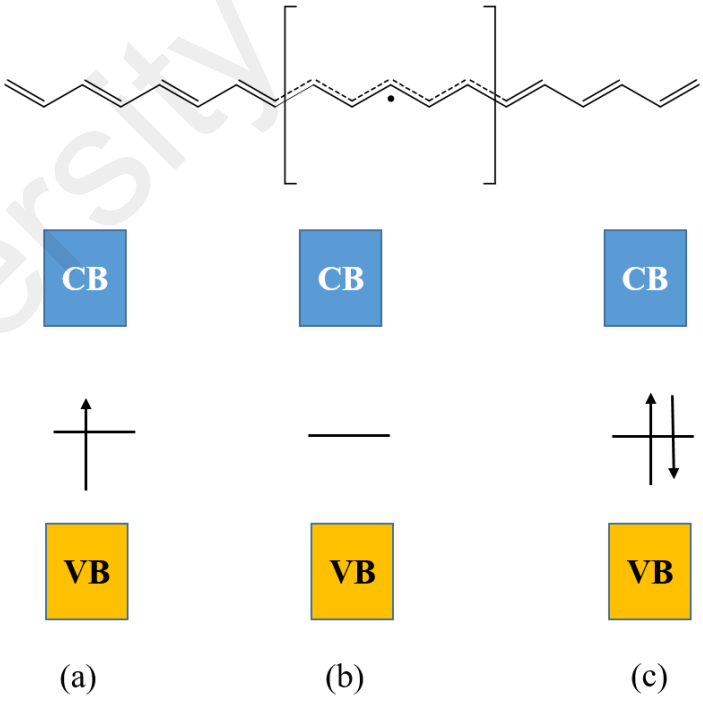

Figure 2.4: Top: a schematic illustration of the geometric structure of a neutral soliton on a trans-polyacetylene chain. Down: band structure for a trans-polyacetylene chain containing (a) a neutral soliton, (b) a positively charged soliton and (c) a negatively charged soliton. (Bredas & Street, 1985; Freund & Deore, 2007)

With the increase of chain length, the spin density in a neutral soliton is not limited to one carbon but extend over several carbons (Ito et al., 1998; Han et al., 1999; Salavagione et al., 1999). The outcome of this phenomenon is the increase of the width of the soliton. At one side of the soliton, the double bonds turn out to be step by step lengthier and the single bonds shorter, so that arriving at the other hand, the alternation has completely reversed. The effect of the presence of a soliton is the appearance of a localized electronic level at mid-gap, which the special property of the localized electronic level is partially occupied for the neutral soliton and empty (doubly occupied) for the positively/negatively charged soliton (Figure 2.5). Likewise, an n-type doping, concurrently charge-compensating cations are added into the polymer lattice when neutral chains are electrochemically or chemically changed to polycarbonium anions. In this case, the charge carriers are the less spin and negatively charged solitons.

The π-conjugated systems of polypyrrole, polythiophene, polyparaphenylene, polyparaphenylene, polyaniline and their derivatives based on their aromatic rings possess non-degenerate ground states. The ground-state degeneracy is weakly raised in these polymers so that polarons and bipolarons are the most significant and main configurations of charge storage. Figure 2.5 shows the oxidative doping of polypyrrole. A radical cation results from the removal of one electron from the π-conjugated system of polypyrrole. A polaron is introduced as a radical cation that is delocalized partially over a polymer segment. A polaron has a ½ spin so that it is a radical cation. The local charge resonance and the radical causes the radical and cation to be coupled to each other.

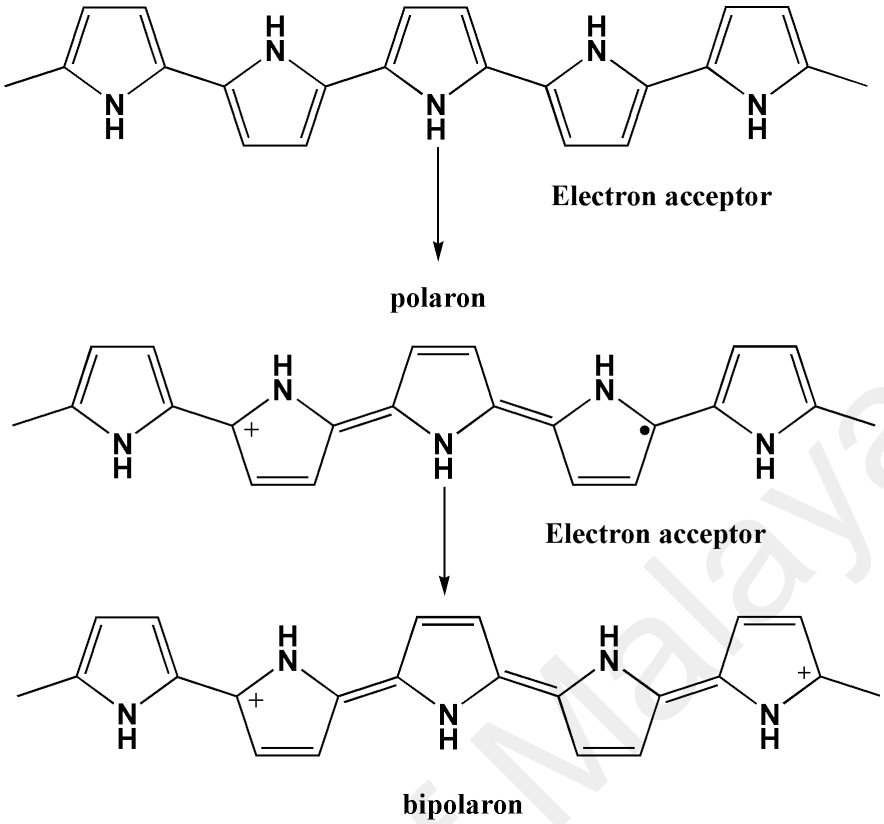

Figure 2.5: Polaron and bipolaron formation on π-conjugated backbone of polypyrrole

The existence of a polaron makes the formation of an area of quinone-type bond arrangement inside the polypyrrole chain displaying a sequence of the aromatic bond. The matrix distortion formed is of higher energy as compared to the other portion of the chain. The distortion of polypyrrole is assumed to cover more than four pyrrole rings. Beginning with oxidation, the following loss of another electron can result in two possible ways: the electron can originate from either a different part of the polymer chain hence generating another independent polaron, or from a polaron level to produce a dication splitting the area of quinone bonds from the sequence of aromatic-type bonds in the polymer chain, referred to as a bipolaron. This comes with lower energy than the formation of two different polarons. Thus, at higher doping, it is possible that two polarons can syndicate to form a bipolaron, to replace polarons with bipolarons (Varela et al., 2001, Han et al., 1994). Also, bipolarons can over four pyrrole rings. Experimental and theoretical investigations have been carried out on polyacetylene for

the evolution of the electronic and transport properties as a function of doping level (Zollinger et al., 1994; Liu et al., 1996; Planes et al., 1998; Shimizu et al., 1997), polypyrrole (Lee et al., 1997; Chan et al., 1998; Dearmitt et al., 1993; Atkinson et al., 2000), polythiophene (Atkinson et al., 2000; George et al., 2002) and polyparaphenylene (Lin et al., 2001; Atkinson et al., 2000; Wei et al., 1990).

2.4 Polypyrrole (PPy)

Amongst conducting polymers, polypyrrole is one of the prominent members, because of its promising properties such as good conductivity, environmental stability excellent thermal stability, redox nature (Wang et al., 2001). The ease of the preparation procedures and low cost of the initial monomers are also part of the interesting features of PPy (MacDiarmid, 2001). Doping and conjugated π-system due to the electrochemical and chemical methods are responsible for the conductivity showed by PPy. Doping and de-doping results in the oxidized form of PPy and the neutral form, respectively. Positive charge is balanced with the counter anion to maintain charge neutrality. Doping comes from the anion of oxidant or electrolyte used in the reaction (Gaponik et al., 2000).

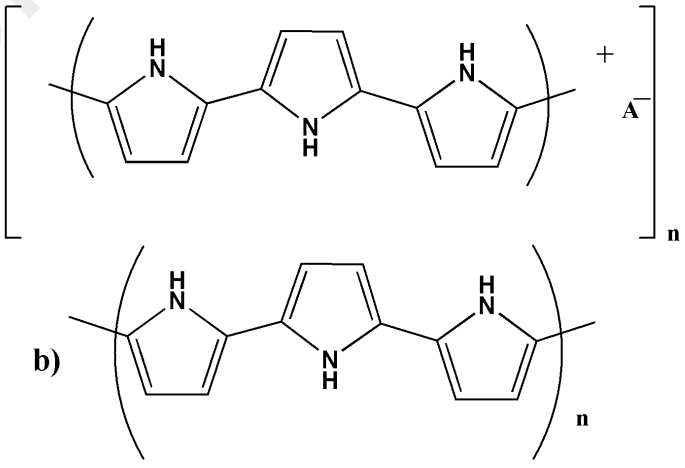

Figure 2.6: a) Oxidized form of PPy and b) neutral form of PPy

2.4.1 Synthesis of Polypyrrole (PPy)

Numerous approaches for the preparation of conducting polymers have been used. As it was mentioned before, the most frequent reaction used in synthesizing CPs is the oxidative coupling involving a cation radical formation by the oxidation of monomers followed by coupling to form dications and this repetition leads to the formation of the polymer. The conducting polymers can be synthesized by chemical oxidative (Armes, 1987) and electrochemical (Quyang et al., 1997) polymerizations. The routes of preparation and additives affect the properties of this conducting polymer (Omastova et al., 2003).

2.4.1.1 Chemical polymerization of pyrrole (PPy)

Chemical polymerization is a straightforward and fast method without any special equipment. Among the chemical oxidants used for the chemical polymerization, Iron (III) chloride was found to be the most reliable oxidant and water has been the best solvent for chemical polymerization on desirable conductivity characteristics (Machida et al., 1989). Several studies have reported the optimum reaction conditions regarding molar ratio, solvent and temperature for PPy obtained in powder or film form (Armes, 1987; Ayad, 1994a; Ayad, 1994b; Przyłuski et al., 1987). Moreover, the morphology and conductivity of PPy were also reported to depend on the synthesis conditions (Chen et al., 1995). The electrical conductivity of PPy was found to depend strongly on the pyrrole/$FeCl_3$ molar ratio and that the solvent used has a substantial consequence on the nature of the PPy aggregates that are formed. Polypyrrole powder with conductivity as high as 62 S/cm was synthesized when pyrrole was chemically oxidized with a variety of ferric salts (Walker et al., 1988). High conductivity was observed in PPy especially when strong acid anions were used as the dopant.

Throughout the chemical polymerization of PPy, the electroneutrality of the PPy matrix is sustained by the incorporation of anions from the solution. The counter ions

which are integrated into the PPy matrix are the anions from the used oxidant its reduced product. Once $FeCl_3$ or Cl_2 are utilized as the oxidants, the Cl^- ion serves as the anion. Elements like reaction time, temperature of the reaction, solvent, concentration and nature of the oxidizing agent, have effect on the oxidation potential of the solution. This oxidation potential of the solution has an impact on the conductivity of the chemically prepared polypyrrole (Machida et al., 1989; Rapi et al., 1988). Elemental analysis results have revealed that the composition of PPy prepared chemically is almost similar to the electrochemically prepared polymer (Dhawan & Trivedi, 1993).

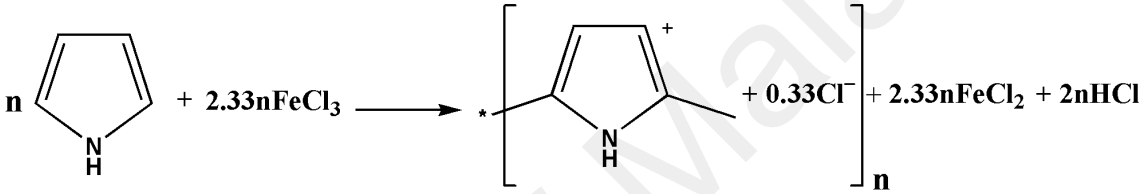

Figure 2.7: Chemical polymerization of pyrrole to polypyrrole in the presence of $FeCl_3$

2.4.1.2 Electrochemical polymerization of pyrrole (PPy)

PPy is usually prepared by an electrochemical reaction, in this process pyrrole is dissolved in a suitable solvent (medium of reaction) in the presence of an electrolyte (Gardini, 1973; Shimidzu et al., 1988; Sotzing et al., 1996). The conductive part of the PPy is created at the anode and incorporates the electrolyte as a counter ion. The synthesized polymer film properties can be monitored by changing the electrolyte, the current used in the polymerization, concentration, or temperature of the reaction. For the pyrrole polymerization, aromatic sulfonate derivatives have been frequently used as the electrolyte (Kim et al., 1995; Kuwabata et al., 1988).

It is commonly believed that the polypyrrole film electropolymerization proceed through a mechanism of electrochemically activated step growth coupling (Genies et al., 1983). The steps of the reaction are presented in Figure 2.8. The first phase of this reaction is the pyrrole monomer oxidation to form a radical cation (a), which then

combines with another radical cation or react with a neutral molecule of the monomer to form a dimer (b). This double charged dimer re-aromatizes to form a stable dimer species by losing two protons. The dimer is to some extent more easily can get oxidized than the normal monomer and may take part in the new coupling reaction of oxidation/radical to form oligomers and finally polymer (c). The polymer is not soluble in the solvent or water and usually get precipitated as a film on the electrode surface. From a mechanist perspective, there are two distinctive stages of the coupling reaction. There is the first coupling, which involves the coupling of monomers of pyrrole to yield the dimeric intermediates, and the second is the steady state coupling reaction, involving the reaction between the oligomeric intermediates and the pyrrole monomer.

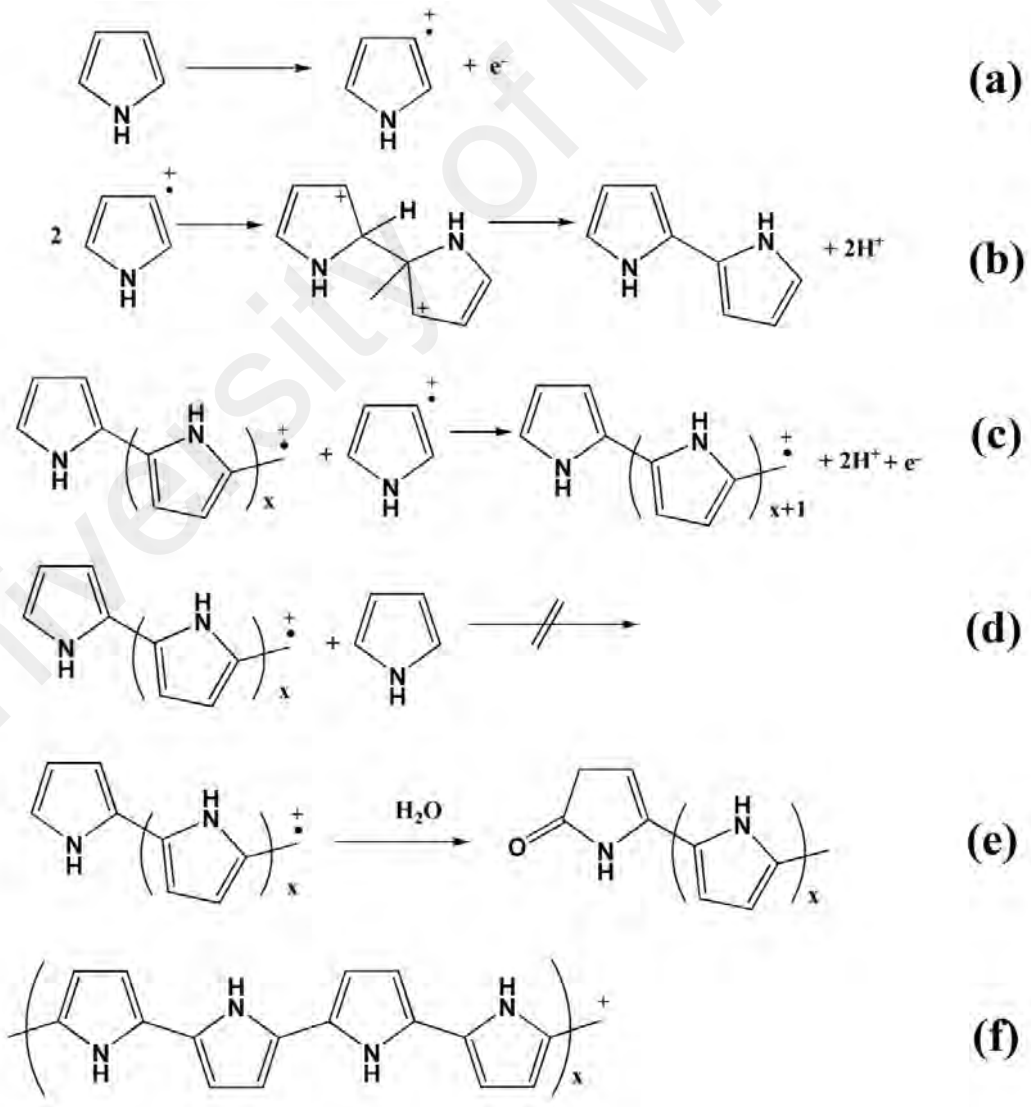

Figure 2.8: Electrochemical polymerization mechanism of polypyrrole

From the initial stage of the reaction, the radical cation formed from the coupling reaction might undergo a radical coupling with another radical to form a dimer (Figure 2.8b) or possibly it could act as electrophile which could be added to a neutral monomer (Figure 2.8d). Meanwhile, the polymerization proceeds when the potential is sufficient to oxidize the monomer, the coupling reaction must involve the coupling of two radical cations. By this continuous reaction, the polymer is generated. The additional loss of an electron, which results in a partial positive charge on the pyrrole ring (from the neutral polymer), is probably due to the further partial oxidation of the polymer. For charge neutrality in the polymer, there must be an affiliation of an anionic species which comes from the electrolyte (polyelectrolyte) salt. As revealed in Figure 2.8f, the PPy chains bear unity charge for every three to four pyrrole rings.

2.5 Polyaniline (PANI)

Polyaniline stands to be the most imperative conducting polymer due to the following reasons: i) Polyaniline is a conjugated polymer, ii) polyaniline can conduct electricity by the process of doping and iii) it is superior when compared to other conducting polymers because it can be easily synthesized by simple doping/dedoping flexibility and stability (Huang et al., 1986).

Polyaniline exists in three different oxidation states. They are leucoemeraldine, pernigraniline and emeraldine. Leucoemeraldine and pernigraniline have poor conductivity. Emeraldine form is an excellent conductor, and it may occur as salt or base forms (green or violet colour). Polyaniline has various promising and versatile applications. These applications are possible because of the special properties of polyaniline such as lightweight, conductivity, mechanical flexibility and chemical properties (Huang & Kaner, 2004). They are light-weight battery electrodes, electromagnetic shielding devices, anticorrosion coatings, and sensors (MacDiarmid, 1997).

2.5.1 Synthesis of Polyaniline (PANI)

Several techniques were described for the preparation of polyaniline using various conditions such as templates/surfactants, oxidizing agents, and solvents. Two major methods for synthesizing polyaniline are oxidative chemical polymerization and electrochemical polymerization. The chemical oxidative polymerization method was used in this research.

2.5.1.1 Chemical oxidative polymerization of aniline (PANI)

The oxidative chemical polymerization of conducting polymers seems to be a common and valuable tool for the synthesis of conductive composites and dispersed particles in aqueous media (Boeva & Sergeyev, 2014; Eisazadeh et al., 1992). Bulk amounts of polyaniline can be achieved as a fine powder using chemical polymerization of the aniline using a chemical oxidants in aqueous or non-aqueous solvents (Chao & March, 1988; Machida et al., 1989).

Even though some mechanisms have been suggested for the synthesis of polyaniline (Ćirić-Marjanović, 2013a; Ćirić-Marjanović, 2013b; Ćirić-Marjanović et al., 2008; Stejskal et al., 2010; Stejskal et al., 2008; Stejskal & Trchová, 2012), no simple technique describes the polymerization procedure. Nevertheless, there is an agreement for the common polymerization of aniline using APS as an oxidizing agent in acidic media (Figure 2.10a). As reported earlier, the aniline nitrenium cation is formed from the protonation and oxidation of aniline (first step). Head to head coupling producing benzidine dication, *para*-coupling (yielding the long-chain PANI precursor), as well as the head to tail *ortho*-coupling (producing the phenazine-like nucleates) have been reported. The ratios of one coupling type over the other is determined by the aniline/oxidant molar ratio, aniline-oxidant concentration, temperature, and the acidity of the reaction medium (Ćirić-Marjanović, 2013a; Ćirić-Marjanović et al., 2008; do Nascimento & Temperini, 2008; Stejskal et al., 2008; Stejskal & Trchová, 2012). Ferric

chloride has been reported to be the best oxidant for chemical polymerization on desirable conductivity characteristics (Machida et al., 1989). Figure 2.10b shows the overall stoichiometry of the chemical polymerization of polyaniline with ferric chloride as the oxidant.

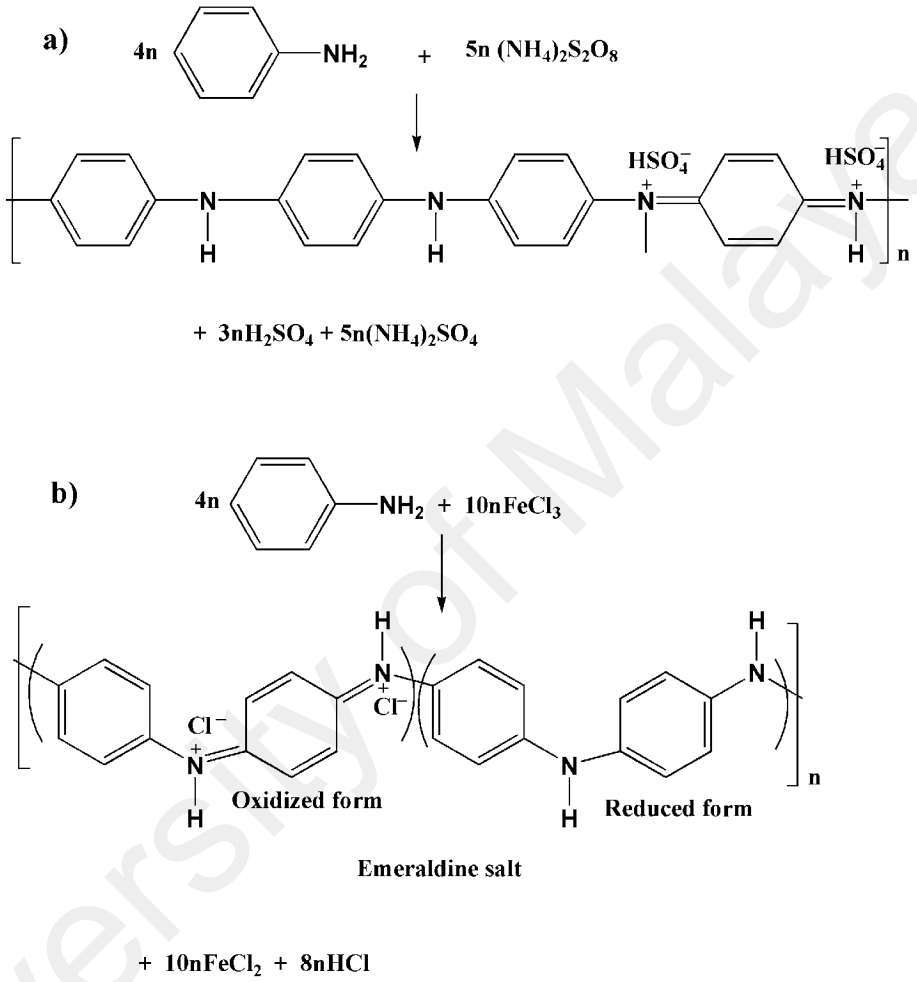

Figure 2.9: General chemical polymerization of aniline a) with APS and b) with Ferric Chloride

2.5.1.2 Electrochemical polymerization of aniline (PANI)

As mentioned earlier, the electrochemical polymerization is usually achieved by potentiostatic or galvanostatic methods. This technique is simple to explain quantitatively, and it has frequently been applied to study the nucleation mechanism and the macroscopic growth (Wei et al., 1989). Potentiodynamic techniques like cyclic voltammetry correspond to a repetitive triangular potential waveform applied to the

surface of the electrode. The latter method has been primarily utilized to get qualitative information as regards to the redox processes of the early stages of the polymerization, and also to study the electrochemical behavior of the polymer film after the synthesis.

Coulometry and chronoamperometry that measures the amount of electricity involved in the oxidation process and the current as a function of time respectively are other electrochemical techniques used for polymerization. The chronoamperometry method is useful for studying the polymerization kinetics and in particular first steps (Li et al., 2009). The commonly accepted mechanism for the aniline electrochemical polymerization is shown below where the formation of the radical cation of aniline by oxidation on the electrode surface is taken as the rate-determining step (Drobny, 2012).

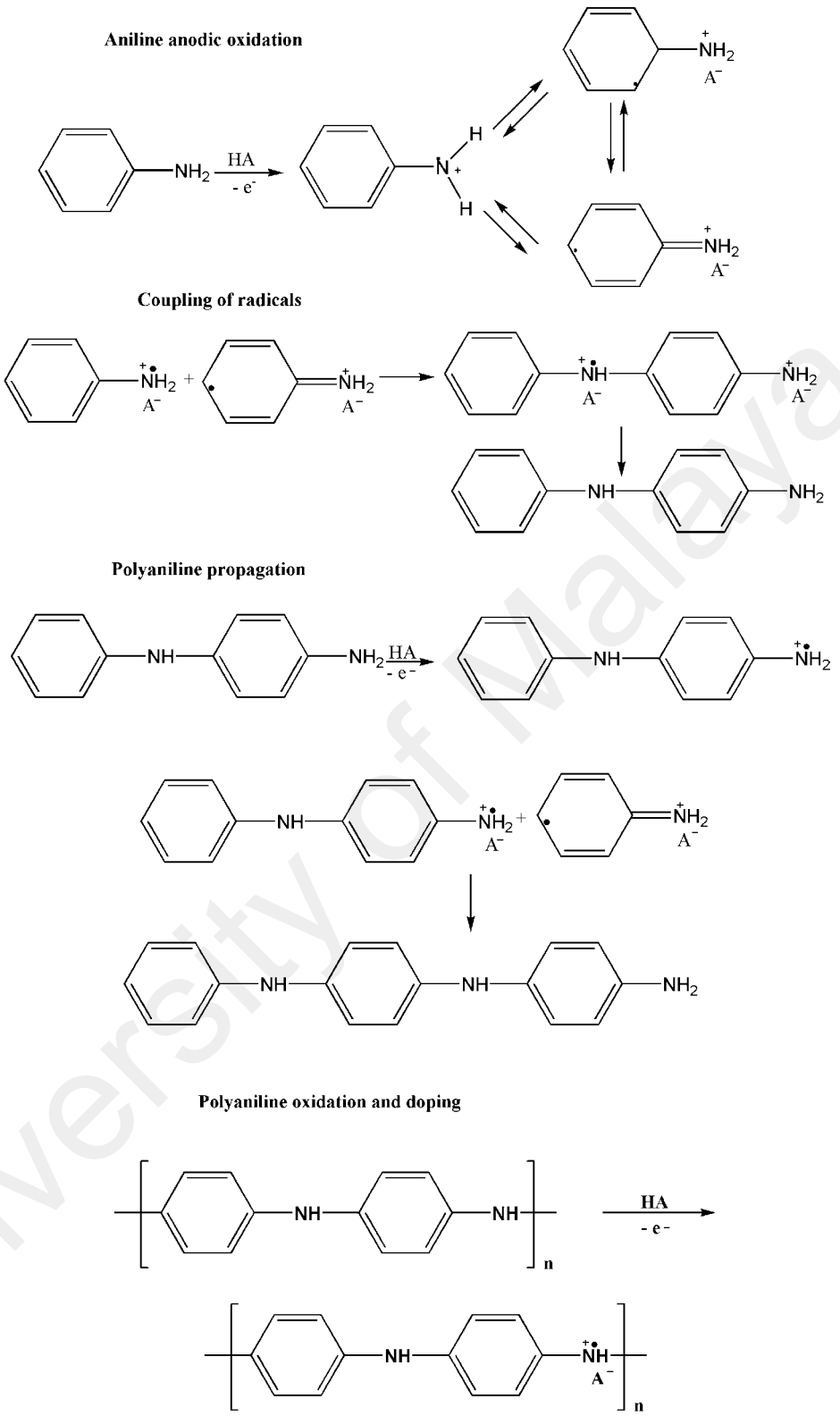

Figure 2.10: Schematic presentation of mechanism of electrochemical polymerization of aniline

2.6 Titanium dioxide nanoparticles (TiO_2 NPs)

Titanium dioxide (TiO_2) is extracted from a variety of naturally occurring ores that contain rutile, anatase, ilmenite and leucoxene. Nevertheless, most of the TiO_2 pigment in the industry is produced from titanium mineral concentrates by the so-called chloride or sulfate process (Khataee & Kasiri, 2010; Zallen & Moret, 2006). These result in different forms of TiO_2 (anatase, rutile and brookite) (Khataee & Mansoori, 2011). TiO_2 crystal can exist in the form of anatase, rutile or brookite (see Table 2.2). TiO_2 has a broad range of application since its commercial production in the early twentieth century. TiO_2 nanoparticles have been applied as additives (in paints and some cosmetic products), as an anti-corrosive coating, as an optical coating, in ceramics. It has also been utilized in heterogeneous catalysis, as a photocatalyst, in solar cells for the production of hydrogen and electric energy, as gas sensor and in electric devices such as visitors.

Table 2.2: Crystallographic properties of anatase, rutile and brookite (Diebold, 2003; Khataee, 2009; Khataee & Mansoori, 2011)

Crystal structure	Density (kg/m^3)	System	Cell parameters (nm)		
			a	b	c
Anatase	3830	Tetragonal	0.3758		0.9514
Rutile	4240	Tetragonal	0.4584		0.2953
Brookite	4170	Rhombohedral	0.9166	0.5436	0.5135

X–ray Diffraction (XRD) method is employed to determine the crystal structure and crystal grain size of anatase, rutile and brookite. In the XRD, anatase peaks appear usually at θ=12.65°, 18.9° and 24.054°; the brookite peaks occur at θ=13.75°, 18.1° and 27.2° while rutile peaks are found at θ=12.65°, 12.85°, 15.4° and 18.1°. The θ parameter represents the X–ray diffraction angle (Khataee, 2009; Mansoori et al., 2008; Moret et al., 2000).

2.6.1 Synthesis of TiO_2 NPs

The crystal sizes and crystal structures of TiO_2 mostly rely on the synthesis parameters such as the solvent, acidity, temperature, additives and aging during the preparation processes. Here, three different techniques are briefly highlighted viz: sol-gel, Solvothermal, and hydrothermal techniques.

2.6.1.1 Sol-gel method

The sol-gel technique is built on inorganic polymerization reactions. It involves four stages: polycondensation; hydrolysis; thermal decomposition and drying. The hydrolysis of metal or non-metal alkoxides sources happens in the presence of water or alcohols. Also, acid or base (e.g., glacial acetic acid) helps in the hydrolysis precursor. The solvent is removed after condensation of the solution to a gel form.

Calcination using furnace at higher temperature is needed to achieve decomposition of the organic precursor. Figure 2.12 shows the synthesis process. The sol particle size depends on the composition of the solution, temperature and probably the pH of the solution. When the above factors are controlled, the particle size can also be controlled (Burda et al., 2005; Gupta & Tripathi, 2012). The major advantages of the sol-gel technique are: i) product homogeneity, ii) solution preparation and gel processing at ambient temperature, iii) facile way of preparing multi-component materials, iv) low sintering temperature, and v) powder particle size and shape control, as well as size distribution (Ganguli, 1992).

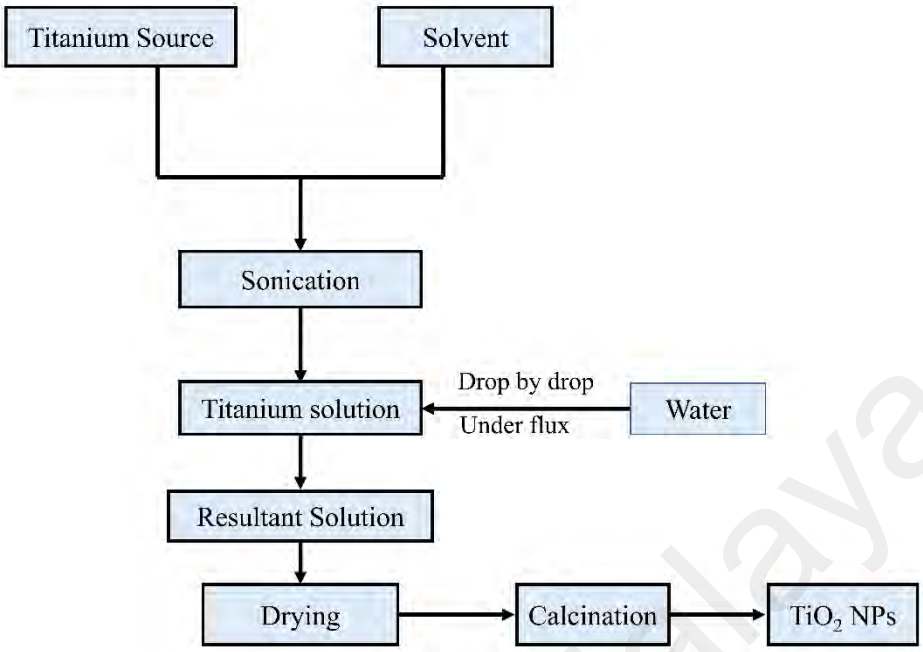

Figure 2.11: Schematic diagram of sol-gel technique for the preparation of TiO_2 NPs

The sol-gel technique is a useful technique for the preparation of doped nanoparticles with the improved surface area. The addition of a metal ion in the solution during the gelation allows the cations to be incorporated into the lattice of the nanoparticle uniformly (Bhattacharyya et al., 2008; Wu & Chen, 2004). Therefore, metal ions such as Cu^{2+}, Ni^{2+}, Sn^{4+}, Co^{2+}, Zn^{2+}, Pt^{4+}, Pb^{2+}, Au^{3+}, Zr^{2+}, Ag^{+}, Ca^{2+},Sr^{2+}, Ba^{2+} and Mn^{2+} (Binitha et al., 2010; Di Paola et al., 2002; Kolen'ko et al., 2005; Ladan et al., 2017; Mahmoudian et al., 2011a; Mahmoudian et al., 2011b; Navío et al., 1999; Sonawane et al., 2004; Stir et al., 2003; Tseng et al., 2002; Tseng et al., 2004) were incorporated into the lattice of TiO_2 powders and films by this technique. Wang et al., (2005) reported the synthesis of Fe-doped TiO_2 that uniform distribution of the dopant ions on TiO_2 particles was obtained by the complete hydrolysis of a mixture (homogeneous) of organic titanium and organic iron sources (Fe (III)-acetylacetonate) in isopropyl alcohol.

2.6.1.2 Hydrothermal Technique

The hydrothermal technique involves water as both a catalyst and occasionally as a component of solid phases at elevated temperature (>100°C) and pressure (1 atmosphere to several kilobars) (Sōmiya & Roy, 2000). It is an interesting method to produce homogeneous and highly monodispersed NPs and to yield nanocomposite materials (Byrappa & Adschiri, 2007; Chen & Mao, 2007). Many authors have studied the hydrothermal preparation of TiO_2 NPs and the effect of many parameters such as pH, experimental duration, pressure, type of solvent, temperature, and the starting charge on the product. The synthesis of TiO_2 is usually performed in autoclaves provided with Teflon liners. The synthesis conditions for the TiO_2 particles are $P < 100$ bars and $T \leq 200$ °C. The Teflon liners help to obtain pure and homogeneous TiO_2 particles (Byrappa et al., 2000).

Qian et al., (1993) reported the synthesis of ultrafine powders of TiO_2 by hydrothermal H_2O_2 oxidation starting from metallic Ti. This is achieved in two stages: a) oxidation of Ti with an aqueous solution of H_2O_2 and NH_3 to form a gel (TiO_2, H_2O) and b) hydrothermal treatment of gel under various conditions. It is expressed as follows (Gupta & Tripathi, 2012):

$$Ti + H_2O_2 \rightarrow TiO_4^{2-} + 4H_2O \quad (2.3)$$

Oxidation step

$$TiO_4^{2-} + 2(x+1)H_2O \rightarrow 2TiO_2.xH_2O + O_2 + 4OH^- \quad (2.4)$$

Heating step

$$TiO_2.xH_2O \rightarrow TiO_2 + xH_2O \quad (2.5)$$

Hydrothermal treatment

Hydrothermal has been found to be the most convenient technique for the synthesis of TiO_2 nanofibers/nanotubes (Kim et al., 2006; Lee et al., 2014; Liu et al., 2014; Wong et al., 2011). The sodium titanate nanotubes were prepared by the hydrothermal

technique by using Degussa P25 powders at a 10 M NaOH, a reaction temperature of 150, and reaction time of 48 h (Kim et al., 2006). The resulting product was free from any leftovers of Degussa P25 NPs and the nanotubes obtained had a very smooth morphology with no bundle-like structures. Yan et al. (2010a) reported a simple ethanol-induced preparation of TiO_2 nanotubes (rutile) by hydrothermal requiring no moulds or templates for repetition. The preparation was done in ethanol-water solution using the nanoparticles of TiO_2 with both anatase and rutile phase as a precursor. The anatase to rutile phase transformation was achieved by the ethanol chelating role to the TiO_6. They also found out that the ethanol-water ratio and the type of alcohol have a significant influence on the shape and phase structure of the products.

2.6.1.3 Solvothermal technique

The solvothermal technique is nearly the same with the hydrothermal technique except that the solvents are non-aqueous solvents (Chen & Mao, 2007). Equally, the temperature can be elevated much higher than that in the hydrothermal method, since the selection of a variety of organic solvents with high boiling points can easily be achieved. The solvothermal method normally has better control than hydrothermal methods of the size and shape distributions and the crystallinity of the TiO_2 nanoparticles. The solvothermal technique has been found to be a useful technique for the preparation of various types of nanoparticles with small size distribution and dispersion (Li et al., 2006; Wen et al., 2005a; Wen et al., 2005b).

The solvothermal technique has been used to prepare TiO_2 NPs and with or without the utilization of the template (Li et al., 2006; Wang et al., 2005; Wen et al., 2005a; Wu et al., 2005; Yang & Gao, 2006). Kim et al. (2003) synthesized TiO_2 by mixing titanium tetra-isopropoxide (TTIP) with toluene at the weight ratio of 1-3:10 and kept at the relatively high temperature for 3 h. The TiO_2 average particle size increases with increase in the composition of TTIP in the solution of the weight ratio of 1-3: 10 (Kim

et al., 2003). By controlling the hydrolysis reaction of TTIP and linoleic acid, re-dispersible TiO_2 NPs and nano-rods could be prepared (Li et al., 2006). The NH_4HCO_3 decomposition could provide H_2O for the reaction of hydrolysis, and linoleic acid might act as the solvent/reagent as well as coordination surfactant in the synthesis of nanoparticles. Triethylamine could serve as a catalyst for the Ti-O-Ti inorganic network polycondensation to get a crystalline product without much influence on the morphology products. The formation of TiO_2 is greatly affected by the chain lengths of the carboxylic acids, and long-chain organic acids were essential and needed in the formation of TiO_2 (Li et al., 2006). Figure 2.13 shows the TEM image of synthesized TiO_2 NPs (Li et al., 2006).

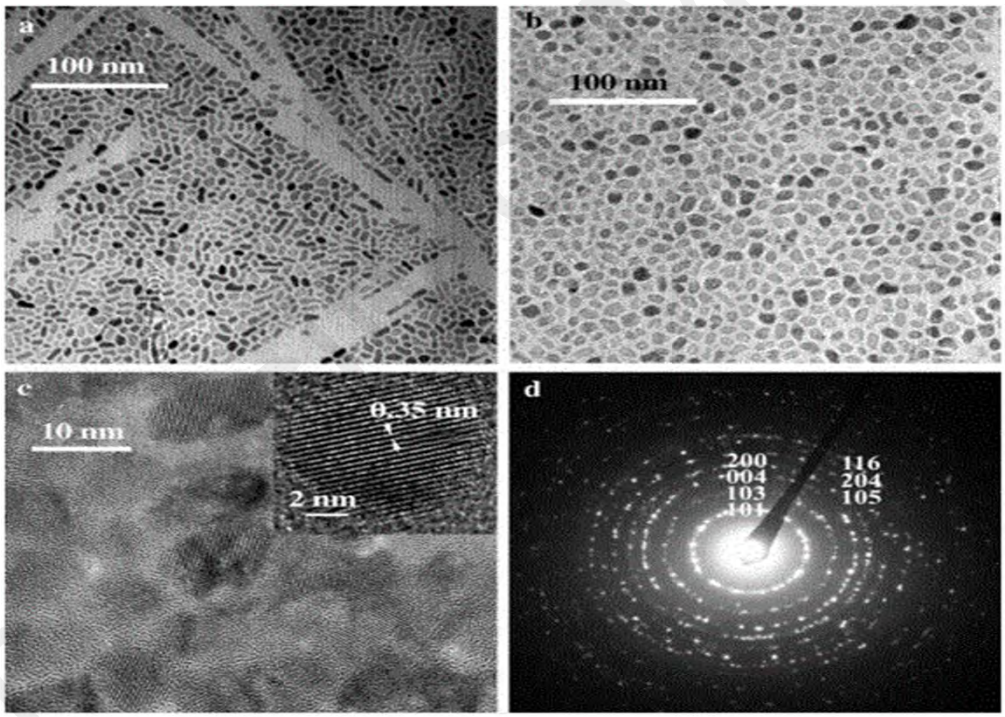

Figure 2.12: TEM images of TiO_2 nanoparticles: a,b) TEM images at different magnification, c) HRTEM image of TiO_2 nanoparticles (inset is an enlarged HRTEM image of an individual spherical particle; the lattice fringes are about 0.35 nm), and d) SAED pattern of TiO_2 nanoparticles (Reprinted with permission from Li, X. L., Peng, Q., Yi, J. X., Wang, X., & Li, Y. D. *Chemistry-a Eur J. 12*(8), 2383-2391. Copyright 2006 Wiley-VCH

2.7 Graphene oxide (GO)

Graphene oxide (GO) is a compound containing hydrogen, carbon and oxygen in different ratios with a near single-atomic-layer which is usually synthesized by exfoliation of graphite with strong oxidizers. The bulk product is a brownish/yellowish solid material that holds the layer structure of graphite with larger and irregular spacing. GO does not require further functionalization as it can be structurally visualized as a graphene sheet with its basal plane decorated by many oxygen-rich groups such as carboxyl, hydroxyl and epoxide groups (Figure 2.14). Because of the high affinity to H_2O molecules by these functional groups, GO is hydrophilic and hence can be dissolved and dispersed in THF, DI H_2O, NMP, DMF, and many other solvents that behave in the same way with H_2O. GO is a poor conductor. However, its treatment by heat, light, or reduction by the chemical method can restore most properties of the well-known pristine graphene (Dreyer et al., 2010; Hu et al., 2010; Kim et al., 2010).

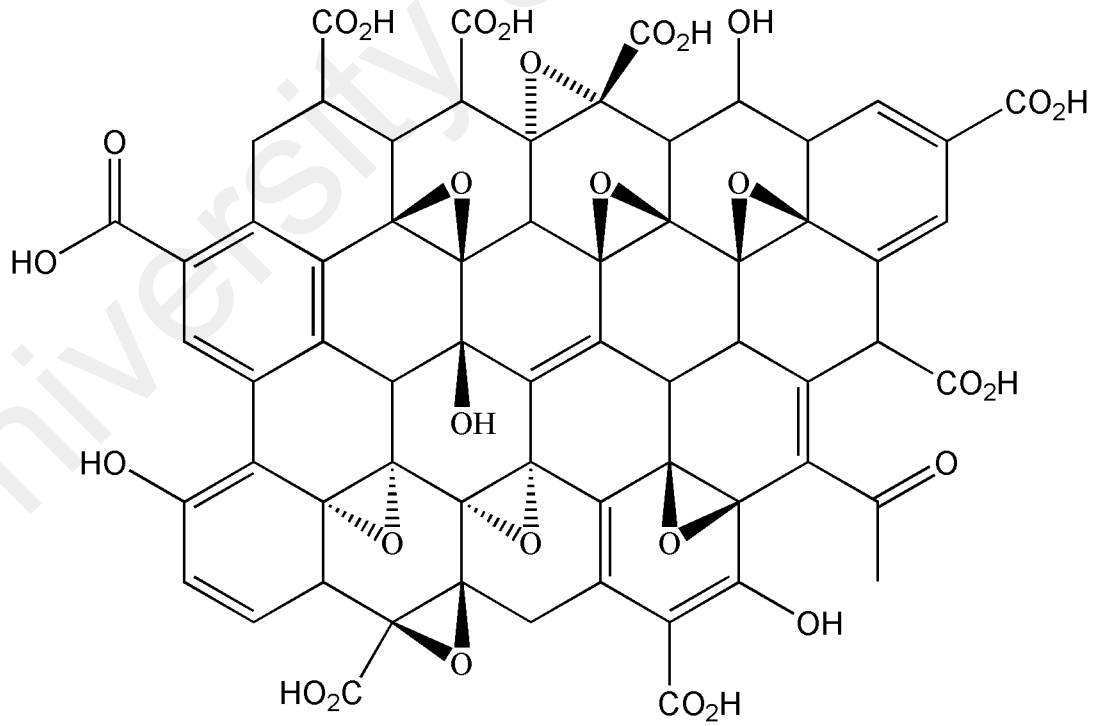

Figure 2.13: GO structure with no minor groups (carbonyl, carboxyl, ester, etc.) on the edge of the carbon plane of the graphite platelets of GO (Pei & Cheng, 2012)

2.7.1 Synthesis of GO

Presently, chemical transformation of graphite to GO has appeared to be a possible route to afford graphene-based single sheets in reasonable quantities (Geim & Novoselov, 2007; Park & Ruoff, 2009; Singh et al., 2011; Zhu et al., 2010b). GO is usually prepared according to the Hummers' method by the oxidation of graphite using oxidants such as concentrated nitric acid, sulfuric acid and potassium permanganate (Hummers & Offeman, 1958). When compared to pristine graphite, GO is deeply oxygenated having epoxy and hydroxyl groups on the sp^3 hybridized carbon on the basal plane, beside the carbonyl and carboxyl groups located at the sheet edges on the sp^2 hybridized carbon. Thus, GO is highly hydrophilic and freely exfoliated in H_2O, yielding stable dispersion comprising mostly of single-layered sheets (GO). Although graphite oxide and graphene oxide share similar chemical properties (i.e., surface functional group), their structures are different. GO is a single layer material prepared by the exfoliation of graphite oxide. Adequately dilute colloidal suspension of GO prepared by sonication are clear, homogeneous and stable indefinitely. A good level of exfoliation of GO was achieved in solvents such as tetrahydrofuran (THF), N, N-dimethylformamide (DMF), ethylene glycol and N-methyl-2-pyrrolidone (NMP) (Paredes et al., 2008). The surface charges on GO are highly negative when dispersed in H_2O (by measuring the zeta potential) because of the ionization of the carboxylic acid and the phenolic hydroxyl groups (Li et al., 2008). So, the stable graphene oxide colloids formation in H_2O is due to not only its hydrophilicity but also to the electrostatic repulsion.

The chemical structure of GO such as the nature and distribution of oxygen-containing functional groups have been investigated (Cai et al., 2008; Gao et al., 2009). The basal plane of the GO sheet is decorated with epoxy and hydroxyl functional groups with less amount of lactol ester, acid and ketone carbonyl groups at the edge. These

functional groups provide reactive sites for a variety of surface modification reactions to develop functionalized GO and graphene-based materials.

2.8 Conducting polymer nanocomposites

Conducting polymer nanocomposites (CPNCs) show a class of hybrid materials in which different inorganic particles are incorporated into the conducting polymers in some chemical or electrochemical techniques. These materials not just consolidate the current properties of the parent constituents into a solitary material, yet they additionally make powerful strides in solving the inherent processing issues of the CPs. Contingent on the characteristics of the inorganic component, various outstanding specific properties such as environmental stability, solubility, mechanical susceptibility, electrochromic properties, catalytic activity, etc., have been incorporated into the prepared nanocomposites and based on these physical properties outstanding applications are designed. In CPNCs, the NPs offer the system with some processing properties (colloidal stability or mechanical strength).

Nanocomposites are classified into two categories due to the nature of the interaction between the organic and inorganic components: one in which the inorganic particle is inserted in the organic matrix and the other where organic polymer is confined into the inorganic template. In any case, the composite formation requests some encapsulation (as shown in Figure 2.14) rather than direct blending or mixing. Nanocomposites of CPs not just scaffold the globe of microparticles with that of the macromolecules, but also makes fruitful steps toward overcoming the processing issues of CPs (Gangopadhyay & De, 2000).

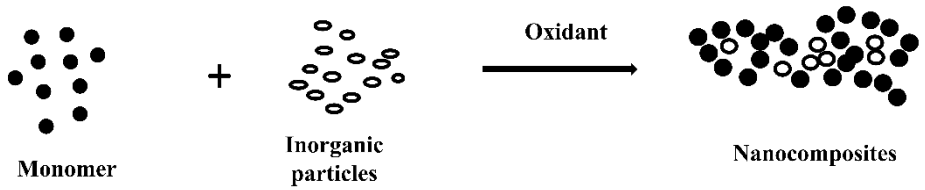

Figure 2.14: Schematic formation of conducting polymer nanocomposites from the constituents

2.9 Conducting polymer nanocomposites for corrosion protection

The alternatives to chromate coatings are currently the industrial standard of corrosion protection of aluminum alloys (Abbas & Khedr, 1995; Cohen, 1995). The highly toxic and carcinogenic properties of chromium (VI) compounds pose a grave danger to the environment. In 1998 the environmental protection agency passed the regulations on the final removal of all chromate based conversion coatings used for corrosion protection of aluminum alloys (Twite & Bierwagen, 1998). There has been active research on replacement coatings for chromate conversion coatings (Hurd et al., 1995). Conducting polymer-based coatings have been thought to be very promising as anti-corrosion coatings for aluminum alloys (Han & Elsenbaumer, 1989; Troch-Nagels et al., 1992). Conducting polymer coatings provide corrosion protection through the electroactive galvanic coupling mechanism. The electroactive polymers present at the surface of the metal can keep the exposed metal surface at a more positive potential than if no conductive pathway were available (Racicot et al., 1995; Racicot et al., 1997; Wessling, 1994). The electroactivity of the conducting polymer is the key in corrosion protection. In the case of the polyaniline-based conductive coatings, only the green emeraldine structure possesses the corrosion protection ability. The pure polyaniline based coating suffers from poor material stability, lack of processability and difficulties in direct application onto the metal surfaces as paints (Chen & Lin, 1995; Kogan et al., 1994; Noufi et al., 1982; Passiniemi & Väkiparta, 1995; Wang et al., 1995). The improvement of the double strand conducting polymer has solved some of the stability

and processability problems of pure polyaniline. The strongly bonded polymeric dopants make the polymer very stable both thermally (up to 290 °C) and environmentally (Li et al., 2013a; Liu et al., 1992; Liu & Yang, 1991).

As mentioned earlier, conducting polymers exhibit attractive properties such as excellent electrical conductivity, ease of preparation by chemical and electrochemical polymerization methods, good thermal stability and environmentally friendly nature (Castagno et al., 2009; Sabouri et al., 2009). However, there are numerous drawbacks as per as use in coatings is concerned. Conducting polymers are insoluble in most commonly used solvents in coatings. They also reveal porosity and poor to control adhesion to the steel surface (Jadhav et al., 2015; Jadhav et al., 2013). Different types of approaches have been explored to solve the problems related with CPs. These include chemical modification of CP monomers to make them soluble. Dopant ion solutions, as well as the use of composites of CPs, nanocomposites of CPs, bilayer's and multilayer's of CPs, copolymers of CPs, are some of the promising ways attempted by researchers recently.

Numerous mechanisms have been suggested for the corrosion protection of metals by conducting polymers (Breslin et al., 2005; Spinks et al., 2002; Tallman et al., 2002). The proposed mechanisms for the corrosion protection of polyaniline are barrier effects, as corrosion inhibitors, anodic protection, and corrosion inhibiting dopant release, a shift in corrosion potential, and inhibition of the diffusion rates and healing in pinholes. The proposed mechanisms for the corrosion protection as in the case of PPy are anodic protection, ennobling, passivation and corrosion inhibiting dopant release (Spinks et al., 2002).

One of the effective approaches to tackling the shortcomings mentioned above is to consider conducting polymer-based composite systems containing a conducting polymer in which different inorganic fillers such as metal oxides have been

encapsulated. Several researchers have exploited the possibility of using composite materials based on conducting polymers as anticorrosive coatings. Composites combine the functional properties of diverse materials imparting better properties for corrosion protection of metals and their alloys. Metal oxides particles or nanoparticles, as well as carbon nanomaterials such as graphene, can be incorporated into the matrix of a conducting polymer to form conducting polymer-based composites (Deshpande et al., 2014). These conducting polymer-based composites syndicate the redox properties and thus the self-healing feature of CP with qualities of inorganic materials (Deshpande et al., 2014). Therefore, conducting polymer-based composites have shown better mechanical and physicochemical properties improving the barrier effect, adhesion and perhaps hydrophobicity. The more these properties are improved, the better the metal is protected against corrosion. Furthermore, the design and development of CP-based coating systems with commercial viability is expected to be advanced with nanotechnology (Ćirić-Marjanović, 2010), which has received substantial attention recently. Nanocomposite CP-based coatings seem to combine more efficiently the properties of CPs and organic polymers to that of inorganic materials. (Bhandari et al., 2012). In this thesis, PPy NCs and PANI NCs have been used as anticorrosive agents for the protection of steel.

2.9.1 Polypyrrole nanocomposites (PPy NCs) for corrosion protection

Polypyrrole nanocomposites are obtained by the incorporation of other materials into the polypyrrole matrix. These materials are inorganic, carbon nanotubes (CNTs), graphene, etc. The inclusion of nanocomposites of PPy and inorganic pigment into coatings is an excellent technique for solving the setbacks of PPy used in the coatings (Qi et al., 2008). A mixture of these inorganic materials with PPy could impart the properties of both the PPy and the incorporated inorganic materials for a synergistic effect. PPy and inorganic materials composites have been prepared for anti-corrosion

study of steel by electrochemical methods (Hosseini et al., 2011; Yan et al., 2010b). A composite of titanium dioxide (TiO_2) and PPy (TiO_2/PPy) was synthesized via an electrochemical technique on AISI 1010 steel. Moreover, it was established that the presence of the TiO_2 nanoparticle (NP) into the PPy matrix at 6.5 wt% results in a slight improvement in corrosion prevention (Ferreira et al., 2001). It was reported that the presence of TiO_2 did not affect the polymerization process of pyrrole in the electrochemical polymerization on the mild steel surface (Lenz et al., 2003). PPy/Sn-doped TiO_2 nanocomposite was synthesized via chemical oxidative polymerization of pyrrole using $(NH_4)_2S_2O_8$ as an oxidant (Mahmoudian et al., 2011c). They reported that the Sn-doped TiO_2 NPs had a nucleus effect and caused a homogenous PPy core-shell type morphology which is leading to the coverage of Sn-doped TiO_2 NPs by the PPy deposit. After that, 1 wt% of it was incorporated into epoxy resin coating formulation and coated on the surface of mild steel (Mahmoudian et al., 2011c). In the same way, PPy/Ni-doped TiO_2 nanocomposite was synthesized and reported that the presence of Ni-doped TiO_2 increases the surface area of the PPy which increases its ability to interact well with the ions liberated during the corrosion process of steel in the presence of an electrolyte (Mahmoudian et al., 2011b).

2.9.2 Polyaniline nanocomposites for corrosion protection

Metals, metalloids, metal oxide particles or nanoparticles, as well as carbon nanomaterials such as carbon nanotubes and graphene, can be incorporated into the matrix of a PANI to produce PANI-based composite or nanocomposites materials (Ćirić-Marjanović, 2013a). To show the improved protection ability of PANI composite on a mild steel substrate, coatings based on a PANI matrix filled with zinc and zinc nanoparticles were obtained on iron by solution mixing method (Olad et al., 2011). The corrosion products of Zn can fill the pores in the PANI causing more barrier protection along with the added electrochemical activity of PANI. Open circuit potential

measurements exhibited a positive shift demonstrating enhanced anticorrosion performance for PANI-Zn nanocomposite coating as compared to the PANI coating (Deshpande et al., 2014; Rohwerder, 2009).

2.10 Corrosion protection mechanisms of conducting polymers

To date, there are four proposed possible corrosion prevention mechanisms of conducting polymers (DeBerry, 1985; Eftekhari, 2011; Rohwerder, 2009; Wessling, 1994):

I) Anodic protection: In this mechanism, conducting polymer coatings may result in the formation of passive layers of metal oxides on the surface of the metal thereby preventing it from corroding (Gašparac & Martin, 2001; Wessling, 1996).

II) Controlled inhibitor release: Based on this mechanism, the oxidized and henceforth doped conducting polymer coating on the surface of metal may lead to the liberation of an anion dopant upon reduction (Kinlen et al., 1999). On account of doped PANI, the anions are released through reduction process as well as the simple elimination of corrosive dopant if it is soluble in water as can be seen in Figure 2.15.

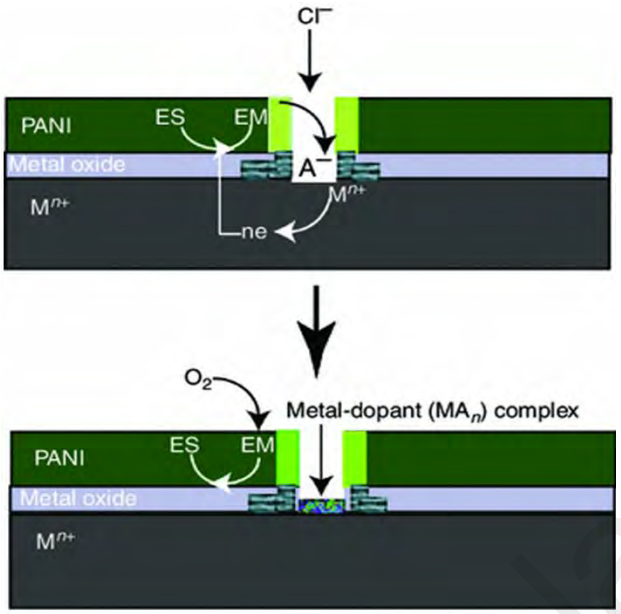

Figure 2.15: Controlled inhibitor release mechanism for a steel coating, M coated with a conducting polymer layer (PANI) doped with an anion, A^-, acting as corrosion protector (Reprinted with permission from Deshpande, P. P., Jadhav, N. G., Gelling, V. J., & Sazou, D. (2014). *Journal of Coatings Technology and Research, 11*(4), 473-494. Copy right 2014, American coatings Association)

III) It is assumed that when a metal comes into contact with a conducting polymer, an electric field is created that would restrict the movement of electrons from the metal surface to an oxidizing species, and consequently decreasing the corrosion rate (Chandrasekhar, 2013).

IV) Coatings of CP form a dense, adherent, low permeable film and sustain a basic environment on a metal surface thereby limiting access of oxidants and averting the oxidation of the metal surface (de Souza et al., 2001; Hasanov & Bilgiç, 2009). The less permeable conducting polymer layer, the better is the hindrance effect and the lower is the mobility level of the O_2 and water into the polymer matrix. By increasing the adherence to the surface of the steel, the site of the reaction of O_2 reduction changes from the steel|conducting polymer coating interface to the conducting polymer|electrolyte interface (Michalik & Rohwerder, 2005). The shift in the O_2-reduction on the CP

surface results in the decrease of the reduction products (OH) through the steel|conducting polymer coating interface, preventing "disbondment and delamination of the coating" (Kinlen et al., 1999; Paliwoda-Porebska et al., 2005). Conversely, the O_2 reduction is involved in the local re-oxidation of the conducting polymer and constant active of the conducting polymer coating in case that local pinholes or small size defects are formed. Hence, improving the barrier effect by processes that inactivate conducting polymers should be avoided. To the extent that the CP is in its conductive form, the OCP of the steel|CP-coating|electrolyte is in the passive form. The site and the kinetics of the O_2 reduction are vital for the long-term protective properties of the coating. It is commonly noticed that dehydration of CP electrodeposited film on metals from aqueous medium increases the barrier effect.

Among the four mechanisms mentioned above, the initial two are viewed as essential ones by which corrosion protection by conducting polymers can be rationalized regarding the active role of conducting polymer layer. The last two mechanisms contribute concurrently to a reasonable level in cases where the anodic protection or the inhibitor release controlled mechanism determined the corrosion protection for a particular steel|CP-coating|electrolyte system. The inhibitor release controlled mechanism has been proposed in places where CP-based coatings protect localized corrosion in chloride containing electrolytes.

2.11 Open circuit potential (OCP) and linear polarization techniques

The OCP measurement refers to the potential difference between the working and reference electrodes under the same experimental condition, obtained in the absence of external polarization. The system is frequently characterized electrochemically by the

OCP variation in a specified period. Therefore, compared to the bare metal, the coated steel can be seen to have higher potential. Higher protection is achieved at a higher potential as well as when the potential is sustained for an extended period. Therefore, coatings protect steel substrates from corrosion, by either providing a physical barrier against the corrosive environments (such as electrolytes, H_2O, chloride ions, O_2, and so forth.) or through reacting with the corrosive media thereby creating passive oxide layer (Sedriks, 1996). However, the protection mechanism of coatings depends on its properties such as coating thickness, the density of the coating and chemical composition of the coating. Hence, the OCP results serve as the initial potential in potentiodynamic polarization or electrochemical impedance studies.

The Tafel analysis could instantaneously measure the corrosion rates for both uncoated as well as coated steels that are exposed to corrosive environments. The Tafel measurements rely on the zero over-voltage (η) of a given system. The zero over-voltage of a system refers to the within ±10 mV, of that system (Despić & Parkhutik, 1989; Sedriks, 1996). Hence, the Ohm´s law is obeyed by the obtained over-voltage-current density (i), and as a result, a linear correlation is achieved. The corrosion current density is termed as the current that flows per unit area (*I/A*), and it is measured in Acm^{-2}. Figure 2.16 shows the values of the cathodic (-) and anodic (+) polarization segments around the open circuit potential.

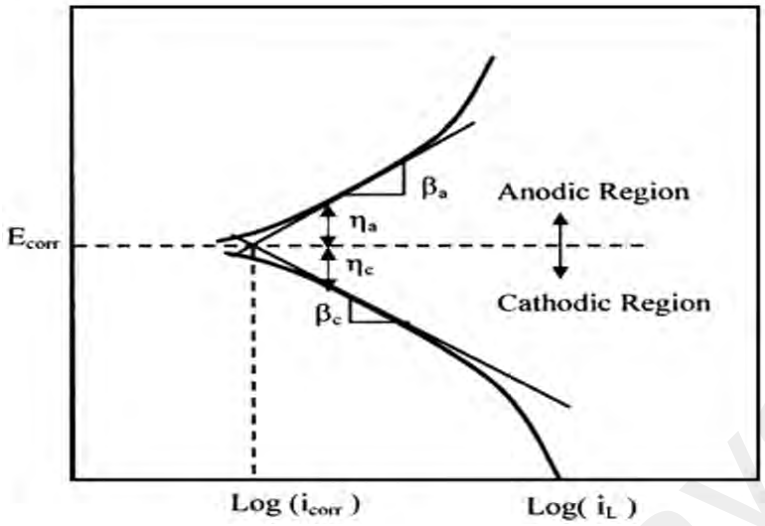

Figure 2.16: A schematic diagram of Tafel curve

The $\Delta E/\Delta i$ is the slope which has a unit of resistance (Ω) and is inversely proportional to the corrosion rate of the system also known as the corrosion current density given by i_{corr}, in Equation (2.6)

$$\frac{\Delta E}{\Delta i} = \frac{\beta_a \beta_c}{2.3(i_{corr})(\beta_a + \beta_c)} \tag{2.6}$$

The βc and βa in Equation 2.6 represent the Tafel slopes corresponding to the cathodic and anodic reactions respectively, whereas the value 2.3 is a constant. The plot of log *I* vs η was otherwise known as the Tafel plot can be used to calculate the Tafel slopes (Fontana, 1980). The corrosion resistance method, the linear polarization method, and polarization resistance method use direct current (DC) and voltage. Therefore, after every measurement cycle, a more profound perturbation is applied to the system under study. However, this is undesirable for continuous measurements taken on the same specimen with minimum external perturbation.

Furthermore, the corrosion current density, or the resistance obtained by the slope ($\Delta E/\Delta i$), can likewise be determined by EIS (Ezhilselvi et al., 2016; Sedriks, 1996). In this study, as in many related works, the open circuit potential and electrochemical impedance spectroscopy analysis are used to examine the anticorrosion properties and

degradation of coatings on steel (Amirudin & Thieny, 1995; Bonora et al., 1996; Canobre et al., 2009; DeBerry, 1985; Jorcin et al., 2006; Kraljić et al., 2003; Wessling, 1996; Yoon et al., 2011; Zarras & Stenger-Smith, 2014; Zhong et al., 2008).

2.12 Electrochemical Impedance spectroscopy (EIS)

EIS is a great tool with a wide scope of research applications. EIS utilizes little sinusoidal potential, which is more valuable for repetitive and steady measurement on the similar specimens. Commonly, under reasonable conditions for measuring EIS, the system can be viewed as remotely unperturbed by the measurement (Despić & Parkhutik, 1989; Sedriks, 1996). Likewise, EIS offers more understanding of the protection mechanism, the rate determining, and many useful parameters concerning the coating deterioration or properties, such as coating resistance (R_C) and capacitance of coating (C_C), the delamination area, electrolytes uptake by the coating, and the pore resistance (R). On the account of the preferences offered by EIS, this technique was supported over the linear-polarization for evaluating the inhibitory properties of the coatings and the electrochemical behavior of the steel substrate. In EIS the frequencies response are distinctive for various surfaces (Bard & Faulkner, 2001). In EIS measurements, Nyquist and Bode's plots are utilized to interpret the corrosion behavior of steel surfaces. The impedance (Z) is defined as the total resistance (Ω) of the electric circuits (Barsoukov & Macdonald, 2005; Sedriks, 1996). Impedance (Z) is the summation of resistance (R) and the reactance (X) acquired from an electric circuit system when a 5-10 mV perturbation of AC potential is applied to it. Also, the AC is recorded while the angular frequency (ω) is cleared over a range of several decades as shown in Equation 2.7.

$$Z[j\omega] = \frac{v[j\omega]}{I[j\omega]} = R + jX,\ j = \sqrt{-1} \equiv \exp^{j\pi/2} \tag{2.7}$$

Where Z[jω] represents the impedance, I and V are the current and potential at each value of ω and j stands for complex (Barsoukov & Macdonald, 2005; Despić & Parkhutik, 1989).

$$Z(\omega) = Z' + jZ'' \tag{2.8}$$

The real and imaginary impedances are represented in Equation 2.8, whereas the impedance components corresponding to the R and X are displayed in Equation 2.7. As can be seen in Equation 2.9 the reactance is openly linked with the capacitance of the electric circuit.

$$X = \frac{1}{2\pi fC} = \frac{1}{\omega C}, \omega = 2\pi f \tag{2.9}$$

The impedance magnitude, polar coordinates, and phase angle (θ) at each frequency revealed in Figure 2.17 can be defined as

$$|Z| = (R^2 + X^2)^{1/2} \tag{2.10}$$

$$\theta = \tan^{-1}(X/Y) \tag{2.11}$$

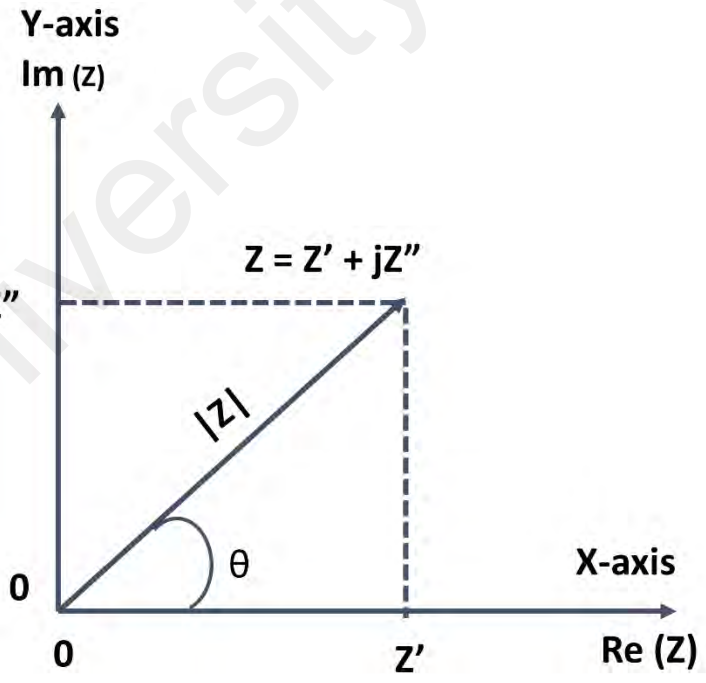

Figure 2.17: Impedance vector plotted in rectangular and polar coordinates

The observed phase angle was due to the shift noticed in the AC current compared to the perturbation AC potential used based on the properties of the system. The real and imaginary components of impedance is usually related to the corresponding polar components as in Equations 2.12 and 2.13.

$$R_e(Z) \equiv Z' = |Z| \cos(\theta) \tag{2.12}$$

$$I_m(Z) \equiv Z'' = |Z| \sin(\theta) \tag{2.13}$$

There are two types of Bode diagrams namely "total impedance modulus" and "phase angle (Macdonald, 2006). Figure 2.18 demonstrates the two types of impedance plots for the electrical equivalent circuit, which is used to explain the behavior of electrodes under corrosion investigation (Barsoukov & Macdonald, 2005; Despić & Parkhutik, 1989; Sedriks, 1996).

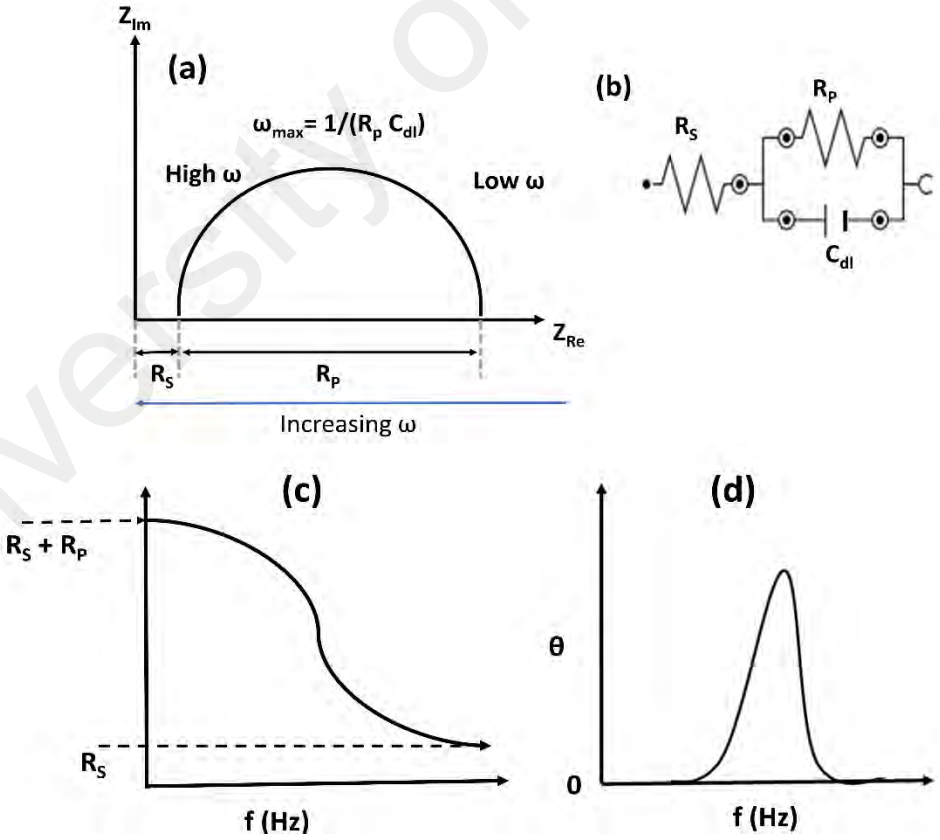

Figure 2.18: (a) Nyquist, (b) Randles electric circuit, (c) Bode – total impedance magnitude, and (d) Bode – phase angle plots

The equivalent electrical circuit is known as randles circuit (Figure 2.18b) comprises of a resistance R_s, representing the dual effect from the electrolyte and any film on the substrate surface, in series with a parallel combination of a capacitance C_{dl}, which is assigned to the double-layer capacitance at the substrate (steel) interface, and a resistance R_p, arising from the charge transfer process. For the circuit in Figure 2.18b, for example at high frequencies (10 kHz), *X* becomes slight. Meanwhile, the capacitor conducts very easily. For an RC parallel combination at 10 kHz, irrespective of the R_{corr} value, the total impedance is nearly the same as the minor contribution.

Therefore, the impedance of the complete circuit approaches R_s, the first point to the left side in the Nyquist diagram (Figure 2.18a), and the first point to the right side in both Bode plots (Figures 2.18c and d). At the point when frequency decreases, the conduction of the capacitor drops, and the impedance response shows a semicircle in the Nyquist plot. At very low frequencies, e.g. 10 mHz, *X* becomes huge, so, the RC approaches R_{corr}. Thus, the overall impedance of the circuit is $R_s + R_{corr}$, matching the last point on the Nyquist plot (right side), and the last comment to the left in the Bode diagrams. The earlier depiction demonstrates the use of equivalent electric circuits in EIS data analysis. Once the impedance experimental data has been acquired, a proposed electrical equivalent circuit is used to fit the experimental data. The simplest electrical circuit will be chosen as long as it provides the lowest value of goodness of fit (χ^2), with all its electric elements having a physical meaning to represent the system appropriately under study and explain its EIS electrochemical behavior.

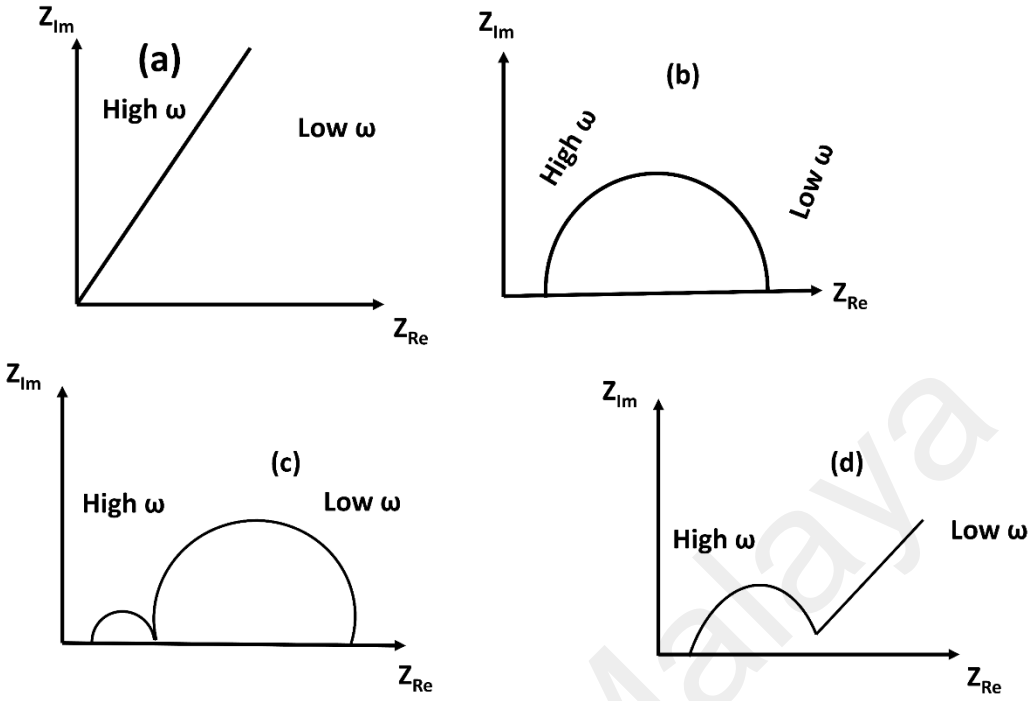

Figure 2.19: Schematic Nyquist plots of a paint-coated steel at a different level of degradation from (a) intact coating to (d) damaged coating with a diffusion controlled degradation process (Cebada-Ricalde, 2014)

When the system under investigation is a organic coated, corrosion occurs in stages (Atwa, 2010; Cebada-Ricalde, 2014; Loveday et al., 2004; Macedo et al., 2009). The coating degradation steps depend on the organic coating, and each of these steps displays a particular nature in the Nyquist plots (Figure 2.19) and Bode plots (Figure 2.20). In general, at the beginning of the exposure, the organic coating is intact and provides full protection to the metal from the corrodents in the medium. Therefore, the Nyquist diagram (Figure 2.19a), and the Bode impedance magnitude plot (Figure 2.20a) indicate a straight line, indicating a capacitor. Then, a huge resistance of coating and a very low capacitance of coating are projected. The EIS plots at this level, describe only the protecting properties of the organic coating. The barrier properties of the coating are inferred from the Bode phase plot (Figure 2.20a).

As the time of exposure increases, the ions in the corrosive environments and water diffuse through the organic coating, which makes the Bode impedance magnitude to decrease (Figure 2.20b). In the Nyquist plot (Figure 2.19b) coating resistance becomes

smaller as compared to its initial value, while the impedance exhibits a semicircle behavior. Therefore, no substantial metal corrosion process is going on, since the corrodents are still not in direct contact with the metal/coating interface. When the time of exposure increases, the solution extends to the interface of metal/coating, so a bigger area of the metal is in direct contact with the corrodents. Thus, the corrosion begins. The bigger the metal area exposed to the solution, the smaller the corrosion resistance and the larger is the double-layer capacitance. Two corrosion reactions occur at this stage, similar to two-time constants. These appear two semicircles in the Nyquist diagrams (Figure 2.19c), two bands in the Bode phase diagram (Figure 2.20c), and two breaks in the Bode impedance magnitude diagram (left in Figure 2.20c). The behavior of the double layer capacitance is seen at low frequencies at the interface of metal/solution, while at high frequencies, the response of the organic coating capacitance is noticed. In some cases at larger exposure times, depending on the coating, the corrosion is controlled by diffusion. In this situation, a characteristic Nyquist diagram (Figure 2.19d) looks like a semicircle with a straight line at higher frequencies, forming a 45° angle with the Re(Z) axis, at lower frequencies. This type of semicircle in Nyquist diagram is showing an element of a diffusion-controlled corrosion process. The similar Bode plots are displayed in Figure 2.20d.

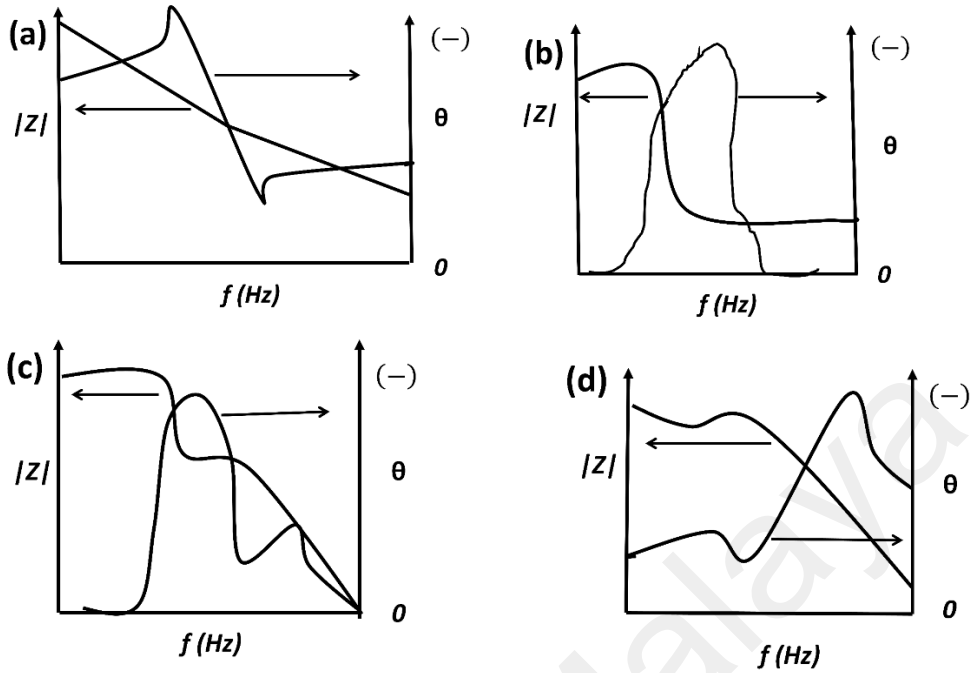

Figure 2.20: Bode plots of a paint-coated steel at various levels of damage. From (a) intact coating to (d) damaged coating with a diffusion controlled damage process

CHAPTER 3: METHODOLOGY

In this chapter, the experimental procedures for the: i) preparation and characterization of conducting polymer nanocomposites and ii) corrosion study is being described. Also, the fundamental principles of the analytical techniques used in the characterization of the prepared nanocomposites are explained.

The steel elemental composition used in this research (wt %, determined by quantiometric method) was as follows: Mn (1.03), P (0.04), C (0.26) Si (0.28), Cu (0.20), S (0.05), and Fe (98.14). The thickness of the coatings was measured using Eco test-Sheen coating thickness

3.1 Preparation and characterization of Co-doped TiO_2/PPy nanocomposites (NTCs) for corrosion protection.

3.1.1 Synthesis of Co-doped TiO_2 and TiO_2 nanoparticles (NPs)

All chemicals were procured from Sigma-Aldrich. The Co-doped TiO_2 NPs were prepared by sol-gel technique (Jeon & Baek, 2010) using titanium tetra-isopropoxide ($Ti[OCH(CH_3)_2]_4$, and cobalt acetate tetrahydrate as the precursors. In the beginning, the titanium precursor and cobalt acetate were mixed with glacial acetic acid, with double distilled water added to the mixture. The molar ratio of the Co-doped (3.0 mol %) nanocomposite was 1:10:200 for $[Ti(OCH(CH_3)_2)]_4$: glacial acetic acid: H_2O, respectively. The solution was constantly stirred for 6 h and then kept for 24 h at an ambient temperature to form a gel. The as-synthesized gel was placed at 75 °C in an oven, after which was ground to fine powders and finally calcined at 500 °C for 5 h. The TiO_2 NPs were also prepared using the same procedures for comparison with the Co-doped TiO_2 NPs (Karthik et al., 2010; Mugundan et al., 2015).

3.1.2 Synthesis of Co-doped TiO_2/PPy NTCs

Co-doped TiO_2/PPy NTCs were synthesized through a chemical oxidative polymerization reaction by using methyl orange (MO) as a soft template. In the beginning, the polymerization was performed by dissolving 0.58 g $FeCl_3$ in 5 mM MO (Mahmoudian et al., 2013), followed by the addition of 0.19 g Co-doped TiO_2 NPs in the mixture. This was followed by stirring for 30 min, after which pyrrole monomer of 0.2 mL was added dropwise into the solution. The polymerization was achieved without stirring for 24 h at 0–4 °C. The resulting product was collected and washed several times using double distilled water and kept at 40 °C in an oven for 24 h. The same procedures were used in the synthesis of PPy/TiO_2 NTCs and PPy NT, with the presence and absence of TiO_2 NPs.

3.1.3 Characterizations of Co-doped TiO_2/PPy NTCs

X-ray diffraction (XRD) was performed to confirm the presence of TiO_2 and Co-doped TiO_2NPs in the PPy NTs matrix, while, TEM was used to determine the size of the nanoparticles. The morphology of the Co-doped TiO_2/PPy, TiO_2/PPy and PPy NT was characterized by FESEM (Hitachi, model: SU8220). The chemical bonding of the nanocomposites was analyzed with FT-IR spectrophotometer (spectrum 400). The thermogravimetric analysis (TGA) was performed on Perkin-Elmer 4000 TG analyser, to measure the thermal stabilities of the PPy NT, TiO_2/PPy NTCs, and Co-doped TiO_2/PPy NTCs respectively, at a heating rate of 10°C /min under nitrogen atmosphere.

3.1.4 Coating formulations of Co-doped TiO_2 /PPy NTCs for corrosion tests

2 g of 60,000 MW butvar (Sigma–Aldrich) was transferred into a vessel containing 20 mL methanol and constantly stirred for 24 h. This was followed by the addition of 1 wt% of the Co-doped TiO_2/PPy NTCs powder into the butvar coating solution and constantly stirred for another 24 h. The steel elemental composition (wt %, determined by quantiometric method) was as follows: Mn (1.03), P (0.04), C (0.26) Si (0.28), Cu

(0.20), S (0.05), and Fe (98.14). Steel sheets of 6 cm × 4 cm × 0.2 cm were subjected to the sandblasting process to acquire a nearly white surface finish before the coating procedures (Venison, 1973; Yin & Lu, 2003). The steel samples were dip-coated for the 30s in a Co-doped TiO_2/PPy NTCs –butvar coating solution and dried at ambient temperature for 20 min. The coated steel samples were then air dried at 50 °C in an oven for 24 h. Steel panels coated with butvar incorporated with TiO_2/PPy NTCs and PPy NT were also prepared, and a steel panel coated with butvar alone was used as the control. The steel samples with a coating thickness of 16 ± 1 µm (measured using Eco test-Sheen coating thickness) were used for the corrosion tests. Glass cylinders having a diameter of 2 cm with a length measuring 4 cm were glued on the coated sample. The coated steel samples were the working electrode (WE), while a graphite rod and saturated calomel electrode-Ag/AgCl (SCE) were the counter and reference electrodes, respectively.

3.1.5 Corrosion measurements of Co-doped TiO_2 /PPy NTCs

The anticorrosive properties of the coated mild steel were evaluated using EIS measurements. The electrochemical impedance spectra were analyzed between 100 kHz to 0.01 Hz with an acquisition of 10 points per decade, at 5mV signal amplitude around the open circuit potential (OCP) (Liu et al., 2015). In the EIS experiments, a FRA.EXE software was installed in a computer connected to a USB_IF030 interface-controlled Autolab PGSTAT302N. The electrochemical cell was placed in a Faraday cage to protect against electromagnetic interference. All the tests were performed at ambient temperature. An area of 3.14 cm^2 of the coated steel was immersed in a solution of 3.5% NaCl. The impedance spectra analysis was achieved by fitting the experimental data to equivalent circuits, through the non-linear least-square fitting technique. The fitting was assessed by controlling the relative error value of each element in the equivalent circuit

to 5% and by limiting the χ^2 value. The Tafel curves were obtained between +0.50 V and −1.50 V at 5 mV s^{-1} in 3.5% NaCl solution.

3.2 Nanocomposites of Co-doped TiO_2/graphene oxide/polyaniline (Co-doped TiO_2/GO/PANI) as an efficient agent for the protection of carbon steel.

3.2.1 Synthesis of Co-doped TiO_2 NPs

The same procedure as in section 3.2.1 was employed. Briefly, The Co-doped TiO_2 NPs were prepared by sol-gel technique (Jeon & Baek, 2010) using titanium tetra-isopropoxide ($Ti[OCH(CH_3)_2]_4$, and cobalt acetate tetrahydrate as the precursors. The solution was constantly stirred for 6 h and then kept for 24 h at an ambient temperature to form a gel. The as-synthesized gel was maintained at 75 °C in an oven, after which was ground to fine powders and finally calcined at 500 °C for 5 h. The TiO_2 NPs were also prepared using the same procedures for comparison with the Co-doped TiO_2 NPs (Karthik et al., 2010; Mugundan et al., 2015).

3.2.2 Synthesis of graphene oxide (GO)

The GO was prepared from the graphite flakes using the Hummers' method (Ming, 2011). Firstly, 360 mL of concentrated H_2SO_4 and 40 mL H_3PO_4 were added into a beaker containing 3 g of graphite at room temperature. This was followed by the gradual addition of 18 g of $KMnO_4$ into the mixture and constantly stirred for three days to ensure the complete oxidation of the graphite. The suspension was cooled and diluted with 400 mL of ice water, followed by the addition of H_2O_2 (30%) until the gas evolution stopped. This was done to ensure that the residual permanganate was reduced to manganese ions. The obtained GO suspension was washed with dilute 1 M HCl and double distilled H_2O several times until pH 5. The final product was separated from the solution mixture by ultra-centrifugation at 11000 rpm.

3.2.3 Preparation of Co-doped TiO_2/GO/PANI NCs

The Co-doped TiO_2/GO/PANI NCs were synthesized by an *in situ* chemical oxidative polymerization process. The polymerization process was performed with the addition of 0.24 g Co-doped TiO_2 NPs into 35 mL 0.1 M HCl solution containing GO (0.063 g) dispersion and stirred for 30 min in the presence of 1 mL aniline. This was followed by the dropwise addition of 3.51 g ammonium persulfate $(NH_4)_2S_2O_8$ in 20 mL 0.1 M HCl solution to the suspension mixture with constant stirring. The stirring was continued for 12 hrs at room temperature for the complete polymerization of the aniline. The Co-doped TiO_2/GO/PANI NCs was washed with double distilled water several times and dried for 1 day at 45 °C in the oven. The same procedures were followed for the synthesis of Co-doped TiO_2/PANI NCs in the absence of GO. Also, PANI was synthesized using the same conditions in the absence of both GO and Co-doped TiO_2 NPs.

3.2.4 Characterizations of Co-doped TiO_2/GO/PANI NCs

The chemical structure of the synthesized Co-doped TiO_2/GO/PANI nanocomposites was characterized by Fourier transformed infrared (FT-IR) spectrophotometer (spectrum 400) over a wavelength range of 400−4000 cm^{-1}. The morphology of the synthesized Co-doped TiO_2/GO/PANI nanocomposites were examined by field-emission scanning electron microscopy (FESEM) (Hitachi, model: SU8220). The X-Ray diffraction (XRD) was carried out using Siemens D5000, with a Cu-Kα radiation source mounted on a horizontal θ-2θ goniometer. Transmission electron microscopy (TEM) analyses were performed on JEM 2100-F at an accelerating voltage of 200 kV.

3.2.5 Preparation of coating formulations

Before coating, carbon steel substrates (3 x 4 cm^2) were polished with emery paper grades of 800, 1000, 1200 and 1500 respectively, then cleaned with ethanol, rinsed with

distilled water and finally air-dried. Meanwhile, 2 g of 60,000 MW polyvinyl butyral (butvar) (Sigma–Aldrich) was transferred into a vessel containing 20 mL methanol and constantly stirred for 24 h. Subsequently, 1 wt% of Co-doped TiO_2/GO/PANI NCs was added into the butvar coating solution and constantly stirred for another 24 h. The steel elemental composition (wt %, determined by quantiometric method) was as follows: Mn (1.03), P (0.04), C (0.26) Si (0.28), Cu (0.20), S (0.05), and Fe (98.14). The steel samples were dip-coated into the Co-doped TiO_2/GO/PANI NCs–butvar coating solution for 30 seconds and dried at ambient temperature for 20 min. The coated steel samples were then air dried at 50 °C in an oven for 24 h. Steel panels coated with butvar incorporated with Co-doped TiO_2/PANI NCs and PANI NTs were also prepared, and a steel panel coated with pure butvar was used as the control. For the prepared specimens, the coating thickness was set at 18 ±2 µm. Glass cylinders with a diameter of 2 cm and 4 cm length were glued on the coated steel samples (Mahmoudian et al., 2011). The coated steel samples were used as the working electrodes (WE), while a graphite rod and saturated calomel electrode Ag/AgCl (SCE) were the counter and reference electrodes, respectively.

3.2.6 Corrosion measurements of Co-doped TiO_2/GO/PANI NCs

The anticorrosive properties of the coated carbon steel were evaluated using electrochemical impedance spectra (EIS) and potentiodynamic polarization measurements. The electrochemical impedance spectra were analyzed between 100 kHz to 10 mHz with an acquisition of 10 points per decade, at 5mV signal amplitude around the open circuit potential (OCP) (Liu et al., 2015). A FRA.EXE software installed in a computer and connected to USB_IF030 interface-controlled Autolab PGSTAT302N instrument was used to run the EIS experiments. The electrochemical cell was positioned in a Faraday cage to protect against electromagnetic interference. All the electrochemical measurements were performed at ambient temperature. An area of

3.14 cm^2 of the coated steel was immersed into a solution of 3.5% NaCl. The impedance spectra analysis was achieved by fitting the experimental data to equivalent circuits, through the non-linear least-square fitting technique. The fitting was assessed by controlling the relative error of each element in the equivalent circuit to 5% and by limiting the χ^2 value. The Tafel curves were obtained between +0.50 V and −1.50 V at 5 mV s^{-1} in 3.5% NaCl solution. The corrosion current density was evaluated using the general purpose electrochemical software (GPES) installed in the computer and interfaced with the Autolab PGSTAT 302N (Metrohm). The corrosion current was obtained from the point of intersection of the extrapolated straight lines along the linear portion of the anodic and cathodic Tafel curves.

3.3 Synthesis and characterization of PANI/GO/Zn-doped TiO_2 NCs for corrosion control

3.3.1 GO synthesis

The same method as in section 3.3.1 above was used to synthesize the GO utilized for this project.

3.3.2 Preparation of Zn-doped TiO_2 NPs

Zn-doped TiO_2 NPs were synthesized using titanium tetra-isopropoxide (TTIP; Aldrich) and zinc acetate (Merck) as precursors of both titanium and zinc, respectively via the sol-gel technique. At first, TTIP and zinc acetate were dissolved in 100% glacial acetic acid. Then, DI H_2O was added to the above solution to achieve complete hydrolysis and polycondensation reaction. The molar ratio of the synthesized Zn-doped TiO_2 (3 mol %) was 1:10:200 of (TTIP: acetic acid: DI H_2O). The whole mixture was constantly stirred for 6 h at room temperature. The obtained homogeneous solution was kept at 75 °C for gel formation. The resultant gel was calcined in a furnace at 500 °C for

the period of 5 h. On the other hand, TiO_2 NPs was prepared using the same process for comparison.

3.3.3 Preparation of PANI/GO/Zn-doped TiO_2 NCs

PANI/GO/Zn-doped TiO_2 was synthesized via chemical oxidative polymerization. As reported elsewhere (Mahmoudian et al., 2012), the chemical polymerization was achieved by dispersing (3 g, 9 x 10^{-2} mol) of sodium dodecylbenzene sulfonate (SDBS) in 50 mL of DI H_2O, the mixture was sonicated until an entirely homogeneous solution is obtained. After that, 0.09 mol of aniline monomer was added to the SDBS solution and stirred until emulsified. Then, 9 mL of 1 M HCl acid was added to the emulsified mixture. It is clear that the molar proportion of the monomer to SDBS for this research was 1:1. The whole mixture was stirred for 15 min at ambient temperature, and 30 mL of 0.03 M ammonium persulfate, APS (kept at low temperature for 5 h) was added dropwise to the mixture with constant and vigorous stirring. The polymerization was carried out under static conditions for 3 h at ambient temperature. The obtained product was repeatedly washed with DI H_2O and dried at 45 °C for 36 h in an oven.

3.3.4 Characterizations of PANI/GO/Zn-doped TiO_2 NCs

The morphology of the prepared PANI/GO/Zn-doped TiO_2 NCs were studied by field-emission scanning electron microscopy (FESEM) (Hitachi, model: SU8220). Fourier transformed infrared (FT-IR) spectrophotometer (spectrum 400) over a wavelength range of 400−4000 cm^{-1} was used for the chemical structure characterization of the prepared PANI/GO/Zn-doped TiO_2 NCs. The X-Ray diffraction (XRD) was performed using Siemens D5000, with a Cu-Kα radiation source mounted on a horizontal θ-2θ goniometer. Transmission electron microscopy (TEM) analyses were carried out on JEM 2100-F at an accelerating voltage of 200 kV.

3.3.5 Preparation of PANI/GO/Zn-doped TiO_2 NCs-butvar coating

At first, steel panels (4 x 4 cm^2) were polished with emery paper grades of 600, 800, 1000, 1200, 1500 and 2000 respectively, then washed with ethanol, rinsed with DI H_2O and then air-dried. A 2 g of polyvinyl butyral (butvar) (Sigma–Aldrich) was transferred into a container of 20 mL methanol and stirred for 24 h. Next, 1 wt% of PANI/GO/Zn-doped TiO_2 NCs was added into the solution of butvar and constantly stirred for another 24 h. The steel elemental compositions were the same as reported in section 3.3.5. The steel panels were dip-coated into the PANI/GO/Zn-doped TiO_2 NCs–butvar coating formulation for 30 seconds and dried at room temperature for 15 min. The coated panels were then air dried at 45 °C in an oven for 24 h. Steel panels coated with butvar incorporated with PANI/Zn-doped TiO_2 NCs and PANI NTs were also prepared, and the pure butvar coated steel panel was used as a control. For the prepared specimens, the coating thickness was set at 15 ±2 μm. Glass cylinders with a diameter of 2 cm and 4 cm length were glued on the coated steel samples. The coated steel samples were used as the working electrodes (WE), while a platinum wire and Ag/AgCl (SCE) were the counter and reference electrodes, respectively.

3.3.6 Corrosion measurements of PANI/GO/Zn-doped TiO_2 NCs

The corrosion resistant properties of the carbon steel were evaluated using EIS and potentiodynamic polarization measurements. The electrochemical impedance spectra were analyzed between 100 kHz to 10 mHz with an acquisition of 10 points per decade, at 5mV signal amplitude around the open circuit potential (OCP) (Liu et al., 2015). A FRA.EXE software installed in a computer and connected to USB_IF030 interface-controlled Autolab PGSTAT302N instrument was used to run the EIS experiments. The electrochemical cell was positioned in a Faraday cage to protect against electromagnetic interference. All the electrochemical measurements were performed at room temperature. The exposed area of the coated steel in a solution of 3.5% NaCl was

3.14 cm^2. The impedance spectra analysis was carried out by fitting the experimental data to equivalent circuits, through the non-linear least-square fitting technique. The fitting was assessed by controlling the relative error of each element in the equivalent circuit to 5% and by limiting the χ^2 value. The Tafel curves were obtained between +0.50 V and −1.50 V at 5 mV s^{-1} in 3.5% NaCl solution. The corrosion current density was evaluated using the general purpose electrochemical software (GPES) installed in the computer and interfaced with the Autolab PGSTAT 302N (Metrohm). The corrosion current was obtained from the point of intersection of the extrapolated straight lines along the linear portion of the anodic and cathodic Tafel curves.

3.4 Instrumentations

3.4.1 X-ray diffraction (XRD)

XRD is among the most important non-destructive techniques for the analysis of all kinds of crystalline materials. The two essential characteristics that can be obtained using X-ray diffraction (XRD) are fingerprint characterization of the crystalline materials and determination of their structure. The basics of XRD analysis are based on Bragg's law. When X-rays of wavelength λ are incident at an angle θ on a crystal lattice, a portion of these beams will be scattered in all directions. The necessary and sufficient condition for constructive interference is known as Bragg's law.

$$n\lambda = 2d_{hkl}\sin\theta \tag{3.1}$$

According to this law, scattered waves originating from each atom will be in phase with one another. Figure 3.1 indicates the geometric requirements for this condition. Parameters of Equation 3.1 are explained in Figure. 3.1.

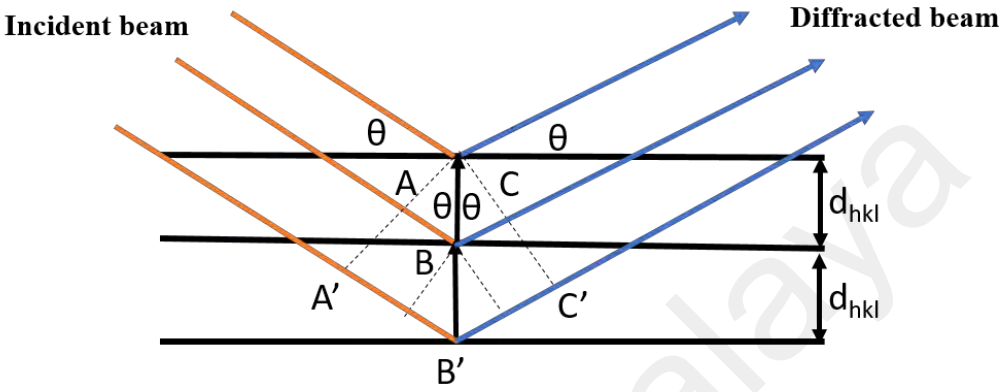

Figure 3.1: Diffraction of an X-rays beam diagram by the parallel atomic crystalline material

A Siemens D5000 XRD unit, with an X-ray source of wavelengths, K_α = 1.54 Å was used. Usually, diffraction experiments are applied at a fixed wavelength; therefore, measurement of the diffraction angles allows calculation of the associated d_{hkl} and the lattice constants.

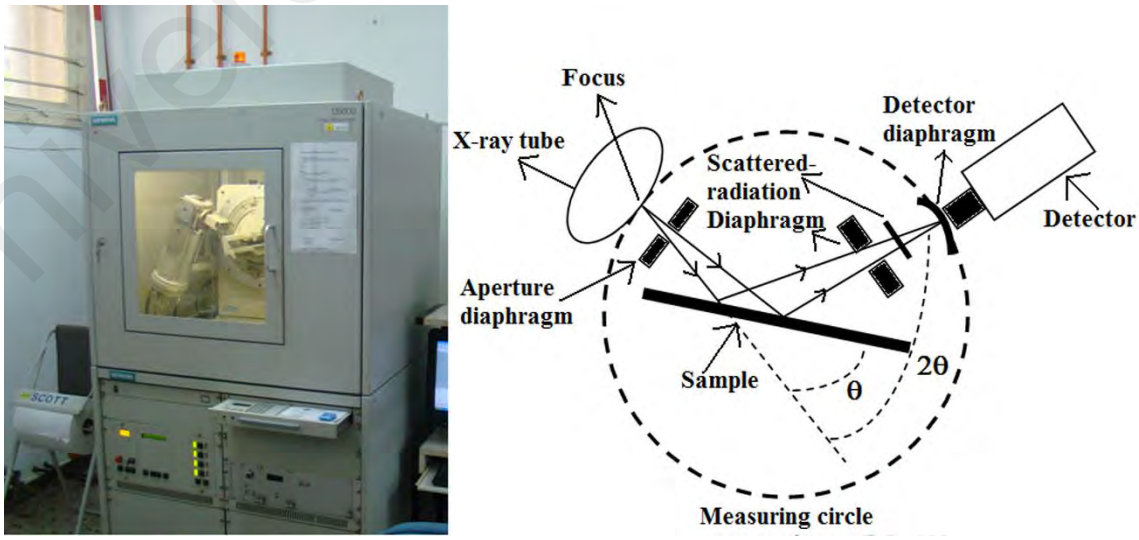

Figure 3.2: A photograph of the simple features of XRD experiment with Siemens D5000 set-up

3.4.2 Fourier transform infrared spectroscopy (FTIR)

FTIR spectroscopy is a tool used to obtain an infrared spectrum of absorption or emission of gas, liquid or solid. It is used to determine the interaction of a single beam of un-dispersed IR radiation with a sample, determining the frequencies at which the sample absorbs the radiation and the intensities of the absorptions are measured. It is known that chemical functional groups absorb light at specified frequencies. Therefore, the chemical structure could be predicted from the recorded spectrum. The chemical bonding of the synthesized materials was analyzed with FT-IR spectrophotometer (spectrum 400). The spectral range of 400 – 4000 cm^{-1} was used throughout.

3.4.3 Field emission scanning electron microscopy and energy dispersive X-ray analysis.

Field emission scanning electron microscopy (FESEM) is among the most used and recognized analytical tools. FESEM has more benefits as compared to the conventional tabletop or optical microscopes. The benefits are high resolution, large depth of focus, and high magnification as well as ease of sample preparation. Here, the electrons emitted from an electron gun enter the surface of a sample and generate many low energy secondary electrons. The intensity of these secondary electrons is directed by the surface topography of the sample. Therefore an image of the sample surface is raised by measuring the electron intensity (secondary) as a function of the location of the scanning electron beam (primary). Energy Dispersive X-Ray (EDX) and backscattered electron imaging are also considered useful techniques for chemical analysis. The intensity of backscattered electrons produced by electron bombardment can be correlated to the atomic number of the element within the sampling volume. Therefore, qualitative elemental information can be realized. The characteristic X-rays emitted from the sample serve as fingerprints and provide elemental information for the

samples, including semi-quantitative and quantitative data, as well as the line profiling and elemental/chemical mapping. FESEM with X-ray analysis is an efficient, inexpensive, and non-destructive method for carrying out surface analysis. A state-of-the-art state, high resolution FEI Quanta 200F FESEM with an EDX system (INCA Energy 400) from OXFORD was used in this research.

Figure 3.3: A set up of the FEI Quanta 200F FESEM equipped with EDX

Figure 3.3 displays the photograph of the FEI Quanta 200F FESEM equipped with EDX attached with a 32-bit computer system using Microsoft Windows 2000 as the operating system.

3.4.4 Transmission electron microscopy (TEM)

TEM is an imaging tool in which electron beam is transmitted onto an ultra-thin specimen and passed through it, interacting with the specimen as it passes through it. The interaction of the electrons transmitted through the specimen results in the formation of an image; the image is focused and magnified on an imaging machine like a photographic film layer or a screen of fluorescent, or to be detected by a charge coupled device (CCD). The magnified transmitted signal can be observed through direct

electron imaging or electron diffraction. Electron diffraction patterns are applied to determine the crystallographic structure of the materials. The picture of the TEM used in this research is shown in Figure 3.4.

Figure 3.4: TEM microscope unit (Philips CM200) photograph

3.4.5 Electrochemical analysis

Autolab PGSTAT-302N Potentiostat / Galvanostat have been used for investigation of the coatings and determination of the polarization and passivation of the electrodeposited layers. The GPES software is included in Autolab PGSTAT-302N. This software can run some useful DC techniques such as cyclic voltammetry, chronoamperometry, chronopotentiometry and so on. The polarization resistance of steel coated with a different type of coatings was examined by linear sweep voltammetry (LSV) through the Tafel curves. Tafel slope lines were extrapolated to identify the corrosion properties, as will be highlighted in the next chapter. Furthermore, passivation of the surfaces was studied by electrochemical impedance spectroscopy (EIS) through the FRA software. Figure 3.5 displays a schematic diagram of Autolab

PGSTAT-302N connected to the working electrode, reference electrode, counter electrode in the electrochemical cell.

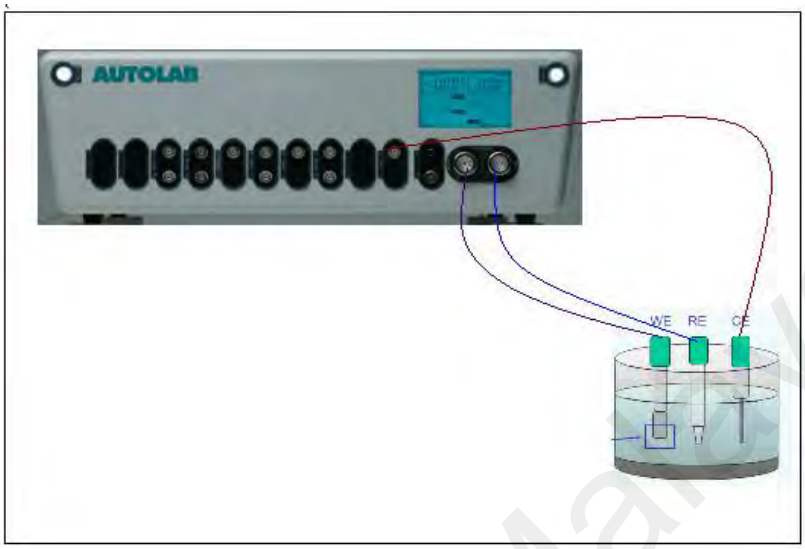

Figure 3.5: Schematic of Autolab PGSTAT-302N

CHAPTER 4: RESULTS AND DISCUSSION

4.1 Preparation and characterization of Co-doped TiO_2/PPy nanocomposites (NTCs) for corrosion protection.

4.1.1 Characterization

4.1.1.1 XRD of TiO_2 NPs, Co-doped TiO_2 NPs, TiO_2/PPy NTCs and Co-doped TiO_2/PPy NTCs.

The phase structure of the pure TiO_2 NPs, Co-doped TiO_2 NPs, TiO_2/PPy and Co-doped TiO_2/PPy nanocomposites are shown in Figure 4.1. From the XRD diffraction patterns, it is observed that both the TiO_2 NPs and the Co-doped TiO_2 NPs are in the anatase phase. The TiO_2 NPs spectrum reveals different diffraction peaks at 2θ values of 25.281°, 37.934°, 48.376°, 53.888°, 55.296°, 62.728°, 68.999°, 70.178°, 75.374° and 83.219°, which can be indexed to the (101), (103), (200), (105), (213), (116), (107) and (303) lattice planes of the tetragonal anatase TiO_2 (JCPDS entry 00-001-0562) with the lattice constant of a = b = 3.73 Å and c = 9.37 Å.

Also, it is evident that the XRD pattern of Co-doped TiO_2 NPs displays a similar XRD pattern with the TiO_2 NPs, i.e., at 3 wt % of cobalt doping, the XRD diffraction peaks do not show any cobalt phase (Karthik et al., 2010; Mugundan et al., 2015). This suggests that the cobalt ions are dispersed uniformly on the TiO_2, where the presence of cobalt does not influence the growth of new crystal arrangements of TiO_2. However, the high-intensity diffraction peak of Co-doped TiO_2 NPs at 25.281° is slightly broadened compared to the bare TiO_2 NPs. This is as a result of a decrease in the crystallite size of TiO_2 NPs in the presence of cobalt doping (Mugundan et al., 2015). The crystallite sizes were calculated from the full width at half-maximum (FWHM) of the (101) XRD diffraction peak using the Scherrer formula presented in Equation 4.1 (Sookhakian et al., 2014).

$$D = \frac{K\lambda}{\beta \cos\theta} \tag{4.1}$$

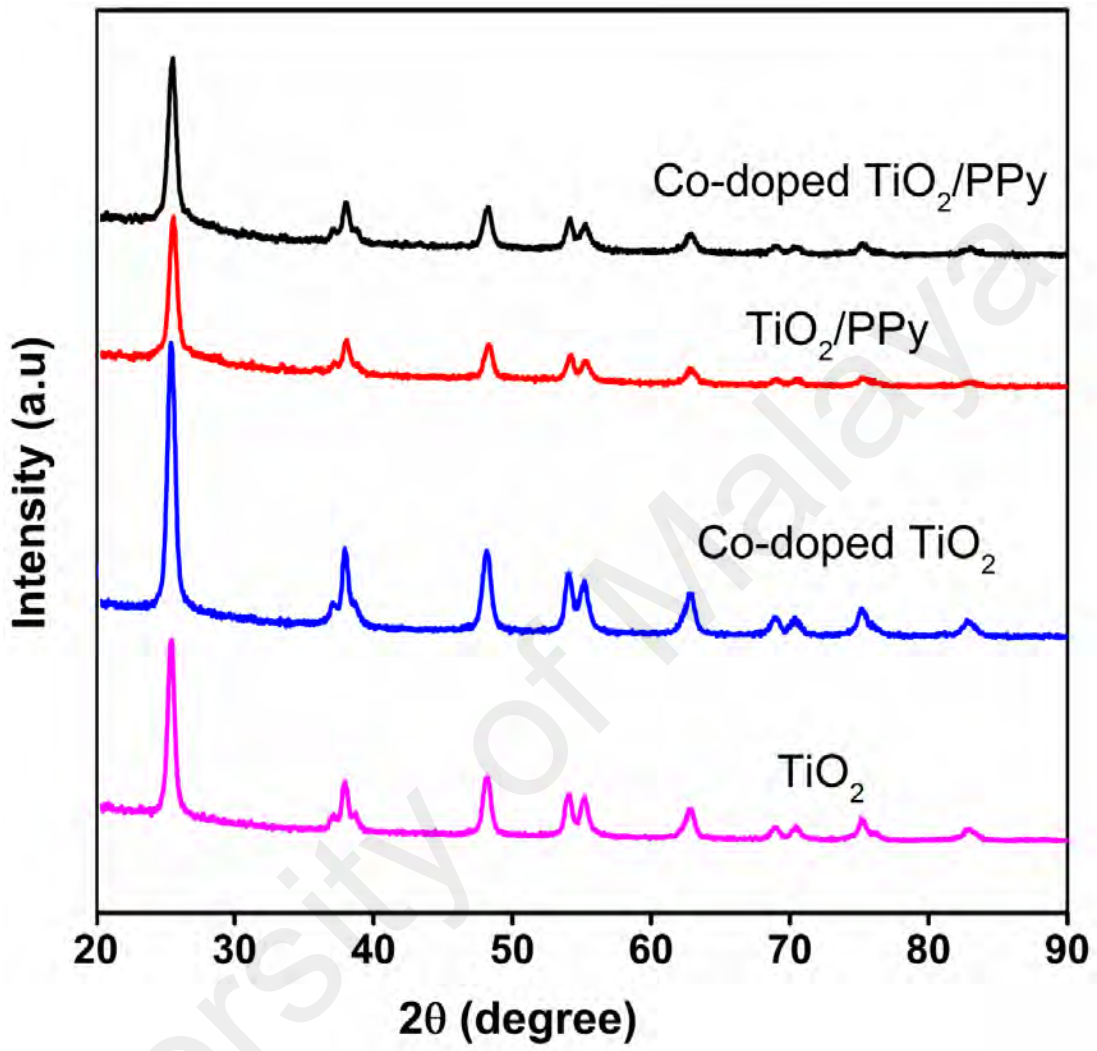

Figure 4.1: XRD diffractograms of TiO_2 NPs, Co-doped TiO_2 NPs, calcined at 500 °C for 6 hrs, TiO_2/PPy NTCs and Co-doped TiO_2/PPy NTCs

The parameter D is the crystallite size of the nanoparticle, K is the shape factor, which is 0.9; λ is the X-ray wavelength, β is the FWHM of the XRD diffraction pattern expressed in radian and θ is the angle of diffraction corresponding to the (101) plane. The crystallite sizes of the nanoparticles calculated from the Scherrer equation are 14.5 nm and 12.8 nm for TiO_2 and Co-doped TiO_2, respectively. It is observed that there are slight changes in the XRD patterns of TiO_2 and Co-doped TiO_2. These changes are due to the decrease in the crystal size of the TiO_2 NPs which could be attributed to the

difference in ionic radii between Co^{2+} and Ti^{4+}. Therefore, cobalt as a dopant impacts on the crystallite size during its growth, contrarily, it does not influence the crystal structure (Narayana et al., 2011). In our case, cobalt doping is further evidenced by the data obtained from EDX in Table 1.

4.1.1.2 The energy dispersive X-ray spectroscopy (EDX) of TiO_2 NPs and Co-doped TiO_2 NPs

Figure 4.2 (a and b) shows the EDX of TiO_2 NPs and Co-doped TiO_2 NPs respectively. The results indicate the presence of Ti, O and Co elements in the prepared TiO_2 NPs and Co-doped TiO_2 NPs respectively. The percentage by weight (wt%) of each of the elements is depicted in Table 4.1. These results confirmed the presence of Co in the TiO_2 NPs. Also, the 3 wt% of doped Co reveals that Co substituted Ti. Therefore, the Ti wt% decreased in the Co-doped TiO_2 NPs. The XRD result of Co-doped TiO_2 did not disclose any additional peaks of Co. Therefore the doping of Co into the TiO_2 lattice was successful.

Table 4.1: EDX data of the TiO_2 NPs and Co-doped TiO_2 NPs calcined at 500 ºC for 5h

Sample	Wt %	Atomic %
TiO_2 NPs		
Ti	51.22	25.97
O	48.78	74.03
Co-doped TiO_2 NPs		
Ti	48.01	23.91
O	50.66	75.55
Co	1.33	0.54

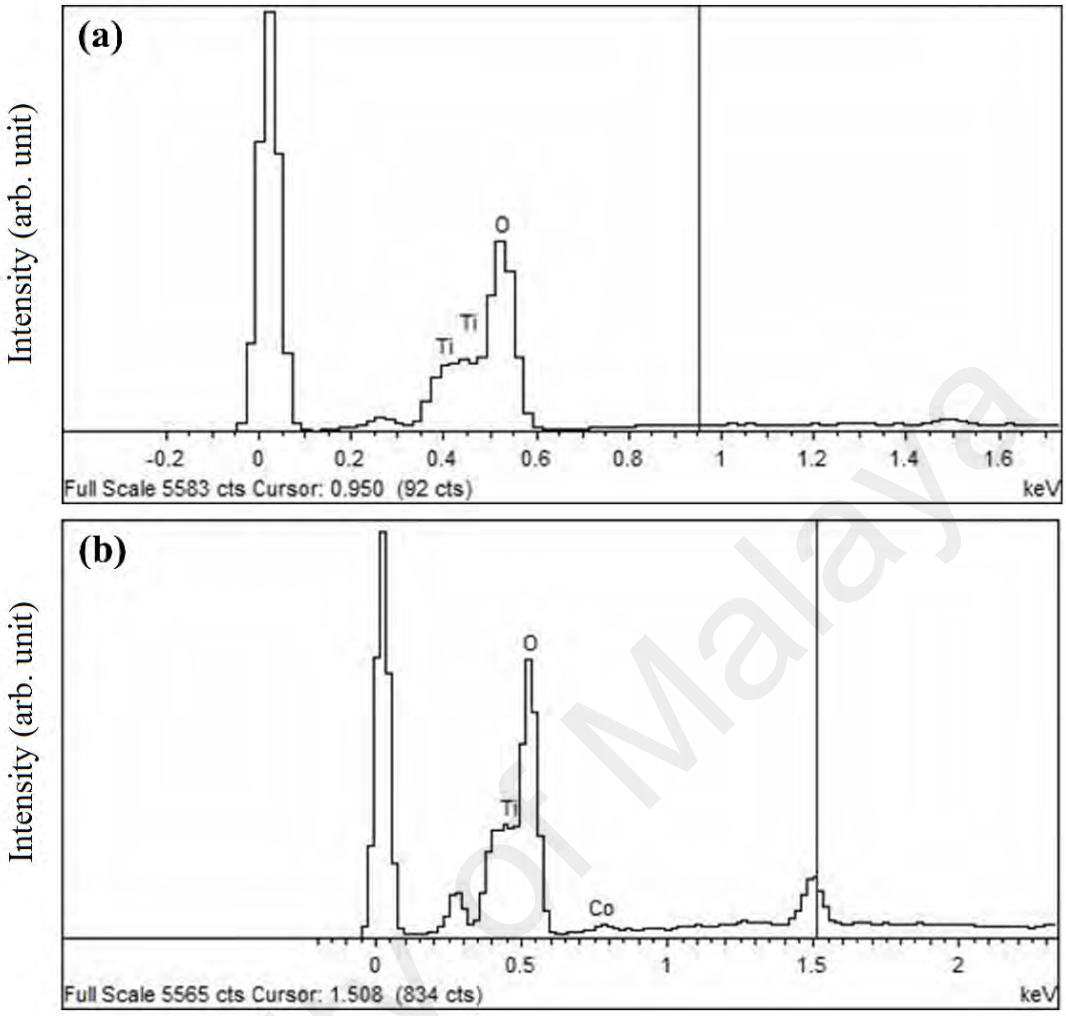

Figure 4.2: EDX spectra of (a) TiO_2 NPs and (b) Co-doped TiO_2 NPs heated at 500 ºC for of 5h

4.1.1.3 FT-IR spectra of TiO_2 NPs, Co-doped TiO_2 NPs, PPy NT, TiO_2/PPy NTCs and Co-doped TiO_2/PPy NTCs

Fig. 4.3 (a and b) depicts the FT-IR spectra of TiO_2 NPs, and Co-doped TiO_2 NPs heated at 500 °C for 5h. The absorption band observed at 3145.87 cm^{-1} in the TiO_2 NPs spectrum is due to the O–H stretching vibration frequency and also signals a strong hydrogen-bonding between OH and the surface of titanium dioxide (TiO_2). The characteristic peak at 1633.71 cm^{-1} is assigned to the H–O–H bending vibration mode of the observed water molecule(s) as well as Ti–OH. The peak between 740 cm^{-1} and 420 cm^{-1} in the TiO_2 NPs spectrum is assigned to the Ti–O–Ti vibration, which also

corresponds to the Ti–O bending mode of the TiO_2 (Cheng et al., 2012a; Cheng et al., 2012b; Luo et al., 2012; Shen et al., 2011). The Co-doped TiO_2 NPs and TiO_2 NPs have similar FT-IR spectrum. The shift of the characteristic peaks to lower wavenumbers is observed in the Co-doped TiO_2 NPs spectrum. This may be due to the doping of cobalt (Co) which decreases the aggregation of TiO_2. This affirms the Co–O formation with the substitution of Ti^{4+} in the TiO_2 lattice. The Co–O bond is formed in the TiO_2 lattice when Co^{2+} substitutes Ti^{4+}. Therefore, oxygen vacancies are easily set up in the doped TiO_2 when Ti^{4+} is substituted with Co^{2+} to maintain the charge balance. The number of oxygen decreases in the Co–O or Ti–O bonds in the doped TiO_2. This results in the decrease of the band frequency and the shift of Co–O band to lower wave numbers (Choudhury & Choudhury, 2012).

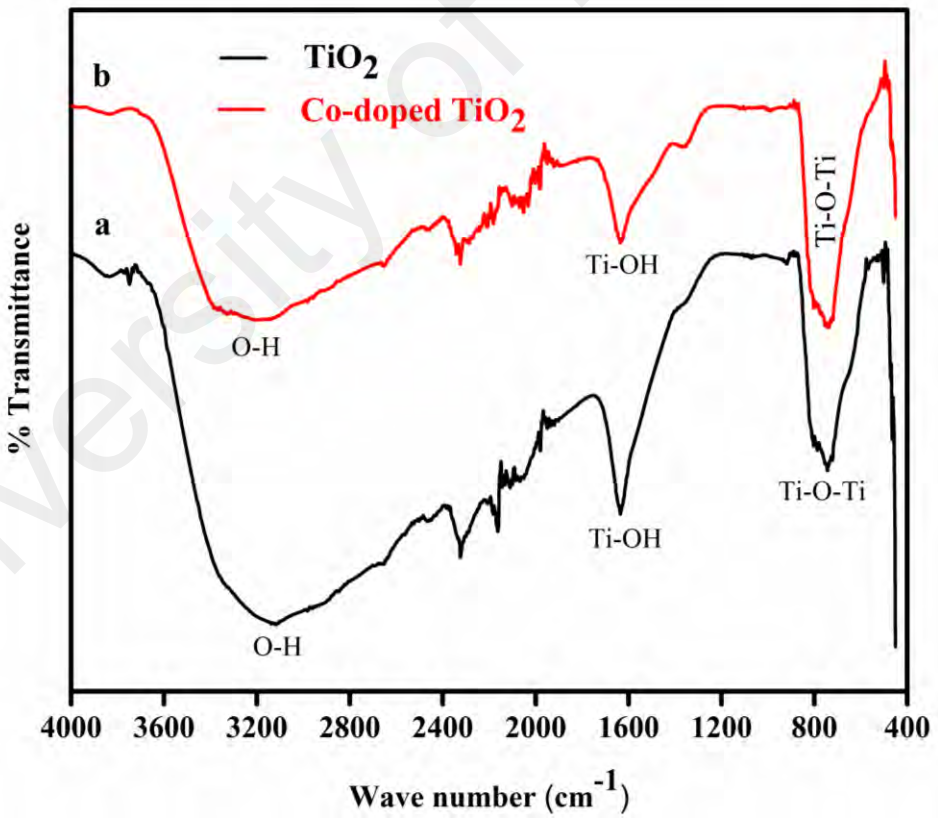

Figure 4.3: FTIR spectra of (a) TiO_2 NPs and (b) Co-doped TiO_2 NPs calcined at 500 ºC

Figure 4.4 (a, b, and c) shows the FTIR spectra of PPy NT, TiO_2/PPy NTCs, and Co-doped TiO_2/PPy NTCs. In the PPy NT spectrum, the bands between 1524 and 1439 cm^{-1} are due to the vibrations of the pyrrole rings, which correspond to the asymmetric and symmetric ring-stretching modes of PPy (Jiang et al., 2009). The absorption peak at 3787 cm^{-1} is due to the N–H stretching, the characteristic peak observed between 1284 and 1131 cm^{-1} are attributed to the C–N stretching vibration and the in-plane deformation vibration of NH^+. The band at 1018 cm^{-1} belongs to the C–H and N–H in-plane deformation vibrations. The spectra of the composites (TiO_2/PPy and Co-doped TiO_2/PPy) in Figure 4.4 (b and c) are almost similar to the PPy NT spectrum (Figure 4.4a); however, the bands between 775 cm^{-1} and 443 cm^{-1} in Figure 4.4(b and c) suggest the presence of TiO_2 NPs in the composites (Chowdhury et al., 2005; Strandwitz et al., 2010).

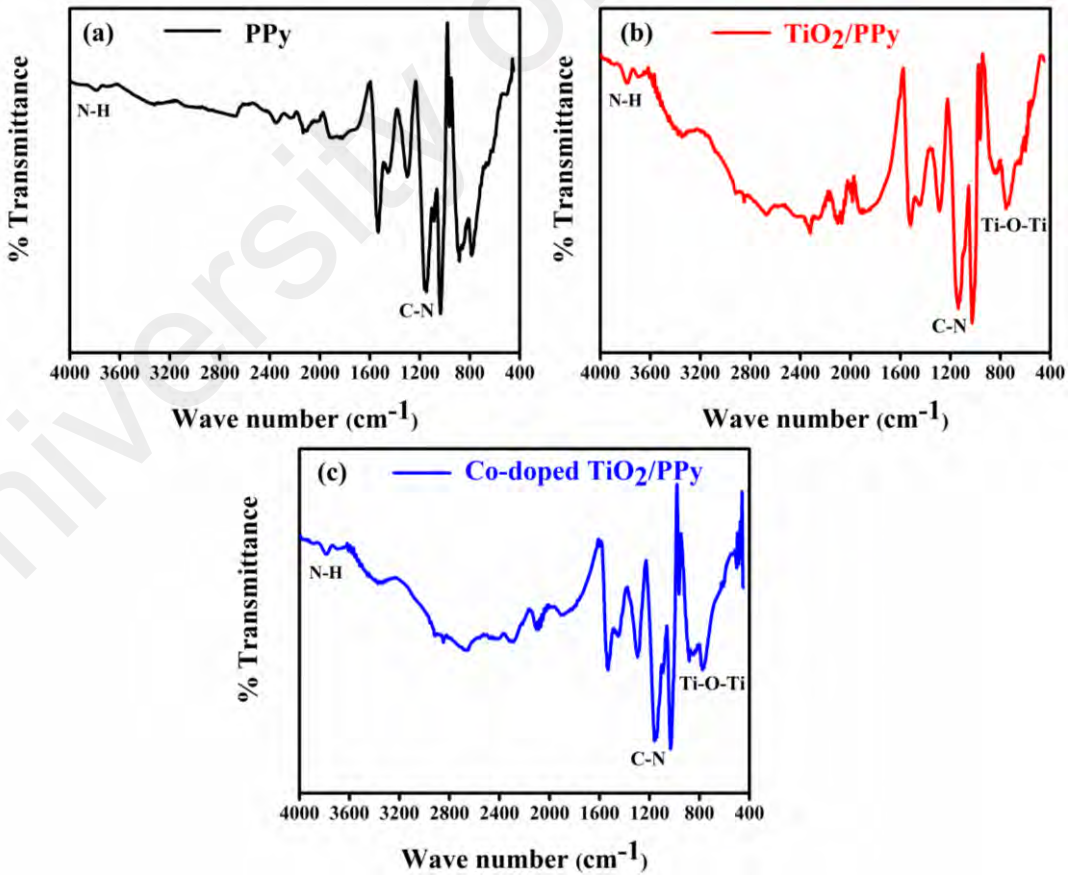

Figure 4.4: FTIR spectra of (a) PPy NTs, (b) TiO_2/PPy NTCs, and (c) Co-doped TiO_2/PPy NTCs

4.1.1.4 FESEM images of TiO_2 NPs, Co-doped TiO_2 NPs, TiO_2/PPy NTCs and Co-doped TiO_2/PPy NTCs

The FESEM micrographs of TiO_2 NPs, Co-doped TiO_2 NPs, TiO_2/PPy NTCs and Co-doped TiO_2/PPy NTCs are shown in Figure 4.5. The results suggest that the TiO_2 NPs and Co-doped TiO_2 NPs have a central influence and promote a homogeneous PPy core-shell-like morphology, leading to the complete coverage of TiO_2 NPs and Co-doped TiO_2 NPs by the PPy. The average diameters of TiO_2/PPy NTCs and Co-doped TiO_2/PPy NTCs were calculated to be around (220 ± 70) nm and (100 ± 30) nm respectively. The TEM images of TiO_2/PPy NTCs (Figure 4.6c) and Co-doped TiO_2/PPy NTCs (Figure 4.6d) show a core of the Co-doped TiO_2 and TiO_2 and a shell of the polymer. The TEM images confirm that the size of the Co-doped TiO_2/PPy NTCs is smaller than the TiO_2/PPy NTCs.

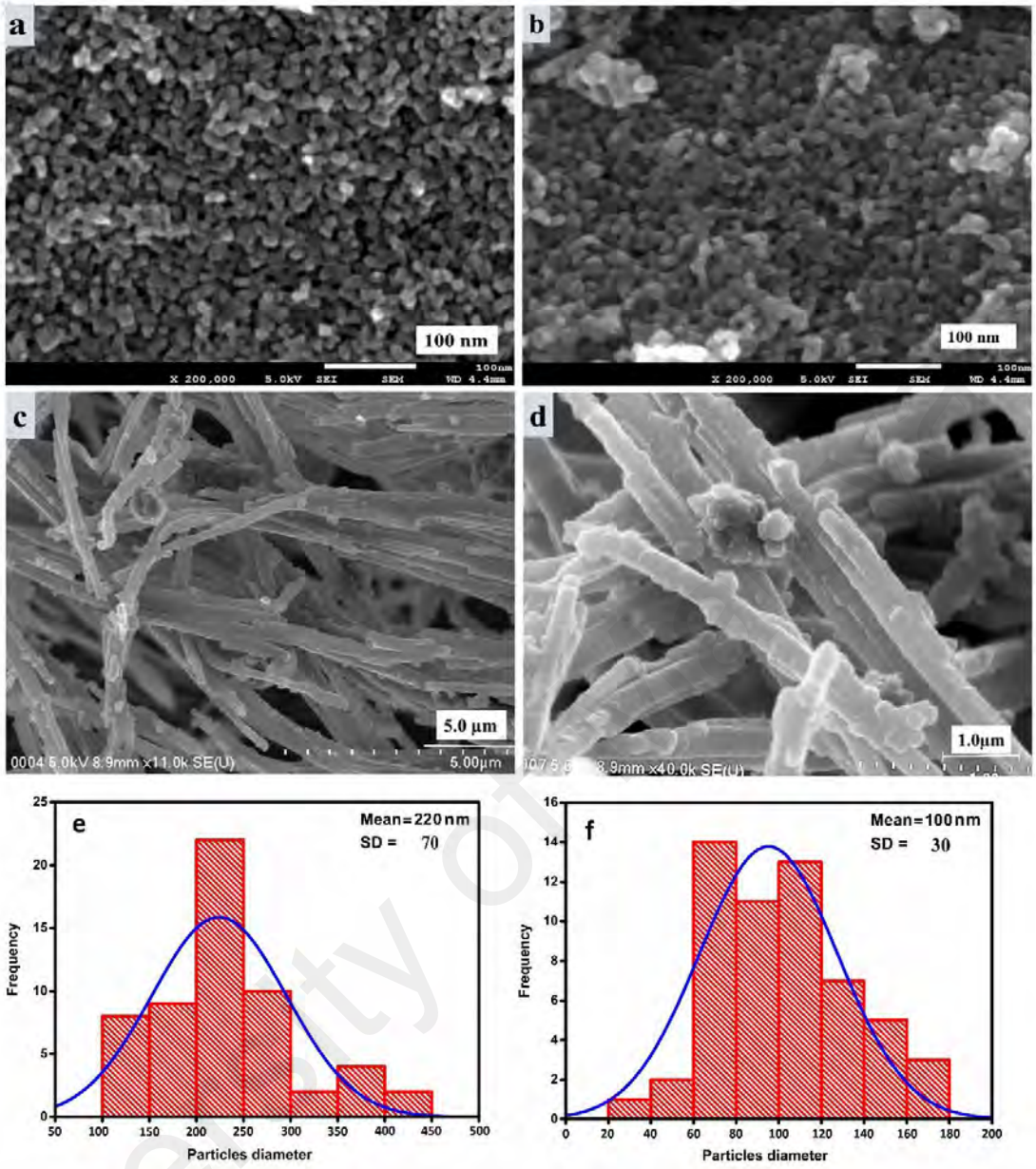

Figure 4.5: FESEM images of (a) Co-doped TiO_2 NPs, (b) TiO_2 NPs, (c) TiO_2/PPy NTCs, (d) Co- doped TiO_2/PPy NTCs and the size histograms of (e) TiO_2/PPy NTCs and (f) Co- doped TiO_2/PPy NTCs

4.1.1.5 TEM of TiO_2 NPs, Co-doped TiO_2 NPs, TiO_2/PPy NTCs and Co-doped TiO_2/PPy NTCs

TEM analysis was used to study the morphology and size of the TiO_2 NPs and Co-doped TiO_2 NPs. The calcined samples at 500 °C were suspended in ethanol separately and sonicated for 1.5 h. Figure 4.6 (a), (b), (c) and (d) are the TEM of TiO_2 NPs, Co-doped TiO_2 NPs, TiO_2/ PPy NTCs and Co-doped TiO_2/ PPy, respectively. As seen in

Figure 4.6 (a and b), the shape of nanoparticles is random, because the nanoparticles assume an indefinite shape with the increase of temperature and reaction time. The atomic proportion on the surface of the nanoparticle increases when the dimension of the nanoparticle becomes smaller. Under these circumstances, the atoms on the surface can influence the particle morphology. The atomic proportion on the surface of the particle decreases when the size of the particle grows larger, and at one point, the impact of the atoms on the surface becomes insignificant. The mean particle sizes of the TiO_2 NPs and Co-doped TiO_2 NPs from the TEM micrographs are calculated to be around 14.57 ± 2.63 and 11.39 ± 2.39 nm, respectively. The structure of the Co-doped TiO_2/PPy NTCs and TiO_2/PPy NTCs shows a nucleus of the Co-doped TiO_2 and TiO_2, and the PPy shell, as shown in Figure 4.6 (c and d). The TEM results show that the Co-doped TiO_2/PPy NTCs size is thinner than the TiO_2/PPy NTCs.

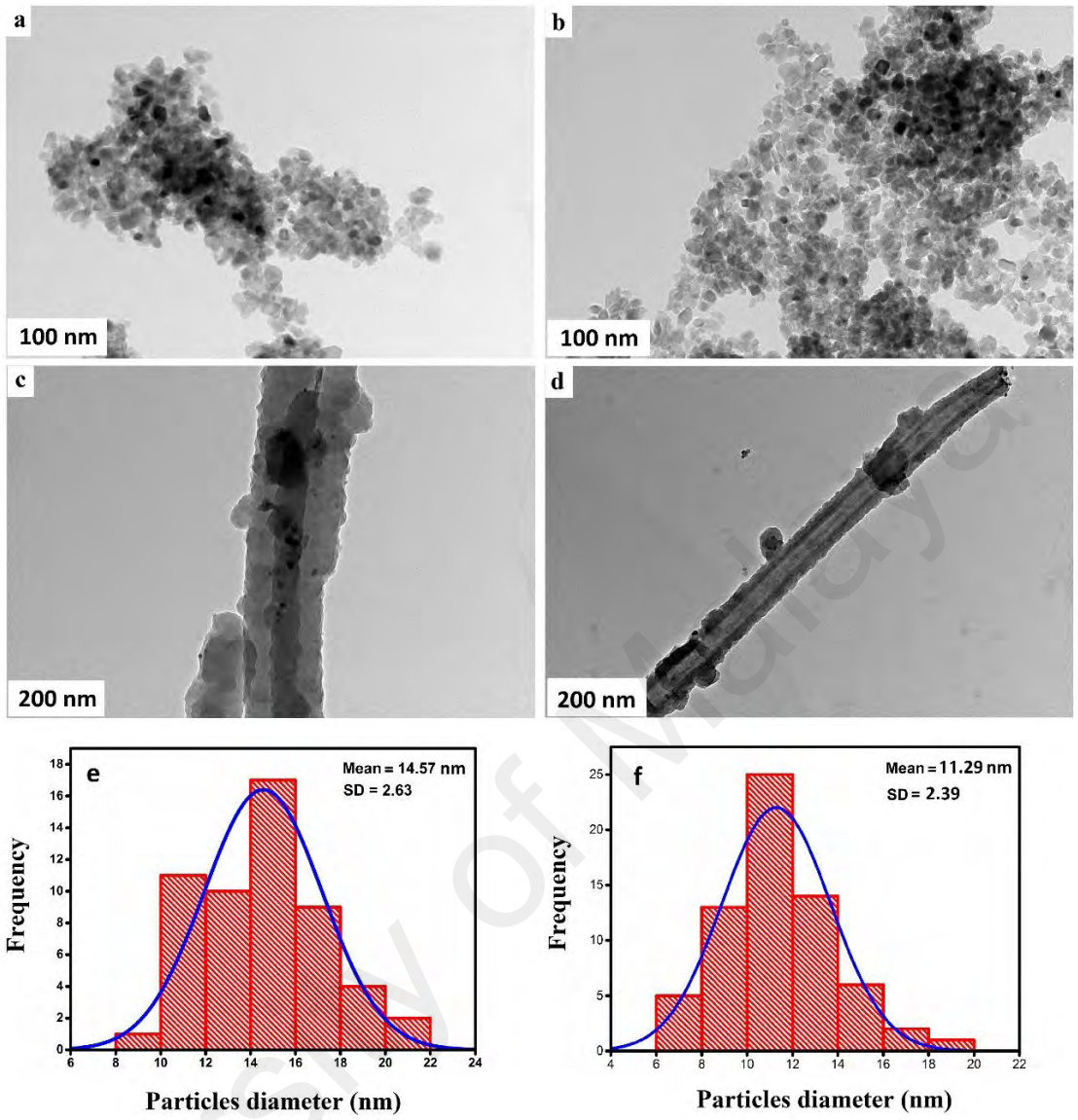

Figure 4.6: TEM images of (a) TiO_2 NPs, (b) Co-doped TiO_2 NPs, (c) TiO_2/PPy NTCs, (d) Co-doped TiO_2/PPy NTCs and size histograms of (e) TiO_2 NPs and (f) Co-doped TiO_2 NPs

4.1.1.6 Thermogravimetric analysis (TGA)

The thermal stability analysis of TiO_2 NPs, Co-doped TiO_2 NPs, TiO_2/PPy NTCs and Co-doped TiO_2/PPy NTCs was performed using (TGA) at a 10 °C /min heating rate. Figure 4.7 shows the TGA curves of the TiO_2 NPs, Co-doped TiO_2 NPs, TiO_2/PPy NTCs and Co-doped TiO_2/PPy NTCs respectively. The PPy, TiO_2/PPy and Co-doped TiO_2/PPy follow similar decomposition patterns and show a slow decomposition trend. The retention percentages of PPy NT, TiO_2/PPy and Co-doped TiO_2/PPy

nanocomposites at 795 °C are 14.48 %, 23.49 % and 48.39 %, respectively. The weight loss is due to the release of C, H and N moieties of PPy (Barkade et al., 2013; Han, 2009). As can be seen in the TGA of pure PPy (Figure 4.7), the weight loss of 5.84 % is observed at temperatures between 43 to 200 °C , which is attributed to the evaporation of moisture in the PPy while the weight loss at the temperature greater than 200 °C is due to the degradation of PPy (Zhu et al., 2010a). From the TGA results, it can be deduced that the Co-doped TiO_2/PPy NTCs exhibited higher thermal stability compared to the TiO_2/PPy NTCs. The improved thermal stability may be due to the strong interactions between Co-doped TiO_2 and PPy chains.

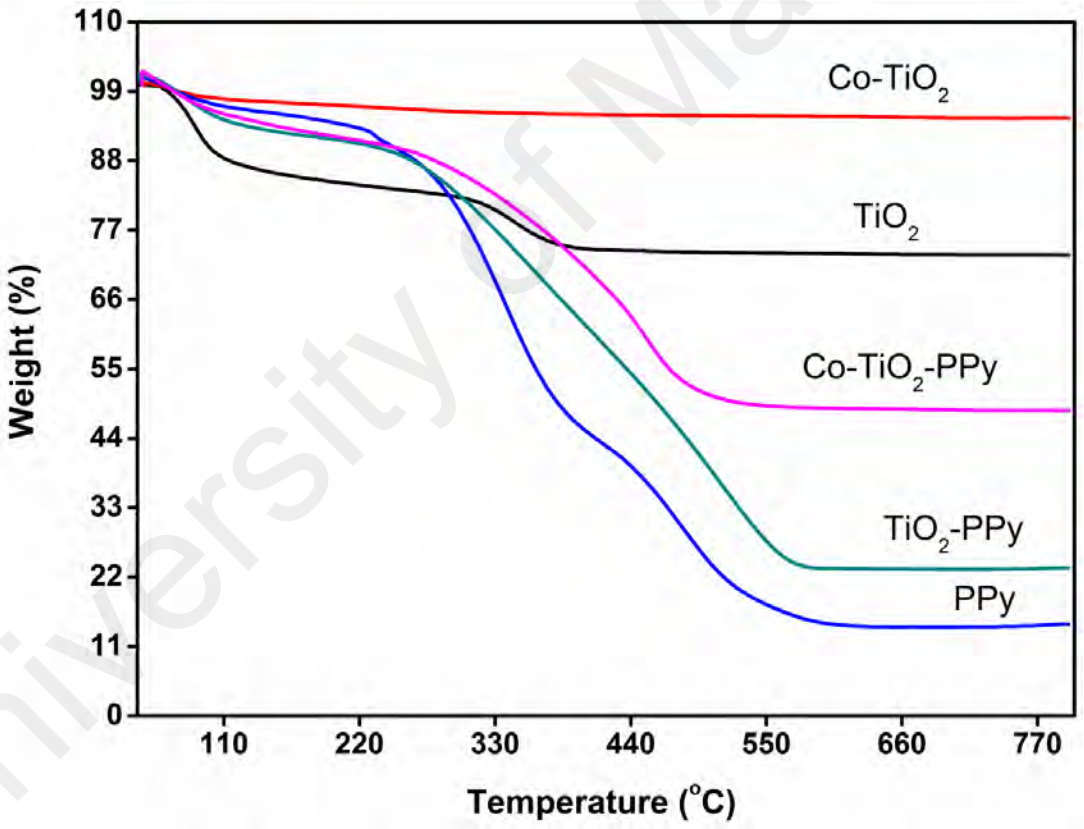

Figure 4.7: TGA curves of TiO_2, Co-doped TiO_2, PPy, TiO_2/PPy, and Co-doped TiO_2/PPy at a 10 °C /min heating rate

4.1.2 Electrochemical study

4.1.2.1 Open circuit potential (OCP) study

Figure 4.8 shows the OCP variation on immersion time for the AISI steel coated with (1) butvar + Co-doped TiO_2/PPy NTCs, (2) butvar + TiO_2/PPy NTCs, (3) butvar + PPy NT and (4) butvar + AISI steel. The coatings incorporated with the Co-doped TiO_2/PPy NTCs keeps higher potential values as compared to AISI steel coated with TiO_2/PPy NTCs, PPy NTs and butvar alone. As shown in Figure 4.8, the OCP value of the Co-doped TiO_2/PPy coated on the steel decreases from -0.018 V to -0.022 V after 10 days of exposure which may be due to the electrolyte penetration to the steel surface.

The decreasing trend of the OCP values from -0.018V to -0.209V of the coatings incorporated with Co-doped TiO_2/PPy for 30 days of exposure shows that the breakdown of coatings was gradual and not immediate. Therefore, the OCP values of Co-doped TiO_2/PPy indicate little changes between the 1 to 30 days of immersion which confirms the high performance of this coating on corrosion. The passivity of the coating incorporated with TiO_2/PPy drastically decreased after 10 days of exposure to a 3.5% solution of NaCl. Moreover, the OCP values of Co-doped TiO_2/PPy, TiO_2/PPy, PPy NT and steel after 30 days of immersion were -0.209V, -0.390V, -0.598V and -0.795V respectively. This confirms the superior performance of the coatings prepared with Co-doped TiO_2/PPy against corrosion, compared to the rest of the coatings prepared in this experiment.

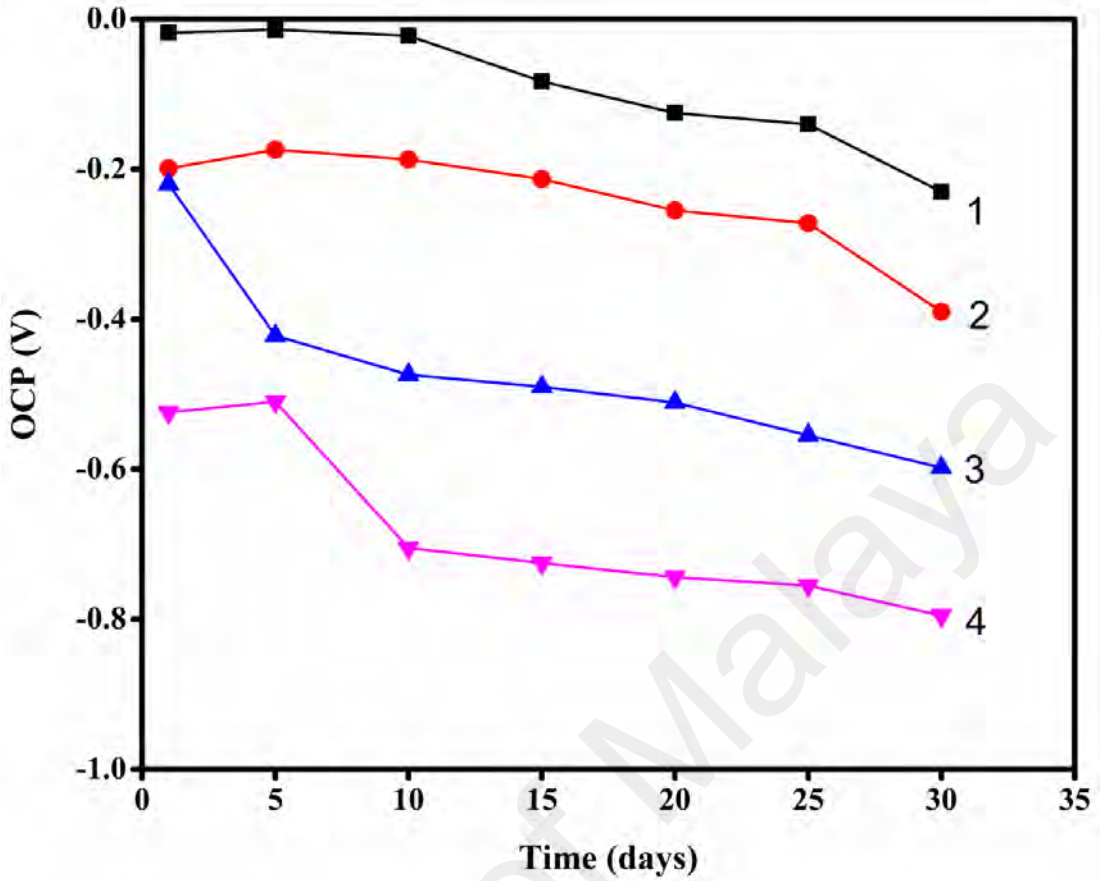

Figure 4.8: Open circuit potential with respect to immersion period (day) in solution of 3.5% NaCl for AISI steel coated with (1) Butvar + Co-doped TiO_2/PPy NTCs, (2) Butvar + TiO_2/PPy NTCs, (3) Butvar + PPy NTs, and (4) Butvar

4.1.2.2 Optical images of the coated steel

Figure 4.9 shows the impact of electrolyte (3.5% NaCl) on the coated AISI steel surface with (a) butvar alone, (b) butvar+ TiO_2/PPy NTCs and (c) butvar + Co-doped TiO_2/PPy NTCs before (left) and after 30 days of exposure period (right). The improvement in the corrosion resistance of AISI steel surface coated with butvar + TiO_2/PPy NTCs and butvar + Co-doped TiO_2/PPy NTCs coatings could be associated with the impact of PPy and the high resistive permeability of the coatings against corrosive species compared to the AISI steel coated with butvar alone. Furthermore, a comparison of all the images confirms that the number of pores on the coated AISI steel surface with butvar + Co-doped TiO_2/PPy is lower than the rest of the coatings after 30 days of exposure. As can be seen in Figure 4.9 (c_1 and c_2), the morphology of the PPy

still retained on the surface of the coated steel even after 30 days of exposure. These results prove that the corrosion resistance of the steel coated with the butvar + Co-doped TiO_2/PPy NTC is greater compared to the other coatings.

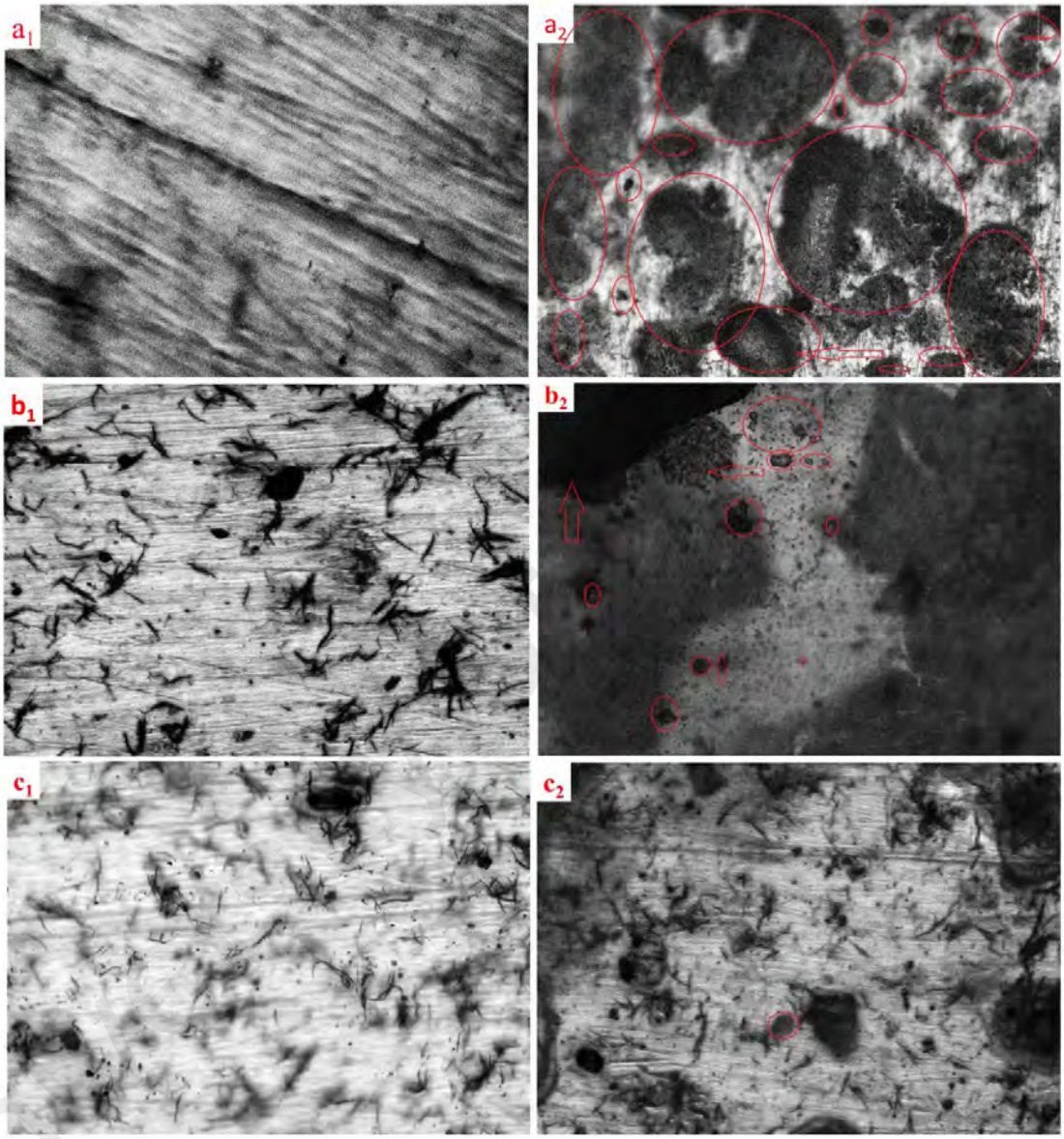

Figure 4.9: Optical microscope images of steel surface coated with (a) butvar, (b) butvar + TiO_2/PPy NTCs and (c) butvar + Co-doped TiO_2/PPy NTCs before (left) and after exposure of 30 days in 3.5% NaCl solution (right)

4.1.2.3 Potentiodynamic polarization measurements (Tafel)

Tafel plot is a powerful tool to estimate the instantaneous corrosion rate of a substrate (Neupane et al., 2015). Figure 4.10 presents the Tafel plots of coated AISI steel with butvar, PPy NT, TiO_2/PPy NTCs and Co-doped TiO_2/PPy NTCs after 30 days

exposure to a solution of 3.5% NaCl. The shift in the corrosion potential (E_{corr}) of the coated AISI steel with TiO_2/PPy NTCs and Co-doped TiO_2/PPy NTCs to more positive potentials were observed when compared with that of butvar and PPy NT. This shows that the corrosion process was subdued by the TiO_2/PPy NTCs and Co-doped TiO_2/PPy NTCs coatings. In addition, the corrosion current decreases from 2.941 x 10^{-6} A cm^{-2} (steel coated with butvar) to 1.487 x 10^{-9}A cm^{-2} (steel coated with TiO_2/PPy NTCs) and 3.107 x 10^{-11} A cm^{-2} (steel coated with Co-doped TiO_2/PPy NTCs). The potentiodynamic polarization results demonstrate that the rate of corrosion of the Co-doped TiO_2/PPy NTCs coating is lower compared to the PPy NT and TiO_2/PPy NTCs coatings. These results also confirm that the Co-doped TiO_2 NPs in the pigments increase the corrosion prevention of the steel surface. The electrochemical parameters obtained from the Tafel plots such as corrosion current density (i_{corr}), corrosion potential (E_{corr}), polarization resistance (R_p) and rate of corrosion (CR) are provided in Table 4.2. The corrosion current density was calculated using the GPES software installed in the Autolab PGSTAT 302N (Metrohm) from the intercept of the two linear segment of the Tafel slope.

Table 4.2: Values of i_{corr}, R_p, $E_{corr,}$ and corrosion rate (CR) of the coated steel with butvar, butvar + PPy NT, butvar + TiO_2/PPy NTCs, and butvar + Co-doped TiO_2/PPy NTCs after exposure for 30 days in a 3.5% NaCl solution.

Coated Sample	i_{corr} (Acm^{-2})	β_c (V/dec)	β_a (V/dec)	R_p ($M\Omega\ cm^2$)	E_{corr} (V)	CR (mpy)
1. Steel with butvar	2.011×10^{-6}	0.179	0.163	0.0020	-0.719	9.330×10^{-1}
2. Steel with butvar/PPy NT	9.512×10^{-8}	0.120	0.125	0.0217	-0.517	4.412×10^{-2}
3. Steel with butvar/TiO_2/ PPy NTCs	3.362×10^{-9}	0.251	0.238	2.454	-0.246	1.546×10^{-5}
4. Steel with butvar/Co-doped TiO_2/PPy NTCs	2.154×10^{-11}	0.170	0.187	203.7	-0.239	9.897×10^{-8}

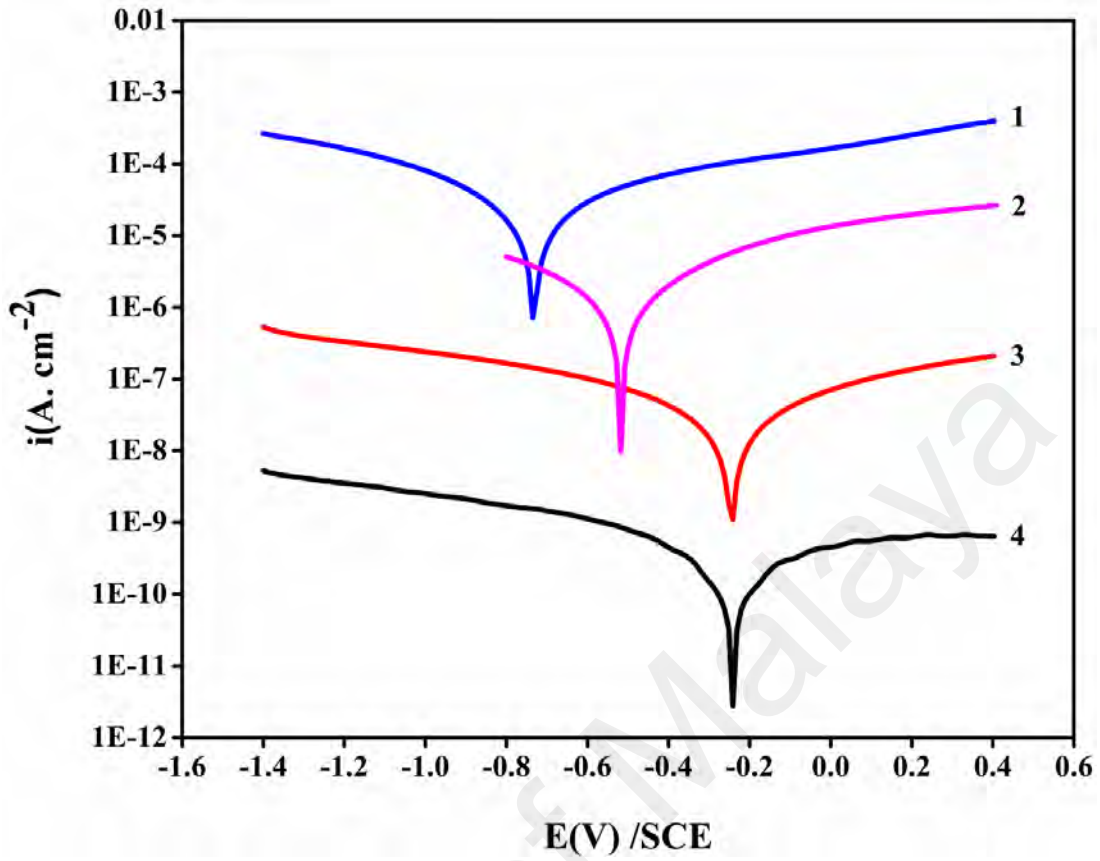

Figure 4.10: Tafel plots of AISI steel coated with (1) butvar, (2) butvar + PPy NTs (3) butvar + Co-doped TiO_2/PPy NTCs and (4) butvar + TiO_2/PPy NTCs

4.1.2.4 Electrochemical impedance spectroscopy (EIS) analysis

EIS was used to examine the behavior of the coated AISI steel with Co-doped TiO_2/PPy NTCs in the presence of 3.5% NaCl. Figure 4.11 shows the Nyquist plot of coated AISI steel in a different situation after 15 days of exposure. The Nyquist plot of the coated AISI steel with butvar (inset of Figure 4.11) shows two-time constants. The larger semicircle is associated with the coating resistance while the smaller semicircle is linked to the processes underneath the surface of the AISI steel (Araujo et al., 2001; Hasannejad et al., 2011; Pour-Ali et al., 2015). Meanwhile, the coated AISI steel with Co-doped TiO_2/PPy NTCs (Figure 4.11 (1)), TiO_2/PPy NTCs (Figure 4.11 (2)) and PPy NTs (Figure 4.11 (3)) respectively, show only one semicircle for the same immersion time in 3.5% NaCl solution. This result suggests that the real impedance (Z_{re}) increases

with the presence of TiO_2 NPs and Co-doped TiO_2 NPs in the lattice of PPy NT. The results obtained in Figure 4.12 prove the efficiency of the Co added to the TiO_2/PPy NTCs as a pigment for corrosion protection of steel surface.

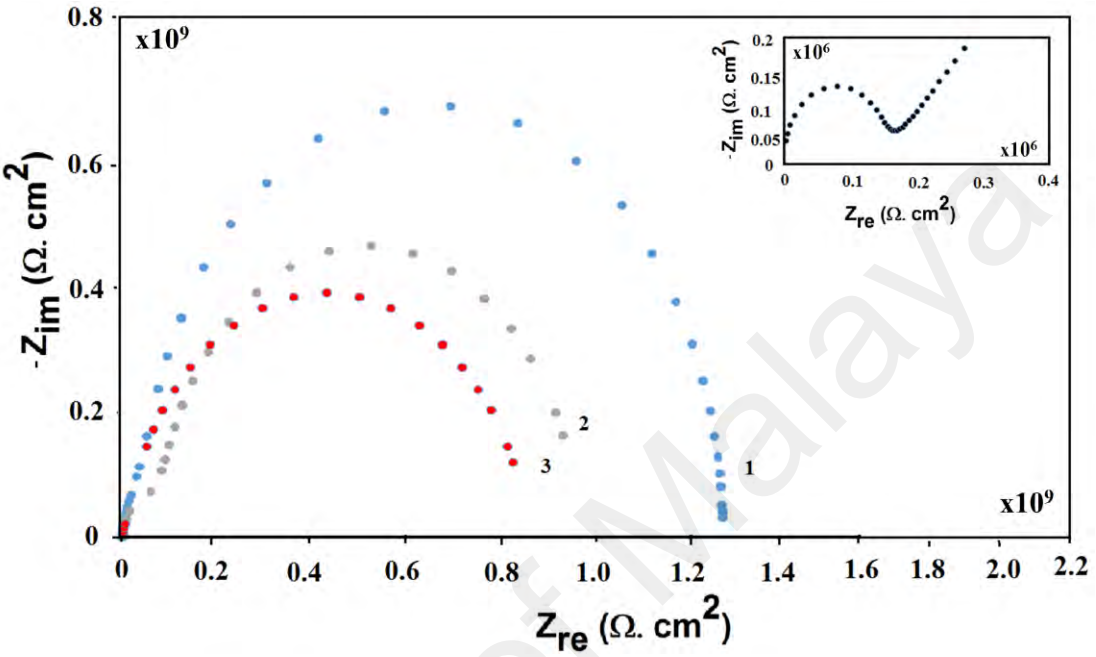

Figure 4.11: Nyquist plot of coated AISI steel with (1) Co-doped TiO_2/PPy NTCs, (2) TiO_2/PPy NTCs, (3) PPy NTs and inset coated AISI steel with butvar alone after 15 days of exposure to a solution of 3.5 % NaCl

Figure 4.12 displays the Bode plots of different coated steel after 1 day, 15 days and 30 days' of exposure period in a solution of 3.5% NaCl. The results suggest the influence of Co on the log |Z| value of the Co-doped TiO_2/PPy NTCs coating. The presence of Co in the TiO_2 matrix increases the efficiency of the coating compared to the other coatings. Although log |Z| value for the steel coated with TiO_2/PPy NTCs (Figure 4.13) is around 6.0 for the immersion period of 30 days, it is around 8.2 for the steel coated with Co-doped TiO_2/PPy NTCs incorporated butvar (Figure 4.13) for the same immersion time. This result proved that the Co-doped TiO_2/PPy NTCs has the best performance in the corrosion protection of steel surface.

From Figure 4.12, it can be seen that the log |Z| of the prepared coating with Co-doped TiO_2/PPy NTCs decreases with long immersion times, due to the penetration of electrolyte into the coated specimen. These results were further affirmed by the decrease

in the value of log |Z| as the immersion time increases (Figure 4.12). Hence, it can be deduced that the reduction in the value of log |Z| is due to the electrolyte penetration into the coated specimen. Therefore, an increase in the coating capacitance and reduction in the coating resistance are observed. The differences of log |Z| value in the initial seven days are small. However, as the exposure time increases, the log |Z| decreases from 9.2 for the first day and reaches around 8.2 at the end of the 30 days.

The Co-doped TiO_2/PPy NTCs/electrolyte impedance parameters were estimated by the simulations with the ZSimpWin software. The impedance behavior of the coatings was simulated using the $R_1(R_2Q)$ equivalent circuit model, and a good correlation between the experimental and simulated data was obtained.

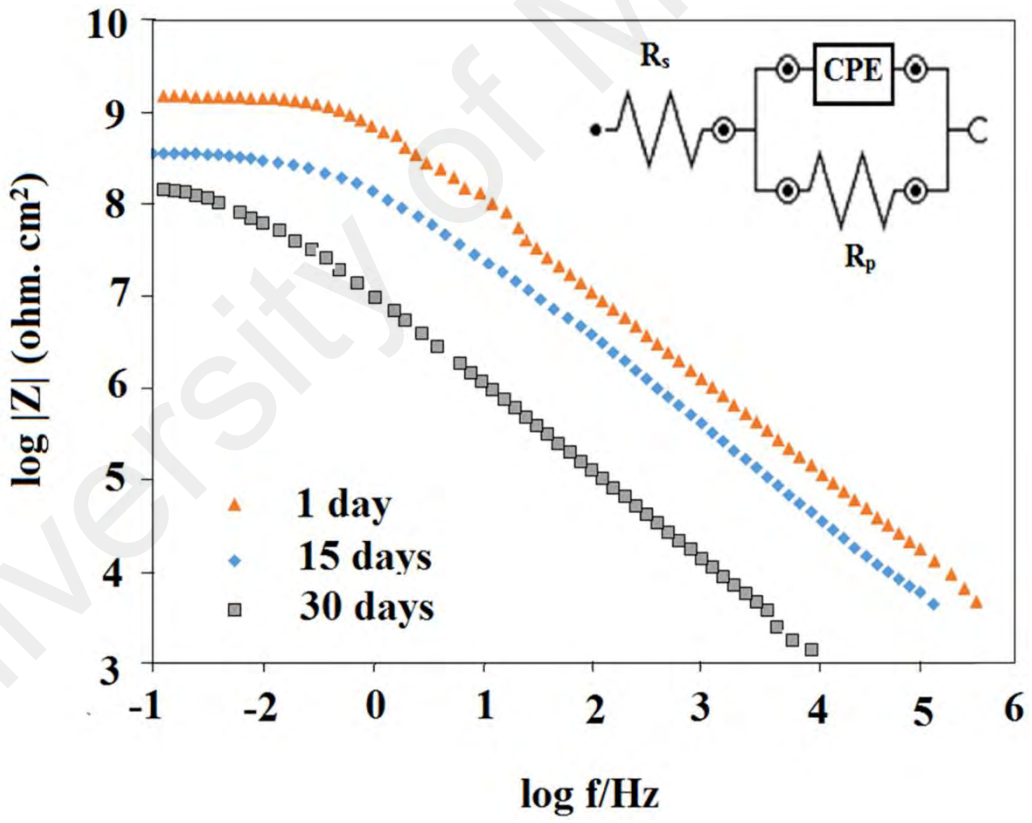

Figure 4.12: Bode plot of coated AISI steel with Co-doped TiO_2/PPy NTCs at different immersion time and the equivalent electrical circuit (inset) used for the EIS results simulation

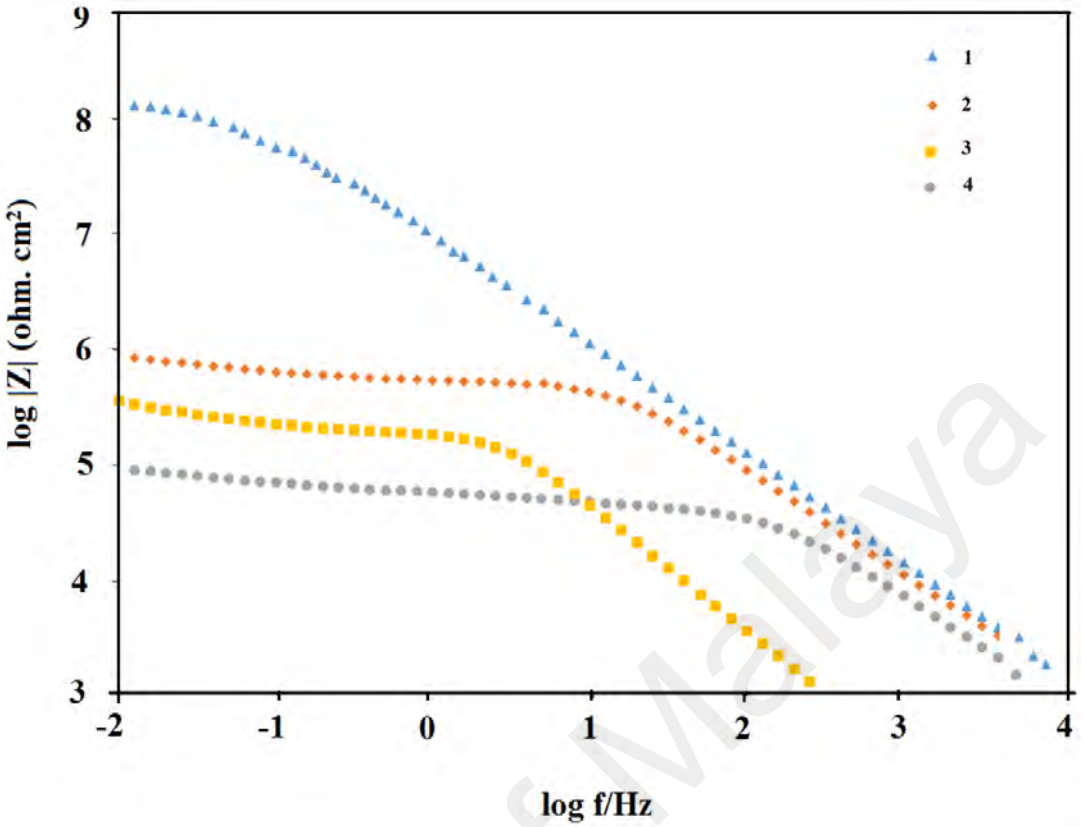

Figure 4.13: Bode plot of (1) Co-doped TiO_2/PPy NTCs, (2) TiO_2/PPy NTCs, (3) PPy NTs, and (4) butvar after 30 days' of immersion

Table 4.3: Impedance parameters of the Co-doped TiO_2/PPy NTCs containing butvar coated on AISI steel in a solution of 3.5 % NaCl.

Time (days)	R_c ($G\Omega\ cm^2$)	Q/Y_o ($n\Omega^{-1}\ S^n\ cm^{-2}$)	n	C_c ($nF\ cm^{-2}$)
1	6.820	0.0756	0.9290	0.0664
5	2.877	0.2086	0.9416	0.1924
10	2.647	0.2066	0.9432	0.1912
15	2.295	0.1968	0.9468	0.1679
20	1.990	0.2263	0.9347	0.1834
25	1.887	0.4699	0.8714	0.3107
30	0.2821	1.261	0.8807	0.4257

The circuit model comprises a series of components, which include; the electrolyte bulk solution resistance (Rs, or R_1 in the circuit model), the constant phase element

(CPE, or Q in the circuit model) due to the coating capacitance (C_c) and R_c (R_2 in the circuit model) as the coating resistance. The CPE was used instead of the pure capacitance in the simulation process due to the surface inhomogeneity and roughness (Zeybek et al., 2015a). The CPE impedance is given by Equation (4.2) (Hussin et al., 2015; Yuan et al., 2015):

$$Z(CPE) = \mathrm{Y}_o^{-1}(j\omega)^{-n} \tag{4.2}$$

Where Y_o is the constant phase element, n is the exponent of CPE and ω is the angular frequency. The CPE is reliant on the values of Q and the exponent "n". The conversion of Y_o to C_c is given by Equation (4.3) below (Azim et al., 2006; Jiang et al., 2015a; Jiang et al., 2015b).

$$C_c = \mathrm{Y}_o(\omega_m^{"})^{n-1} \tag{4.3}$$

where C_c is the coating capacitance, $\omega_m^{"}$ is the angular frequency at which Z imaginary is maximum.

The increase in coating weakness can be understood from the R_c and C_c values as a function of exposure time (Figure 4.14). It can be seen from Figure 4.14 that the R_c; indicating the degree of ionic movement through the coating in the electrolyte, decreases with the increase of exposure time, displaying a higher ionic conductivity and lower protective properties of the coatings due to the electrolyte diffusion (Pour-Ali et al., 2015; Vakili et al., 2015). The difference in the C_c values is an alternative approach to recognize the performance of the coating. The increase in the coating capacitance value (C_c) is due to the increase in the solution uptake (Pour-Ali et al., 2015). The effectiveness of the organic coating as an anti-corrosive agent may be attributable to the barrier effects which avert the electrolyte from reaching the steel surface (Schachinger et al., 2015).

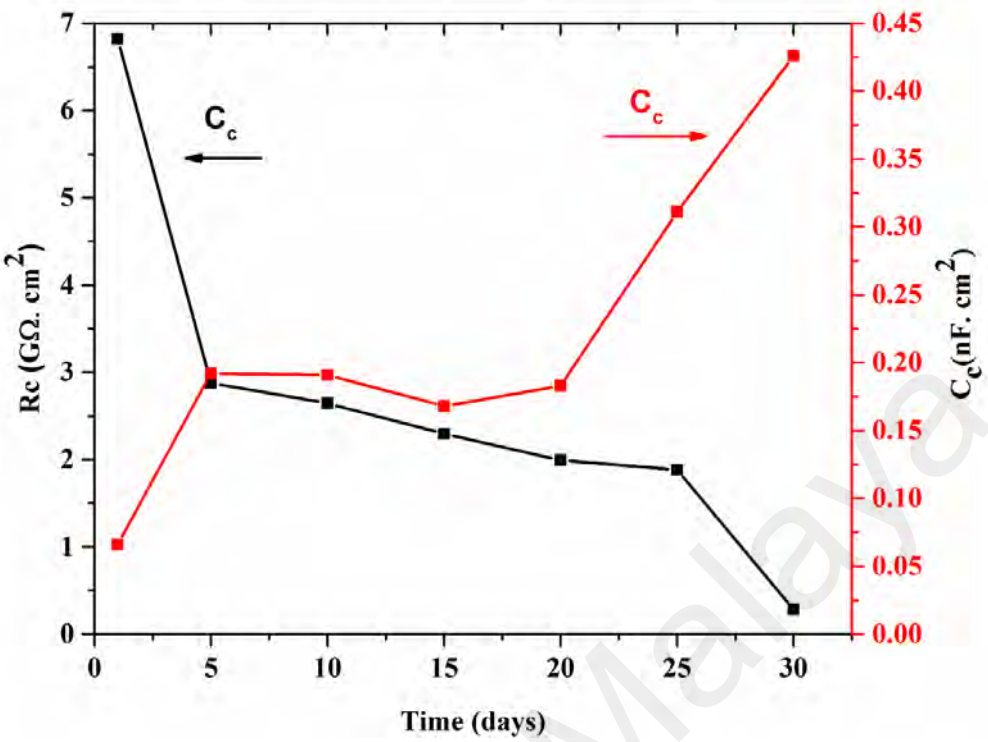

Figure 4.14: Variation of the resistance of the coating, R_c, and the capacitance of coating, C_c, of AISI steel coated with Co-doped TiO_2/PPy NTCs as a function of exposure time in a solution of 3.5 % NaCl

The Co-doped TiO_2/PPy NTCs offers superior protection of the AISI steel surface than the TiO_2/PPy, which is due to barrier effects preventing oxygen and moisture from reaching the surface of AISI steel resulting in the formation of a passive layer (Mahmoudian et al., 2012). The excellent anti-corrosion performance of the Co-doped TiO_2/PPy NTCs is because polymerization of pyrrole monomer in the vicinity of nanoparticles increases the dispersion of PPy, and more dispersion was observed with the prepared PPy in the presence of the Co-doped TiO_2 NPs compared to the PPy synthesized in the vicinity of TiO_2 NPs. The corrosion protection of PPy increases with the increase in PPy dispersion in the reaction medium. Also, the pyrrole polymerization in the presence of NPs can decrease the size of the PPy thereby increasing the surface contact area of the PPy, which can interact well with the steel surface. The TEM results confirmed that the size of Co-doped TiO_2/PPy NTCs was smaller than TiO_2/PPy NTCs thereby creating more interaction between the PPy nanotube and the AISI steel surface.

Therefore, the corrosion resistance of the coating incorporated with Co-doped TiO_2/PPy NTCs is higher than the TiO_2/PPy NTCs. The result of this reaction creates a new and very compact passive layer on coated AISI steel surface with Co-doped TiO_2/PPy, which can decrease the rate of corrosion in the presence of 3.5% NaCl solution. The OCP results in Figure 4.8 confirms this effect. It is realized that the redox reaction behavior of PPy plays an extraordinary role in its anti-corrosion properties. Also, an electroactive polymer such as PPy adds to the electric field formation at the steel surface, thereby decreasing the electron flow from the steel to the oxidant. Electroactive polymer coatings compel the formation of protective passive layers of metal oxides on the steel surface, and this can prevent the corrosion processes (Mahmoudian et al., 2012). Based on this, we can suggest that one of the metal oxides produced during the corrosion process of the coating incorporated with Co-doped TiO_2/PPy NTCs is cobalt (II) hydroxide $Co(OH)_2$. The formation of $Co(OH)_2$ on the steel surface could be due to the penetration of the electrolyte during the corrosion reaction. The increased surface area of the TiO_2/PPy with Co doping can reduce the charge transfer process across the electrolyte/steel interface and makes the coating more efficient against corrosion (Mahmoudian et al., 2011c).

4.2 Nanocomposites of Co-doped TiO_2/GO/PANI as effective anticorrosion agent for the protection of carbon steel.

4.2.1 Characterizations

4.2.1.1 XRD of Pure PANI, Co-doped TiO_2/PANI NCs, and Co-doped TiO_2/GO/PANI NCs.

XRD provides useful information about the structure of the samples. Figure. 4.15 represents the X-ray diffraction patterns of the (Ia) Co-doped TiO_2/GO/PANI, (Ib) Co-doped TiO_2/PANI, (Ic) Co-doped TiO_2, (Id) TiO_2, (IIa) PANI, and (IIb) GO. From the

XRD diffractograms, the Co-doped TiO_2 NPs are crystalline, and all the peak positions are similar to the results obtained by Su et al., (2012b). For PANI alone (Figure 4.15(IIa)), the peaks at 19.28° and 25.76° can be indexed to the (020) and (200) planes of PANI, respectively, in its amorphous emeraldine salt (Chaudhari & Kelkar, 1997). Figure 4.15(Ia and Ib) shows the presence of anatase TiO_2 peaks where all the peaks in the XRD spectra of the nanocomposites can be attributed to the anatase phase (JCPDS entry 00-001-0562) with the lattice constant of a = b = 3.78 Å and c = 9.52 Å. The PANI and GO diffraction peaks are too weak to be seen, which may be due to the presence of the Co-doped TiO_2 which could have blocked the crystallization of the PANI and the aggregation of GO (Lai et al., 2010).

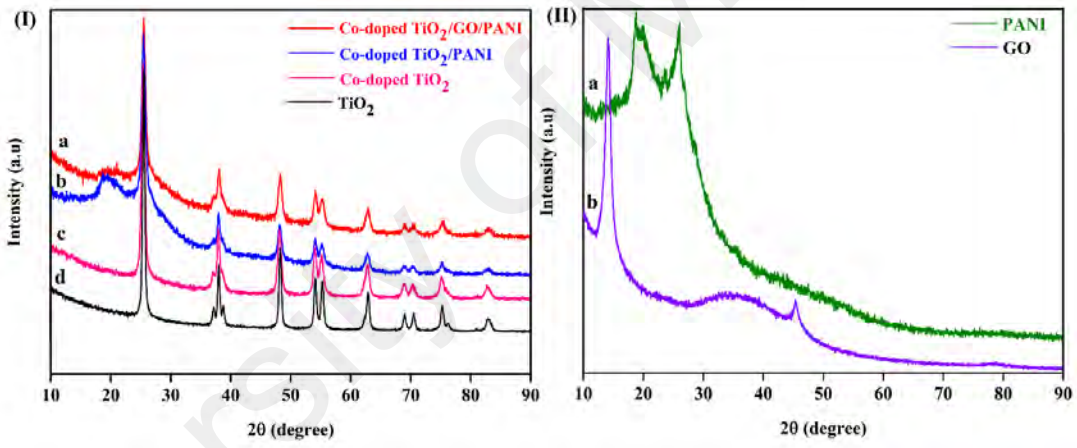

Figure 4.15: XRD pattern of (Ia) Co-doped TiO_2/GO/PANI NCs, (Ib) Co-doped TiO_2/PANI NCs, (Ic) Co-doped TiO_2, (Id) TiO_2, (IIa) PANI and (IIb) GO

4.2.1.2 FESEM images of GO, pure PANI NTs, Co-doped TiO_2/PANI NCs and Co-doped TiO_2/GO/PANI NCs

The FESEM of the nanocomposites is presented in Figure 4.16. Figure 4.16b reveals that the pure PANI has a rod-like structure while Figure 4.16c shows that the Co-doped TiO_2 NPs are spread on the surface of the PANI. Figure 4.16d is the FESEM image of the Co-doped TiO_2/GO/PANI composite which shows a flake-like graphene, rod-like PANI and nanoparticles of Co-doped TiO_2.

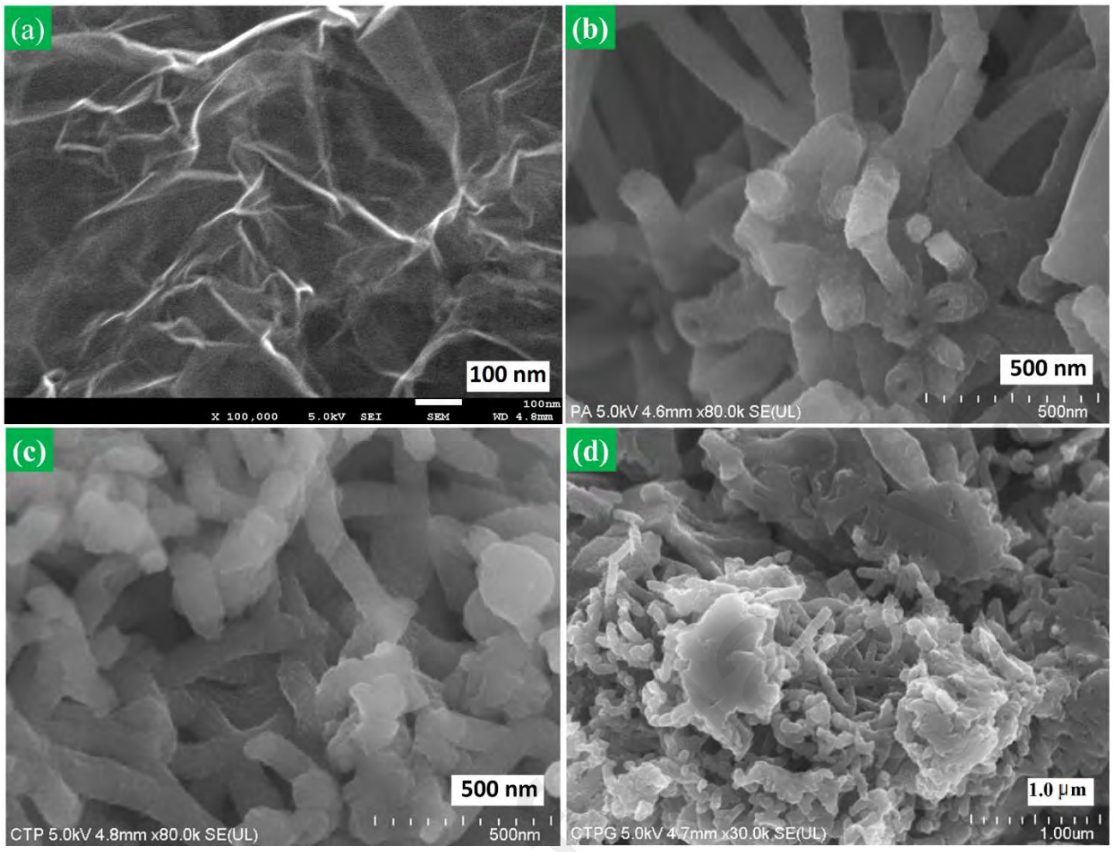

Figure 4.16: FESEM images of (a) GO, (b) pure PANI, (c) Co-doped TiO_2/PANI and (d) Co-doped TiO_2/GO/PANI

4.2.1.3 FTIR of GO, PANI NTs, Co-doped TiO_2/PANI NCs, and Co-doped TiO_2/GO/PANI NCs.

From Figure 4.18a, the band observed at 3376 cm^{-1} is assigned to O-H stretching vibrations, while the peaks at 1714 and 1620 cm^{-1} are attributed to the C=O stretching vibration in the COOH groups and C=C from the un-oxidized sp^2 CC bonds, respectively. The bands were seen at 1389, 1221 and 1048 cm^{-1} are due to the C-O vibrations in carboxy, epoxy and alkoxy groups in the GO, respectively (Kumar et al., 2012; Wang et al., 2009). Figure 4.18(b, c, and d) represents the FTIR spectra of PANI, Co-doped TiO_2/PANI, and Co-doped TiO_2/GO/PANI, respectively. The peaks at 1494, 1292 and 820 cm^{-1} in Figure 4.18b correspond to the stretching vibration modes of the C=C, C-N and C-C bonds, respectively, present in the benzenoid rings. The peaks observed at 1574 and 1294 cm^{-1} are attributed to the C=N and C-N stretching modes of

the quinoid rings, respectively. The peaks are seen at 3228, and 1142 cm^{-1} are assigned to the N-H stretching mode, and the plane is bending vibration mode of the C-H bond, respectively (Kang et al., 1998; Katoch et al., 2012). The bands at 1574, 1494 and 1294 cm^{-1} are attributed to the stretching mode of C=N, C=C and C-N, respectively, all shifted to lower wave numbers in Figure 4.18c. These shifts indicate that the bond strengths of C=N, C=C and C-N in the PANI are weakened in the presence of Co-doped TiO_2. This is due to the strong interaction between PANI and Co-doped TiO_2 NPs in the Co-doped TiO_2/PANI NC. This strong interaction is most likely due to the coordination of titania and nitrogen atoms in PANI because titania has a high tendency to form coordination compounds with the nitrogen atoms in PANI. Therefore, this interaction could result in the weakening of the C=N, C=C and C-N bond strengths present in PANI. More so, the H-bonding between Co-doped TiO_2 NPs and PANI could also contribute to the band shift to lower wavenumbers.

The possible structure of the PANI prepared in the presence of ferric chloride as oxidant is shown in Figure 4.17. It can be observed that the polymer unit is protonated and ionized with the chloride ion.

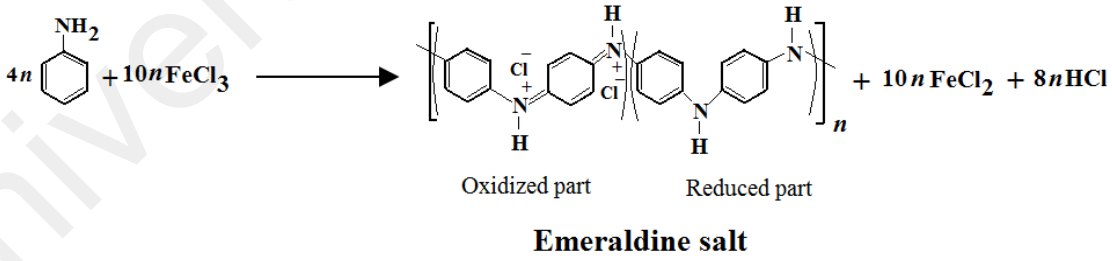

Figure 4.17: Possible polymerization reaction of aniline in the presence of an oxidant to form polyaniline

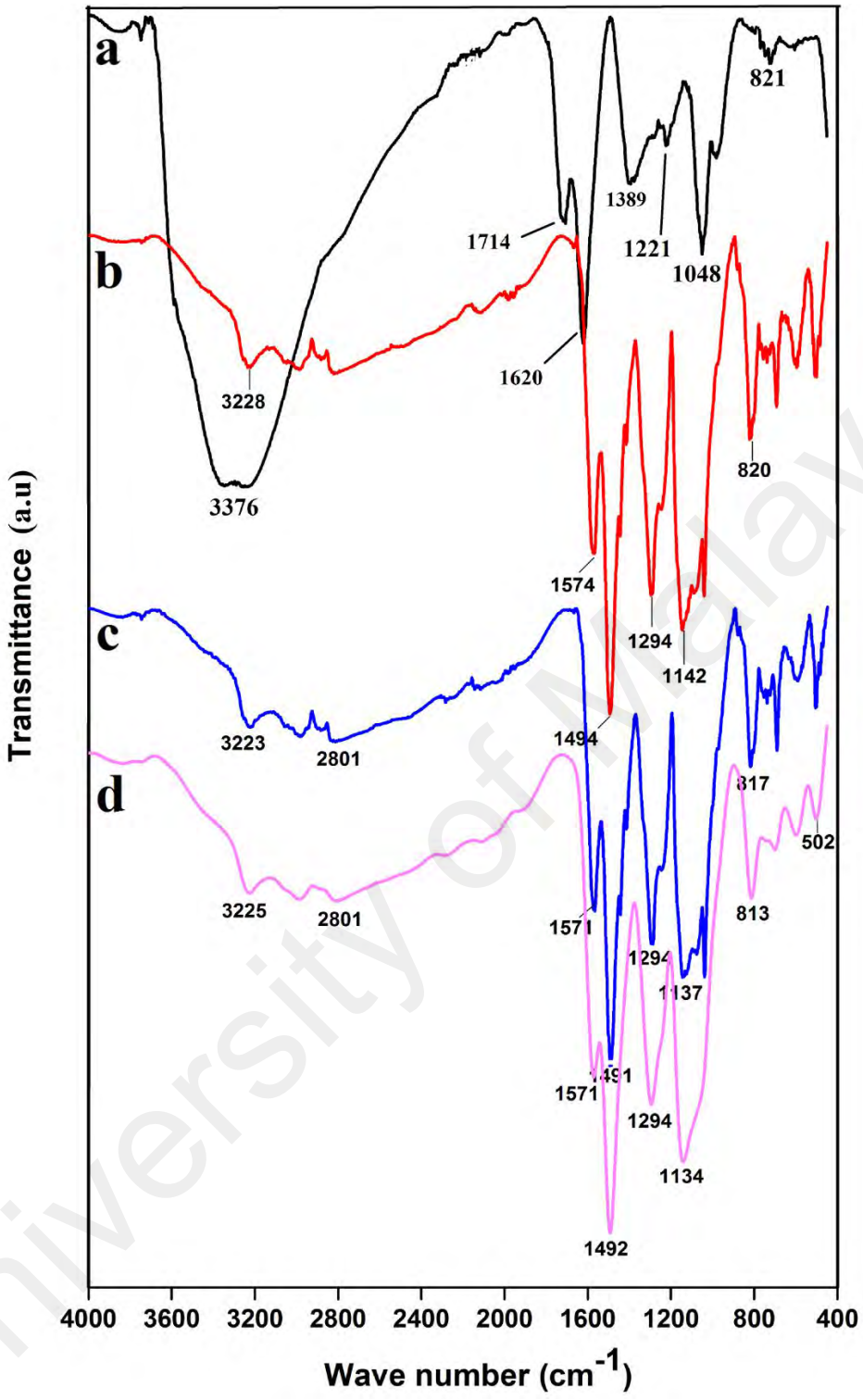

Figure 4.18: FTIR spectra of (a) GO, (b) PANI, (c) Co-doped TiO_2/PANI NCs, and (d) Co-doped TiO_2/GO/PANI NCs

4.2.1.4 TEM images of Co-doped TiO_2/PANI NCs and Co-doped TiO_2/GO/PANI NCs, Raman spectrum of GO and the elemental mapping of Co-doped TiO_2/GO/PANI NCs

Figure 4.19 shows the TEM images of the PANI nanocomposites. Figure 4.19a reveals a rod-like structure of the Co-doped TiO_2 nanocomposites. Obviously, it can be seen that the Co-doped TiO_2 NPs are randomly distributed in the PANI matrix. A similar morphology was also observed in Figure 4.19b, but with a sharp decrease in the diameter of the PANI nanocomposites. The decrease in size is likely due to the presence of GO in the nanocomposite; it can be observed that the PANI covers most of the GO sheets. Figure 4.19c shows the Raman spectrum of GO which reveals a D band at 1347 cm^{-1} and a G band at 1601 cm^{-1}, respectively. The elemental distribution in the Co-doped TiO_2/GO/PANI is shown in Figure 4.19d.

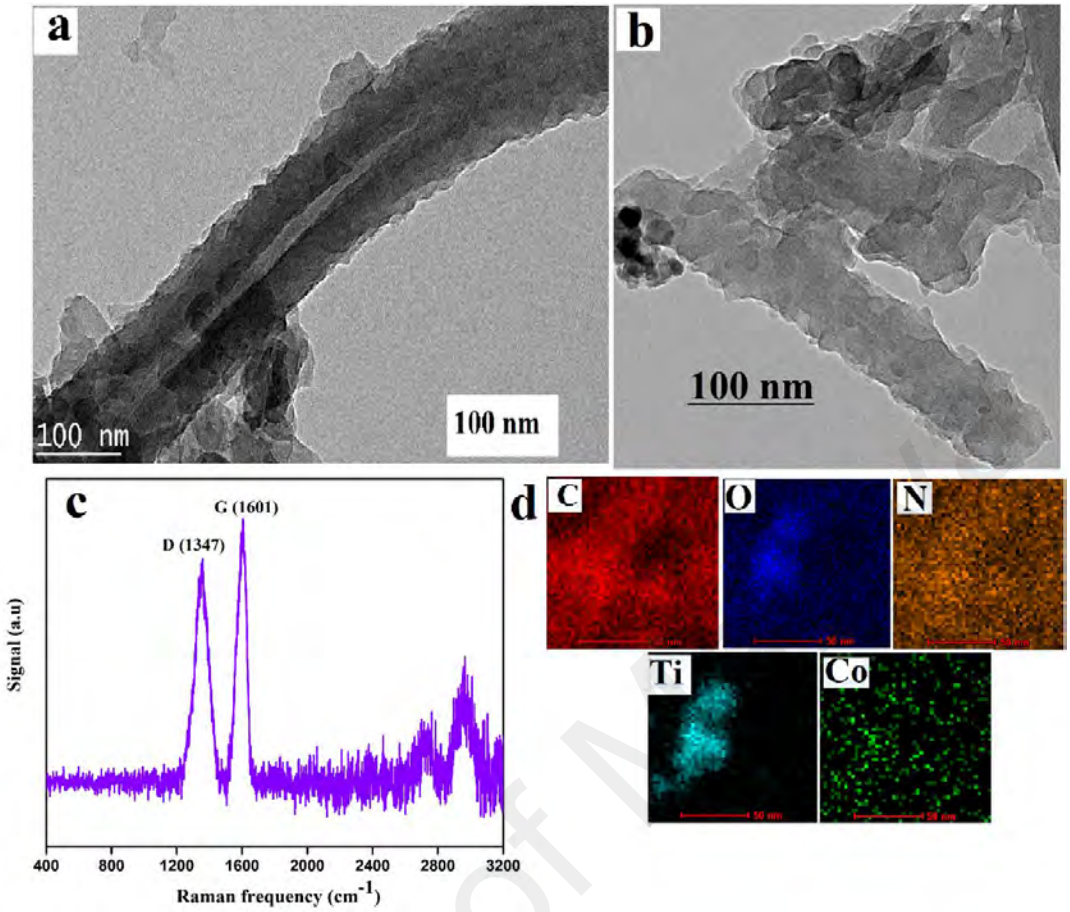

Figure 4.19: TEM images of (a) Co-doped TiO_2/PANI and (b) Co-doped TiO_2/GO/PANI; Raman spectrum of (c) GO; and (d) elemental mapping images of Co-doped TiO_2/GO/PAN

4.2.2 Corrosion study

4.2.2.1 Open circuit potentials

Figure 4.20 shows the variation of OCP with regards to the immersion time for the low carbon steel coated with (1) butvar incorporated with Co-doped TiO_2/GO/PANI NCs, (2) butvar incorporated with Co-doped TiO_2/PANI NCs, (3) butvar incorporated with PANI and (4) butvar alone. The coatings incorporated with the Co-doped TiO_2/GO/PANI NCs has higher potential compared to low carbon steel coated with Co-doped TiO_2/PANI NCs, PANI and butvar alone. As shown in Figure 4.20, the OCP value of the Co-doped TiO_2/GO/PANI coated on low carbon steel decreases from 0.278 V to 0.046 V after 11 days of immersion time which could be due to the electrolyte penetration to the steel surface.

The decreasing trend of the OCP values from 0.278 V to -0.072 V of the coatings incorporated with Co-doped TiO_2/GO/PANI NCs from the first day to 30 days of immersion time shows that the breakdown of coatings was gradual and not immediate. Therefore the OCP values of Co-doped TiO_2/GO/PANI NCs indicate only small changes between 1 to 30 days of immersion time which confirms the high performance of this coating for corrosion protection. However, the passivity of the coating incorporated with PANI drastically decreased just after 10 days of immersion in 3.5% NaCl solution. Moreover, the OCP values of Co-doped TiO_2/GO/PANI NCs, Co-doped TiO_2/PANI NCs, PANI and low carbon steel after 30 days of immersion were -0.072 V, -0.552 V, -0.688 V and -0.923 V respectively. This confirms the excellent performance of the coatings prepared with Co-doped TiO_2/GO/PANI NCs against corrosion, compared to the coatings incorporated with Co-doped TiO_2/PANI and PANI, respectively.

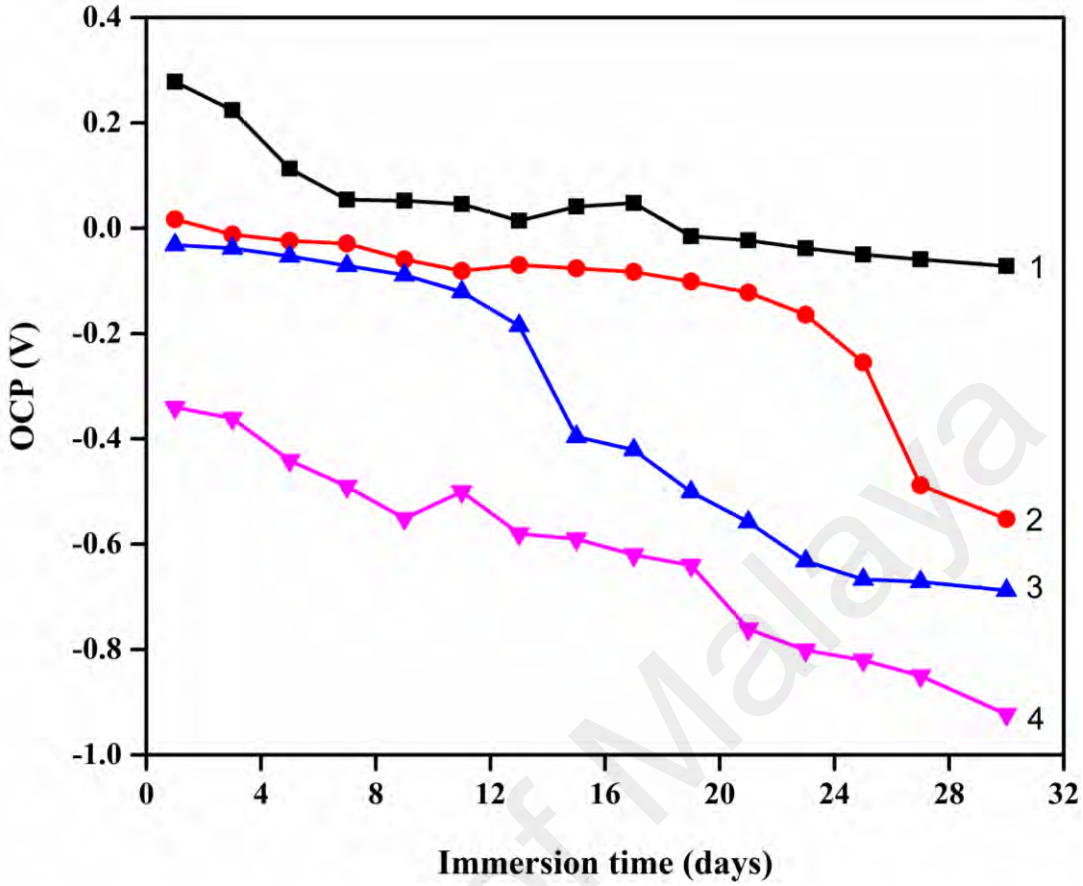

Figure 4.20: The variation of the open circuit potential (OCP) with the immersion time (day) 3.5% NaCl solution for low carbon steel coated with (1) Butvar + Co-doped TiO_2/GO/PANI NCs, (2) Butvar + Co-doped TiO_2/PANI NCs, (3) Butvar + PANI, and (4) Butvar

4.2.2.2 Optical images of the coated steel before and after corrosion study

Figure 4.21 shows the effect of electrolyte (3.5% NaCl) on low carbon steel surface coated with (a) butvar alone, (b) butvar + Co-doped TiO_2/PANI NCs and (c) butvar + Co-doped TiO_2/GO/PANI NCs before (up) and after 30 days of immersion time (down). The enhancement in the corrosion resistance of the low carbon steel surface coated with butvar + Co-doped TiO_2/PANI NCs and coated with butvar + Co-doped TiO_2/GO/PANI NCs is attributed to the high resistive permeability of the coatings against corrosive environments compared to the low carbon steel coated with butvar alone. The images in Figure 4.21 also indicate that the number of pores on the low carbon steel surface coated with butvar + Co-doped TiO_2/GO/PANI is lower than the rest of the coatings after an immersion time of 30 days. From Figure 4.21 (b_1 and c_1), the morphology of the PANI

is still maintained on the surface of the low carbon steel coatings even after 30 days of immersion time. These results also demonstrate that the low carbon steel coated with butvar + Co-doped TiO_2/GO/PANI NCs shows better corrosion resistance compared to the other coatings.

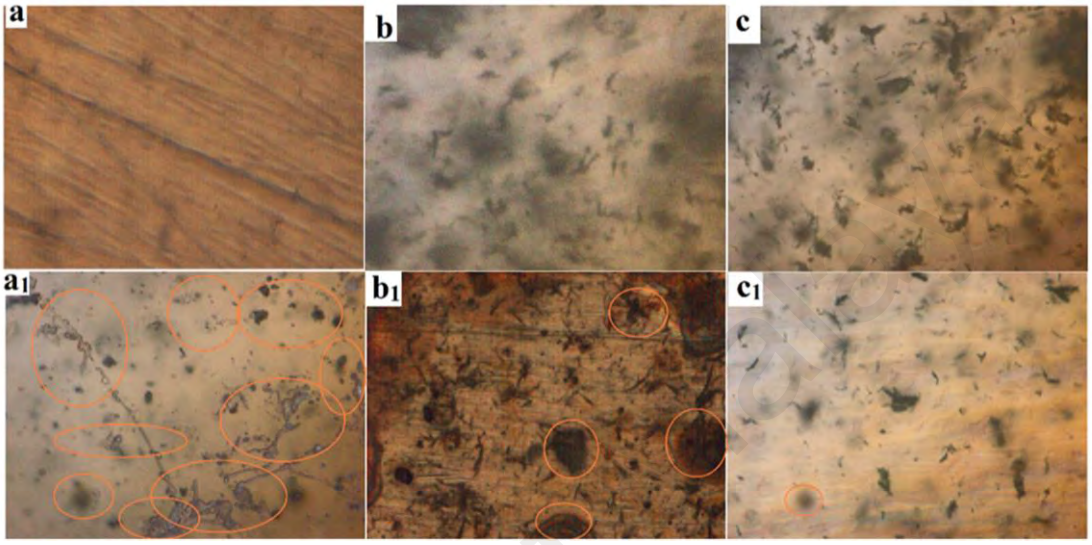

Figure 4.21: Images of low carbon steel coated with (a) butvar alone, (b) Co-doped TiO_2/PANI NCs and (c) Co-doped TiO_2/GO/PANI NCs before (up) and after exposure of 30 days in 3.5% NaCl solution (down)

4.2.2.3 Potentiodynamic polarization study

Tafel analysis is an imperative tool to evaluate the instantaneous corrosion rate of steel (Neupane et al., 2015). Figure 4.22 shows the Tafel plots of low carbon steel coated with butvar, PANI, Co-doped TiO_2/PANI NCs and Co-doped TiO_2/GO/PANI NCs after 30 days of immersion in 3.5% NaCl solution. The shift in the corrosion potential (E_{corr}) of the low carbon steel coated with Co-doped TiO_2/PANI NCs and Co-doped TiO_2/GO/PANI NCs to more positive regions were observed compared to that of butvar and PANI. Furthermore, the corrosion current decreases from 2.011×10^{-6} A cm^{-2} (steel coated with butvar) to 5.172×10^{-12} A cm^{-2} (steel coated with Co-doped TiO_2/PANI NCs) and 2.261×10^{-14} A cm^{-2} (steel coated with Co-doped TiO_2/GO/PANI NCs). The Tafel curve analysis indicates that the corrosion rate of the low carbon steel coated with Co-doped TiO_2/GO/PANI NCs is lower compared to the coatings

incorporated with Co-doped TiO_2/PANI NCs and PANI respectively. These results also confirm that the incorporation of Co-doped TiO_2 NPs and GO in the pigments could increase the corrosion resistance of the low carbon steel. The electrochemical parameters obtained from the Tafel curves such as corrosion potential (E_{corr}), corrosion current density (i_{corr}), polarization resistance (R_p) and corrosion rate (CR) are listed in Table 4.3.

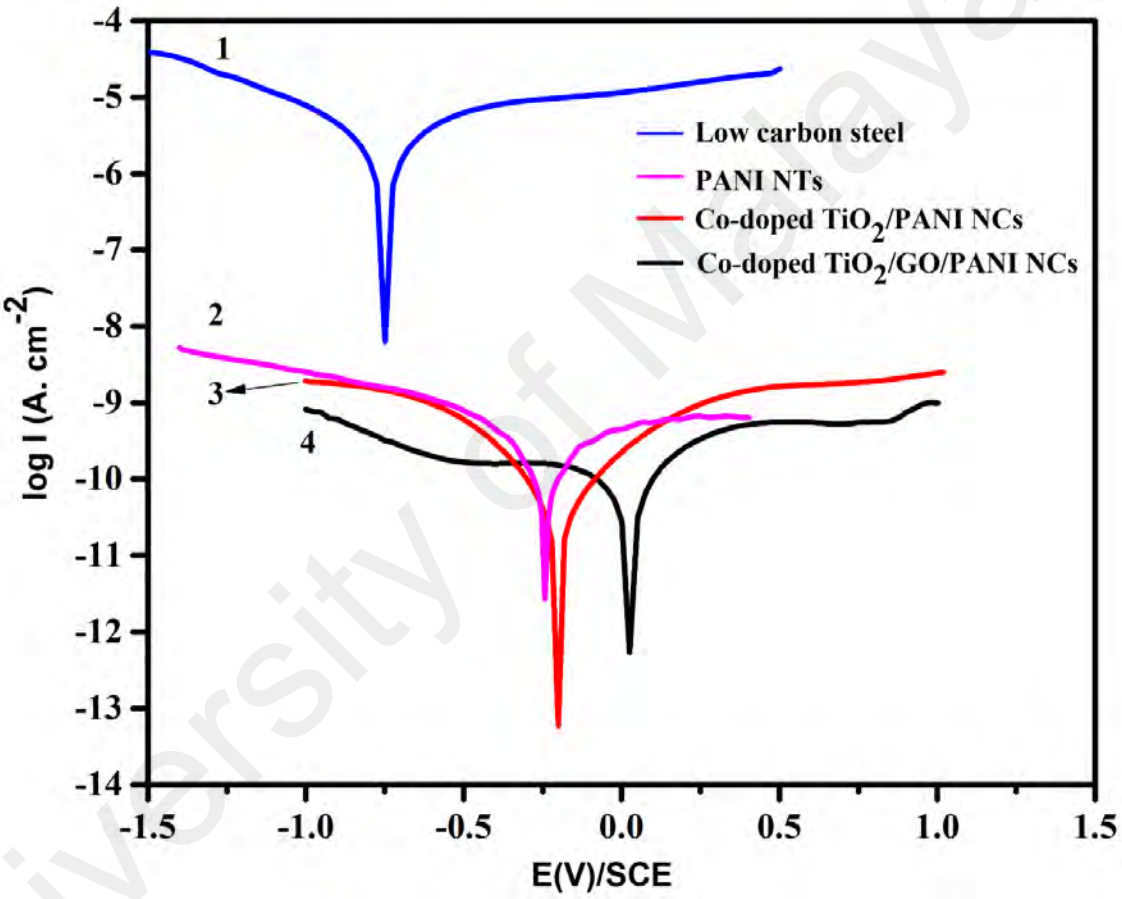

Figure 4.22: Tafel curves of low carbon steel coated with (1) butvar, (2) butvar + PANI (3) butvar + Co-doped TiO_2/PANI NCs and (4) butvar + Co-doped TiO_2/GO/PANI NCs

Table 4.4: E_{corr}, β_c, β_a, R_p, i_{corr} and corrosion rate (CR) values of the low carbon steel coated with butvar, butvar + PANI, butvar + Co-doped TiO_2/PANI NCs, and butvar + Co-doped TiO_2/GO/PANI NCs after 30 days of immersion time in 3.5% NaCl solution

Low carbon steel	E_{corr} (V)	β_c (V/dec)	β_a (V/dec)	R_p (MΩ cm^2)	i_{corr} (Acm^{-2})	CR (mpy)
1. coated with butvar	-0.719	0.179	0.163	0.0020	2.011×10^{-6}	9.330×10^{-1}
2. coated with butvar/PANI NTs	-0.249	0.146	0.151	0.1624	1.870×10^{-7}	8.676×10^{-2}
3. coated with butvar/Co-doped TiO_2/PANI NCs	-0.164	0.156	0.165	686.20	5.172×10^{-12}	2.399×10^{-6}
4. coated with butvar/Co-doped TiO_2/GO/PANI NCs	0.070	0.007	0.007	818.2	2.261×10^{-14}	1.049×10^{-8}

4.2.2.4 EIS study

EIS is a powerful tool to study the electrochemical deterioration of metals and their coated samples. The Bode and Nyquist plots are the two basic plots in EIS that can be used to examine the corrosion properties of the coated materials on the steel sample. The EIS measurements were carried out between100 kHz to 10 mHz frequency range, with an AC perturbation of 5 mV around the OCP. Figure 4.23 shows the Nyquist plots of the low carbon steel coated with (a) Co-doped TiO_2/GO/PANI, Co-doped TiO_2/PANI, (a_1) PANI, (a_2) butvar alone after 15 days of immersion, and (b) after 30 days of immersion in 3.5% NaCl solution. From Figure 4.23a it can be seen that the semicircle diameter at the Z_{re} axis of the Co-doped TiO_2/GO/PANI is nearly double compared to the value of Co-doped TiO_2/PANI after 15 days of immersion time. These results indicate that the presence of GO in the PANI NCs is more efficient for corrosion control, where the Co-doped TiO_2/GO/PANI NCs has better corrosion protection performance than the Co-doped TiO_2/PANI on carbon steel. These results suggest that the semicircle diameter on the real axis (Z_{re}) increases with the presence of GO and Co-doped TiO_2 NPs. The results in Figure 4.23 prove the efficiency of the Co-doped TiO_2/GO/PANI NCs as an additive for corrosion protection of steel surface. It can be seen in Figure 4.23b that there is only one semicircle in the Nyquist plots of Co-doped TiO_2/GO/PANI and Co-doped TiO_2/PANI during the immersion of 30 days in 3.5% NaCl solution. Whereas, the Nyquist plots of the carbon steel coated with PANI and butvar (inset of Figure 4.23b) indicate two-time constants after 30 days of immersion time. The first semicircle (at higher frequencies) is associated with the formation of porous corrosion products which serve as a protective barrier. The second semicircle is related to the charge transfer resistance process which occurs beneath the surface of the carbon steel coated with PANI (Ladan et al., 2017; Pour-Ali et al., 2015).

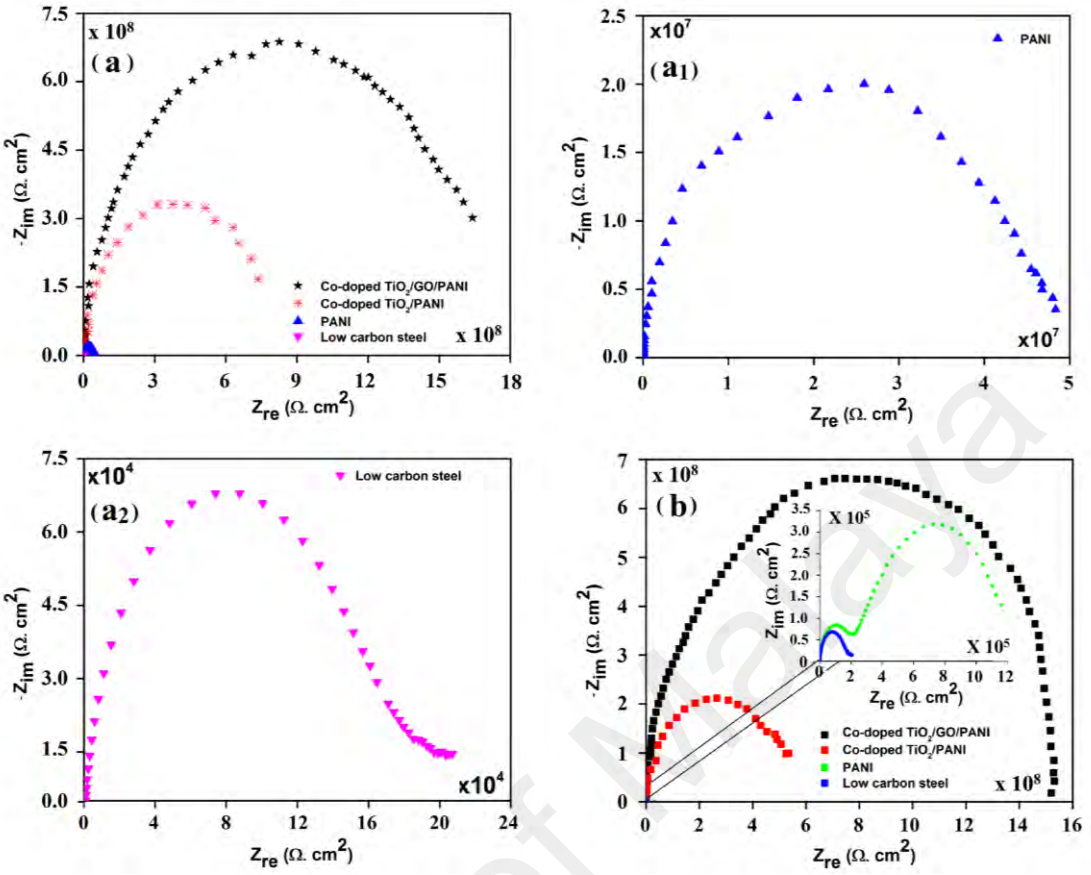

Figure 4.23: Nyquist plot of carbon steel coated with (a) Co-doped TiO_2/GO/PANI and Co-doped TiO_2/PANI, (a_1) PANI, (a_2) low carbon steel (butvar) after 15 days of immersion time and (b) After 30 days of immersion time in 3.5% NaCl solution, respectively

Figure 4.24(a and c) represents the Bode modulus and Bode phase diagrams respectively, of the carbon steel coated with Co-doped TiO_2/GO/PANI NCs at different immersion times. Figure 4.24(b and d) shows the Bode modulus and Bode phase diagrams respectively, for all the materials after 15 days of immersion time in 3.5% NaCl solution. The log |Z| value for the low carbon steel coated with Co-doped TiO_2/PANI NCs is approximately 8.9 for the immersion time of 15 days, but increases to 9.4 for the steel coated with Co-doped TiO_2/GO/PANI NCs incorporated butvar (Figure 4.24b) for the same immersion time. These results indicate better corrosion protection performance of the Co-doped TiO_2/GO/PANI NCs compared to the Co-doped TiO_2/PANI NCs as the exposure time increases. The log |Z| value of the carbon steel coated with Co-doped TiO_2/GO/PANI NCs is higher than the rest of the coatings

after 15 days of immersion time. The results also indicate that the log |Z| value decreases with the increase in immersion time. It can be deduced that the reduction in the log |Z| value is ascribed to the electrolyte penetration into the coated steel specimen. Hence, an increase in the coating capacitance and decrease in the coating resistance are observed. The variations of the log |Z| value in the initial ten days are small. However, as the immersion time increases, the log |Z| decreases from 9.7 (first day) to around 9.2 at the end of the 30 days.

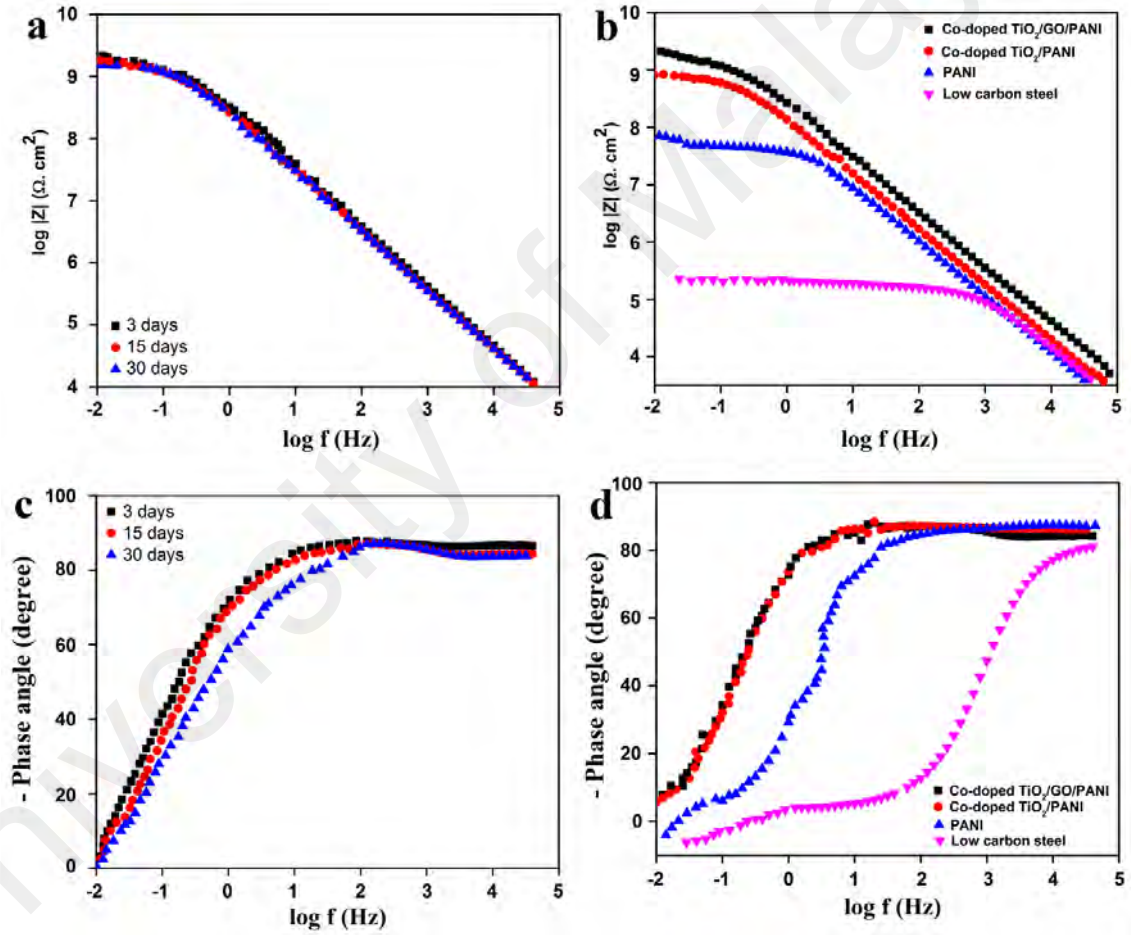

Figure 4.24: (a) Bode modulus and (c) Bode phase diagrams of carbon steel coated with Co-doped TiO_2/GO/PANI NCs at different immersion times. (b) Bode modulus and (d) Bode phase diagrams for all the materials after 15 days of immersion time in 3.5% NaCl solution

Table 4.5: Impedance parameters of the Co-doped TiO_2/GO/PANI NCs containing butvar coated on carbon steel immersed in 3.5 % NaCl solution

Time (days)	R_c ($x10^9$ Ω cm^2)	Q/Y_o ($x10^{-9}$ $Ω^{-1}$ S^n cm^{-2})	n	C_c ($x10^{-9}$ F cm^{-2})
1	8.910	0.3944	0.9667	0.0453
3	6.230	0.5814	0.9566	0.0630
5	6.050	0.5571	0.9131	0.0854
7	5.671	0.5674	0.9245	0.0987
11	4.601	0.5915	0.9565	0.1064
13	2.630	0.6014	0.9571	0.1657
15	2.041	0.6875	0.9526	0.1846
17	1.767	0.8590	0.9484	0.1893
21	1624	0.8901	0.9551	0.1953
23	1.509	0.9041	0.9523	0.2034
25	1.480	0.9147	0.9488	0.3342
27	1.288	0.9476	0.9489	0.4037
29	0.912	0.9681	0.9397	0.4856
30	0.862	0.9891	0.9192	0.5678

The Co-doped TiO_2/GO/PANI/electrolyte impedance parameters were estimated by the simulations with the FRA EXE software and presented in Table 4.5. The EIS results of the coatings were simulated using the $R_1(R_2Q)$ equivalent circuit model, and good correlations between the experimental and simulated data were obtained. The circuit model is composed of a series of the component, which consists of the bulk solution resistance (Rs, or R_1 in the circuit model) and the parallel combination of R_2 and Q. The parallel combination (R_2Q) consists of the constant phase element (CPE, or Q in the circuit model) due to the coating capacitance (C_c) and charge transfer resistance R_{ct} (R_2

in the circuit model) as the coating resistance (R_c). The CPE was used instead of pure capacitance in the simulation process due to the surface inhomogeneity and roughness (Matin et al., 2015). Equation (4.4) gives the CPE impedance (Ladan et al., 2017; Yuan et al., 2015):

$$Z(CPE) = Y_o^{-1}(j\omega)^{-n} \tag{4.4}$$

Where Y_o is the constant phase element, n is the exponent of CPE and ω is the angular frequency. The CPE parameter is dependent on Q and exponent "n". Equation (4.5) gives the conversion of Y_o to C_c (Hao et al., 2013; Jiang et al., 2015a; Jiang et al., 2015b).

$$C_c = Y_o(\omega_m^{"})^{n-1} \tag{4.5}$$

where C_c is the coating capacitance, $\omega_m^{"}$ is the angular frequency at which Z imaginary is maximum.

The coating deterioration can be assessed from the R_c and C_c values on immersion times (Figure 4.25). From Figure 4.25, it can be seen that the R_c indicates the degree of ionic penetration through the coating, which decreases with the increase of immersion time, revealing a higher ionic conductivity and lower protective properties of the coatings due to the electrolyte diffusion (Pour-Ali et al., 2015; Ramezanzadeh et al., 2016). The difference in the C_c values is an alternative approach to recognize the performance of the coating. The increase in the coating capacitance value (C_c) is due to the increase in the electrolyte uptake (Pour-Ali et al., 2016). The effectiveness of the organic coating as an anti-corrosive agent may be attributable to the barrier effects which avert the electrolyte from reaching the steel surface.

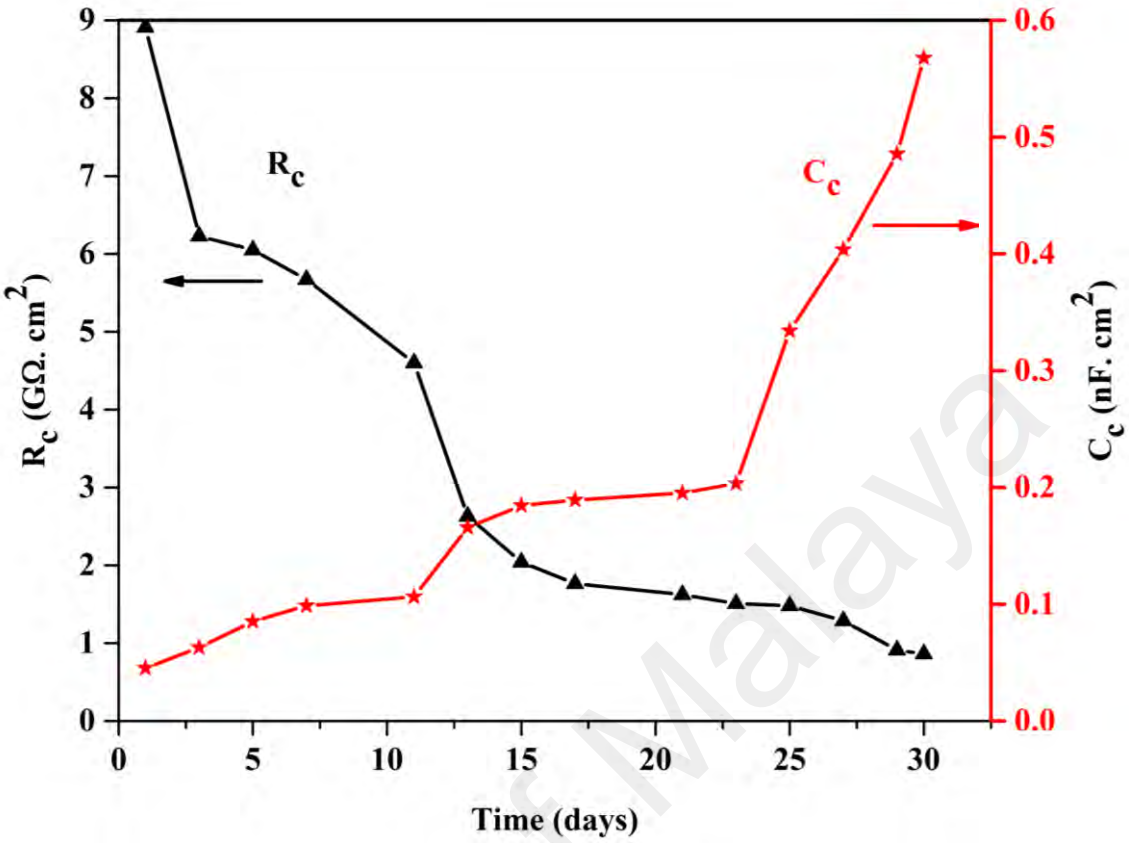

Figure 4.25: The variation of the charge transfer resistance R_c, and the coating capacitance C_c, of the carbon steel, coated with Co-doped TiO_2/GO/PANI NCs on immersion time in 3.5 % NaCl solution

The excellent corrosion protection performance of the Co-doped TiO_2/GO/PANI NCs is further confirmed from the Bode plots shown in Figure 4.24(b). It can be seen that Co-doped TiO_2/GO/PANI NCs has better resistance properties than the rest of the coatings which could be associated with the ionic transport through the coatings. Also, the Bode phase angle values in Figure 4.24d show that the coatings incorporated with Co-doped TiO_2/GO/PANI and Co-doped TiO_2/PANI remain intact while others indicate signs of deterioration (Mahmoudian et al., 2011a). The outstanding corrosion resistance performance of the coatings incorporated with Co-doped TiO_2/GO/PANI NCs could be due to barrier effect which prevents the corrosive agents from reaching the steel surface. It also promotes the passive layer formation and decreases reaction with the corrosive ions (Radhakrishnan et al., 2009). In this case, the excellent corrosion resistance performance is enhanced due to the presence of GO and Co-doped TiO_2. The

incorporation of GO and Co-doped TiO_2 enhanced the barrier properties of PANI NCs against electrolyte diffusion (Sun et al., 2007). The polymerization of PANI was conducted in the presence of GO, and Co-doped TiO_2 dispersed in the reaction medium, it is most likely that the PANI formed around these particles resulting in a core-shell-like structure where the Co-doped TiO_2 is the core, and the PANI forms the shell. This kind of material gives rise to a higher surface area compared to the pure PANI. The major role of PANI in corrosion prevention is its redox nature where it absorbs the ions liberated during the corrosion reaction of low carbon steel in the presence of an electrolyte and oxygen (Mahmoudian et al., 2011). The subsequent doping and release of the dopant ions form a passive layer even upon the initiation of the corrosion process. There is also a possibility of charge trapping process in the Co-doped TiO_2/GO/PANI NC due to the n-type nature of the TiO_2 with a band gap of around 3.13 eV and p-type nature of PANI with a band gap of 2.1 eV (Grgur et al., 2015; Kofstad, 1972). This could form a barrier at the electrolyte/steel interface which could avert the charge transport across the layer.

4.3 Synthesis and characterization of PANI/GO/Zn-doped TiO_2 NCs for corrosion control

4.3.1 Materials characterization

4.3.1.1 XRD of PANI, GO, TiO_2 NPs, Zn-doped TiO_2 NPs, Zn-doped TiO_2/PANI NCs, and Zn-doped TiO_2/GO/PANI NCs

XRD provides useful information about the structure of the samples. Figure 4.25 represents the X-ray diffraction patterns of (a) TiO_2 and (b) Zn-doped TiO_2 calcined at 500 ^oC, respectively. Figure 4.26 (c and d) displays the XRD patterns of PANI/Zn-doped TiO_2, and PANI/GO/Zn-doped TiO_2. It is observed in Figure 4.26 (a & b) that both the TiO_2 and Zn-doped TiO_2 exhibit anatase structure. The spectrum of TiO_2 NPs

shows various diffraction peaks at 2θ of 25.31°, 37.79°, 48.10°, 53.88°, 55.08°, 62.69°, 68.76°, 70.31°, 75.05°, and 82.69° which is indexed to the (101), (004), (200), (105), (211), (204), (116), (220), (215) and (224) tetragonal anatase TiO_2 (COD 96-900-8214) with the lattice constant a = b = 0.3784 nm and c = 0.9515 nm. Similar TiO_2 NPs diffraction patterns were observed in Zn-doped TiO_2 NPs which also correspond to the standard X-ray diffraction peaks of anatase TiO_2 (Shen et al., 2014). By comparing the diffractograms of both TiO_2 NPs and Zn-doped TiO_2 NPs, it can be observed that the addition of Zn into the lattice of TiO_2 decreases the diffraction peak (101) intensity. This decrease in the intensity is likely due to the decrease in crystallinity. Using the Scherrer's formula (Equation 4.6), the crystallite sizes (D) of the TiO_2 NPs and Zn-doped TiO_2 NPs were calculated to be 20 nm and 12.5 nm, respectively (Wattanawikkam & Pecharapa, 2015).

$$D = \frac{K\lambda}{\beta \cos\theta} \tag{4.6}$$

Where D is the crystallite size, K = 0.9 (shape factor), β is the FWHM (full width at half maximum), λ is the X-ray wavelength (0.154 nm), and θ is the major diffraction peak at 2θ = 25.31˚.

It is evident that the shift of the diffraction peaks confirms the metal ion doping into the titania lattice structure. More pattern shifts were observed when the difference in the ionic radii between the host metal and the doped metal ions is high. The ionic radius of Zn^{2+} is 0.74 Å, which is slightly larger compared to Ti^{4+} (0.68 Å), which results in the slight shift of the diffraction peaks due to the Zn doping into the titania lattice.

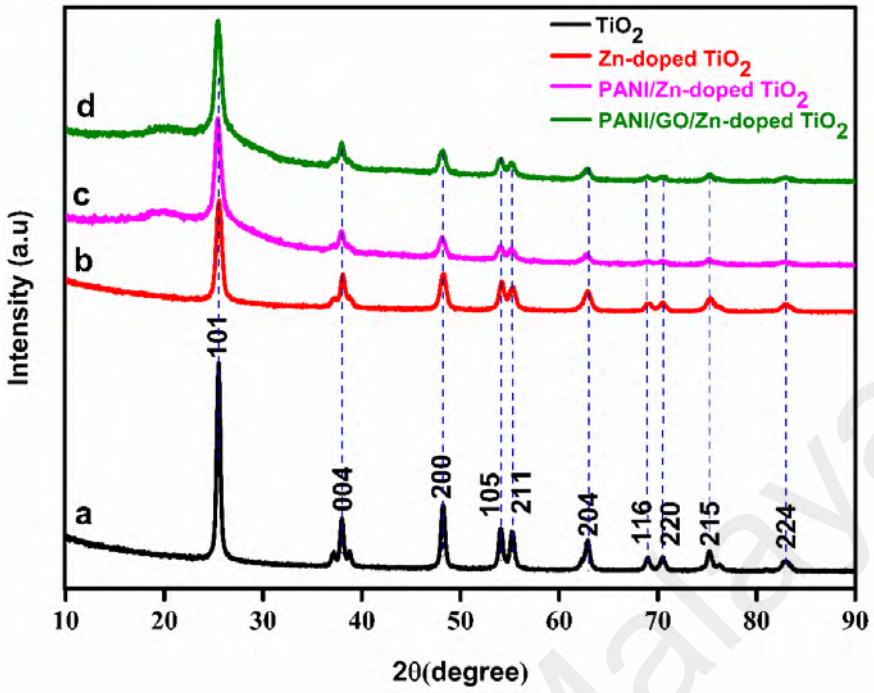

Figure 4.26: XRD spectra of (a) TiO_2 NPs, (b) Zn-doped TiO_2 NPs, (c) PANI/Zn-doped TiO_2 NCs, and (d) PANI/GO/Zn-doped TiO_2 NCs

The XRD patterns of the PANI/Zn-doped TiO_2 and PANI/GO/Zn-doped TiO_2 NCs both indicate characteristic peaks of PANI and TiO_2. It is believed that the broad diffraction peak of PANI in Figure 4.26c is too weak to be observed. This suggests that the addition of Zn-doped TiO_2 NPs hampers the crystallinity of PANI molecular chain. This is because of the absorption of PANI onto the Zn-doped TiO_2 NPs surface. The molecular chain of the absorbed PANI is tethered onto the titania nanoparticles and hence decreases the crystallinity of the PANI (Pawar et al., 2010). The same phenomenon was observed in the XRD spectrum of PANI/GO/Zn-doped TiO_2 NCs (Figure 4.26d). The crystallite sizes of both PANI/Zn-doped TiO_2 and PANI/GO/Zn-doped TiO_2 NCs were calculated from the (101) peak. The crystallite size is around 39.8 nm, and 14.5 nm for the PANI/Zn-doped TiO_2 and PANI/GO/Zn-doped TiO_2 NCs, respectively, from the Scherrer' equation.

Figure 4.27 indicates the XRD patterns of pure PANI and GO. The XRD pattern of pure PANI shows broad peaks at 2θ = 20.3 and 25.41˚, which is attributable to the

periodicity of the polymer chain indicative of amorphous nature of PANI (Mi et al., 2008; Pawar et al., 2009). The XRD patterns of GO shown in Figure 4.27 indicates a strong diffraction peak at 2θ = 9.6˚ which signifies GO characteristic (Shabani Shayeh et al., 2015). The small diffraction peak seen at 2θ = 42.4˚ is associated with (100) plane of graphite and which indicates the presence of some traces of graphite phases in the structure of GO (Shabani Shayeh et al., 2015).

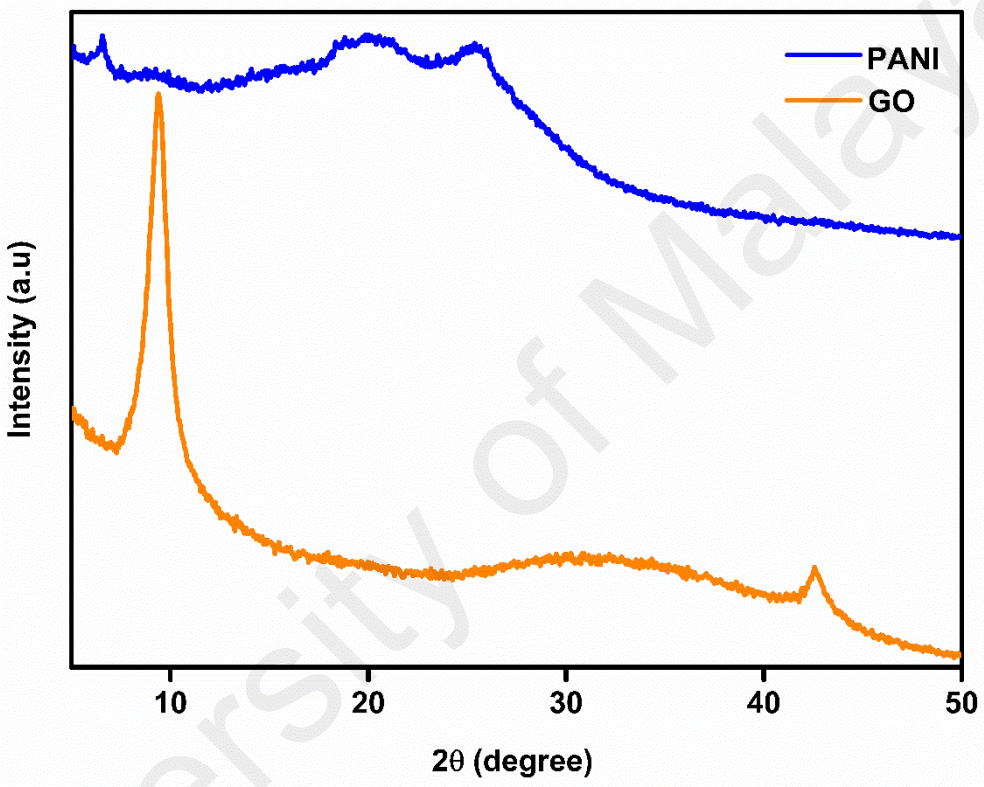

Figure 4.27: XRD spectra of pure polyaniline (PANI) and graphene oxide (GO)

4.3.1.2 FTIR of TiO_2 NPs, Zn-doped TiO_2 NPs, PANI, PANI/Zn-doped TiO_2 NCs, and PANI/GO/Zn-doped TiO_2 NCs

Figure 4.28 presents the FT-IR spectra of TiO_2 NPs and Zn-doped TiO_2 NPs. The bands were seen at 3139 cm^{-1} and 3291 cm^{-1} in TiO_2 NPs and Zn-doped TiO_2 NPs respectively, are ascribed to the stretching vibration of hydroxyl (OH) groups (Mahmoudian et al., 2011b; Zhang & Gao, 2002). The bands at 1633 cm^{-1} for TiO_2 and 1631 cm^{-1} for Zn-doped TiO_2 are likely due to the bending vibration of the coordinated

H_2O molecule and additionally from the Ti-OH. The bands at 426 cm^{-1}, 769 cm^{-1}, and 745 cm^{-1} in both TiO_2 and Zn-doped TiO_2 are attributed to the Ti-O bond vibration and O-O mode of stretching for TiOOH on the TiO_2 NPs surface, respectively (Nakamura et al., 2003). The bond energy of Zn-O (283 kJ. mol^{-1}) is significantly lower than that of Ti-O (662 kJ. mol^{-1}) (Mahmoudian et al., 2011b). So, doping of Zn^{2+} in TiO_2 NPs should not lead to a significant shift of the wavenumber for the vibration of Ti-O lattice.

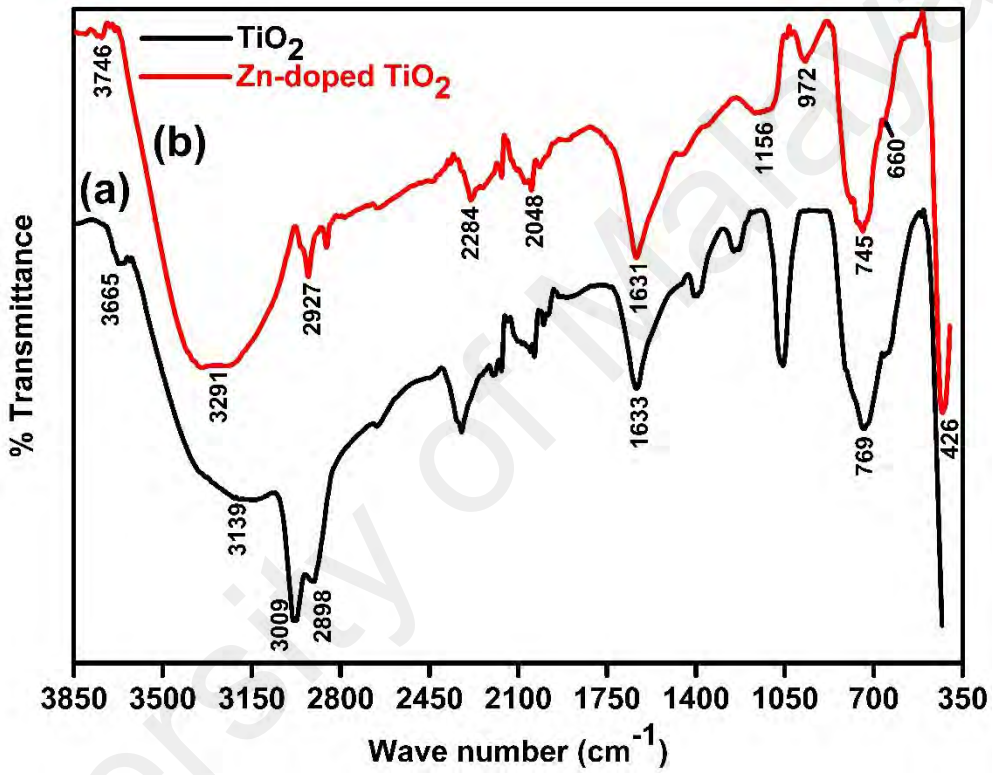

Figure 4.28: FTIR of (a) TiO_2 NPs and Zn-doped TiO_2 NPs calcined at 500 °C for 5 h

The FTIR spectra also show the interaction between the polymer (PANI) and the TiO_2 NPs. The FTIR spectra of PANI, PANI/Zn-doped TiO_2 NCs, and PANI/GO/Zn-doped TiO_2 NCs are displayed in Figure 4.29 (a-c), respectively. Figure 429a shows the characteristic peaks of PANI. The band observed at 3228 cm^{-1} is assigned to the stretching vibration of N−H, and the peak at 3045 cm^{-1} is assigned to the C−H vibration of the aromatic ring. The bands at 1571 cm^{-1} and 1492 cm^{-1} are due to the stretching vibrations of the quinonoid and benzenoid structures, respectively (Guo et al., 2014). Also, the absorption peak at around 1145 cm^{-1} is attributed to the quinonoid unit of

doped PANI. Additionally, the peak at 1299 cm^{-1} is due to the benzenoid unit stretching vibration of C−N. The absorption peak observed at 1083 cm^{-1} is due to the C−H bending vibration. The band at around 807 cm^{-1} is associated to the C−H and C−C of the benzenoid unit (Majumdar et al., 2015; Ranka et al., 2016; Xie et al., 2011). Absorption peaks observed within 489−801 cm^{-1} in Figure 4.29 (b and c) are linked to the stretching vibrations of Ti−O−Ti, which is the characteristic absorption frequencies in anatase phase of TiO_2 (Kim et al., 2007; Liu et al., 2013). Furthermore, all characteristic absorption peaks of PANI are also present in Figure 4.29 (b and c) indicating the presence of PANI in PANI/Zn-doped TiO_2 NCs and PANI/GO/Zn-doped TiO_2 NCs, respectively. The new absorption peak at around 1078 cm^{-1} is likely due to the Ti-O-C stretching vibration (Li et al., 2013b), which could result from the interaction between the PANI, Zn-doped TiO_2, GO. Also, the peak at 3747 cm^{-1} that is assigned to stretching mode of N–H, shifts to higher wavenumber in PANI/GO/Zn-doped TiO_2 NCs and is enhanced in PANI/Zn-doped TiO_2 NCs, because of the contribution from O–H stretching mode of GO molecules (Su et al., 2012a).

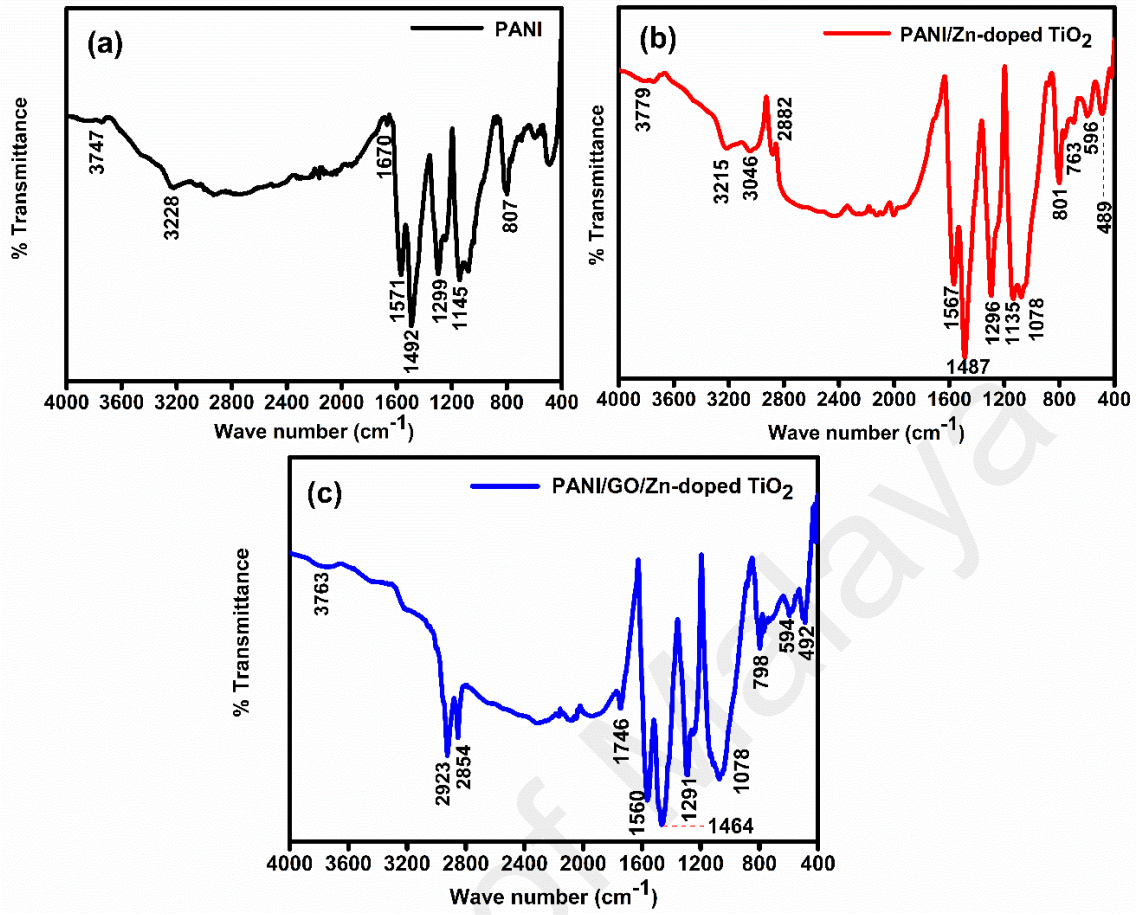

Figure 4.29: FTIR of (a) PANI, (b) PANI/Zn-doped TiO_2 NCs and (c) PANI/GO/Zn-doped TiO_2 NCs synthesized in the presence of ferric chloride ($FeCl_3$)

4.3.1.3 EDX analyses and FESEM micrographs of TiO_2 NPs and Zn-doped TiO_2 NPs calcined at 500 °C for 5 h.

The Field emission scanning electron micrographs of TiO_2 NPs and Zn-doped TiO_2 NPs are presented in Figure 4.30. The elemental analysis was also performed by energy dispersive X-ray studies (EDX) as presented in Figure 4.30 (c and d) for both TiO_2 NPs and Zn-doped TiO_2 NPs. The EDX results show that the doped samples contain 2.66% Zn and it can be confirmed that the Zn^{2+} ions are incorporated into the TiO_2 lattice. Figure 4.30 (a and b) displays the FESEM micrographs of TiO_2 and Zn-doped TiO_2. The particles are uniform and have spherical like morphology, which consists of spheres of small spherical crystals of TiO_2 agglomerated together. It can be observed that the particle sizes of TiO_2 NPs and Zn-doped TiO_2 NPs are about 19.8 ± 0.23 and 12.1 ±

0.18, respectively. This shows that the decrease in the particle size was observed due to the Zn doping. When Zn^{2+} ions are doped into the TiO_2 lattice in grain boundary regions or on the particles surface, they inhibit the growth of the TiO_2 crystal.

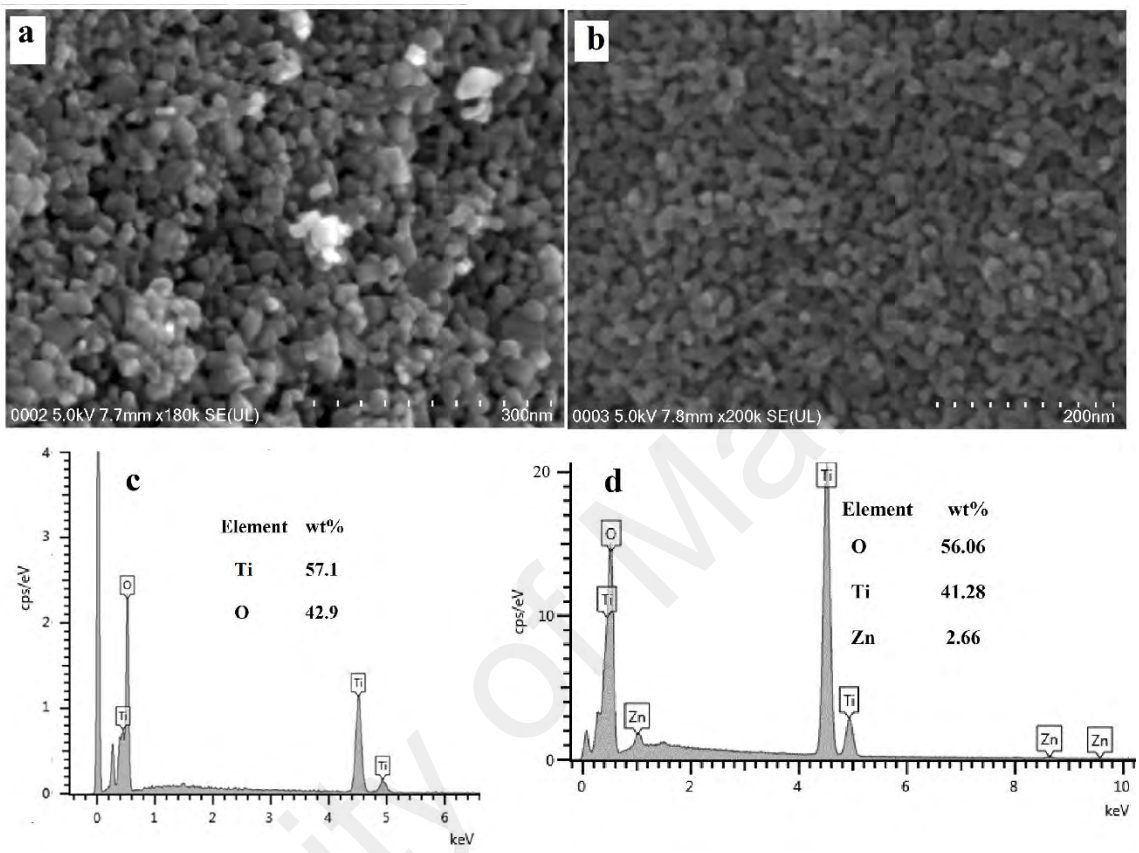

Figure 4.30: FESEM images of (a) TiO2 NPs, and (b) Zn-doped TiO2 NPs calcined at 500 °C for 5 h and their EDX spectra (c and d), respectively

4.3.1.4 EDX analyses and FESEM micrographs of PANI/Zn-doped TiO_2 NCs and PANI/GO/Zn-doped TiO_2 NCs synthesized in the presence of $FeCl_3$.

Figure 4.31 shows the FESEM micrographs and EDX spectra of PANI/Zn-doped TiO_2 NCs and PANI/GO/Zn-doped TiO_2 NCs. It is observed that the PANI/Zn-doped TiO_2 NCs indicates rod-like morphology with small Zn-doped TiO_2 NPs distributed on the surface of PANI (Figure 4.31a). Figure 4.31b shows the morphology of the nanocomposites containing GO (PANI/GO/Zn-doped TiO_2 NCs). From the FESEM image in Figure 4.31b, the rod-like PANI, flake-like graphene, and small Zn-doped TiO_2 were observed. EDX analyses were used to study the elemental composition of the

synthesized nanocomposites. The EDX spectra were shown in Figure 4.31(c and d). It is seen that the wt% of C and O is higher in PANI/GO/Zn-doped TiO_2 NCs as compared with that in PANI/Zn-doped TiO_2 NCs, which confirms the presence of GO in PANI/Zn-doped TiO_2 NCs.

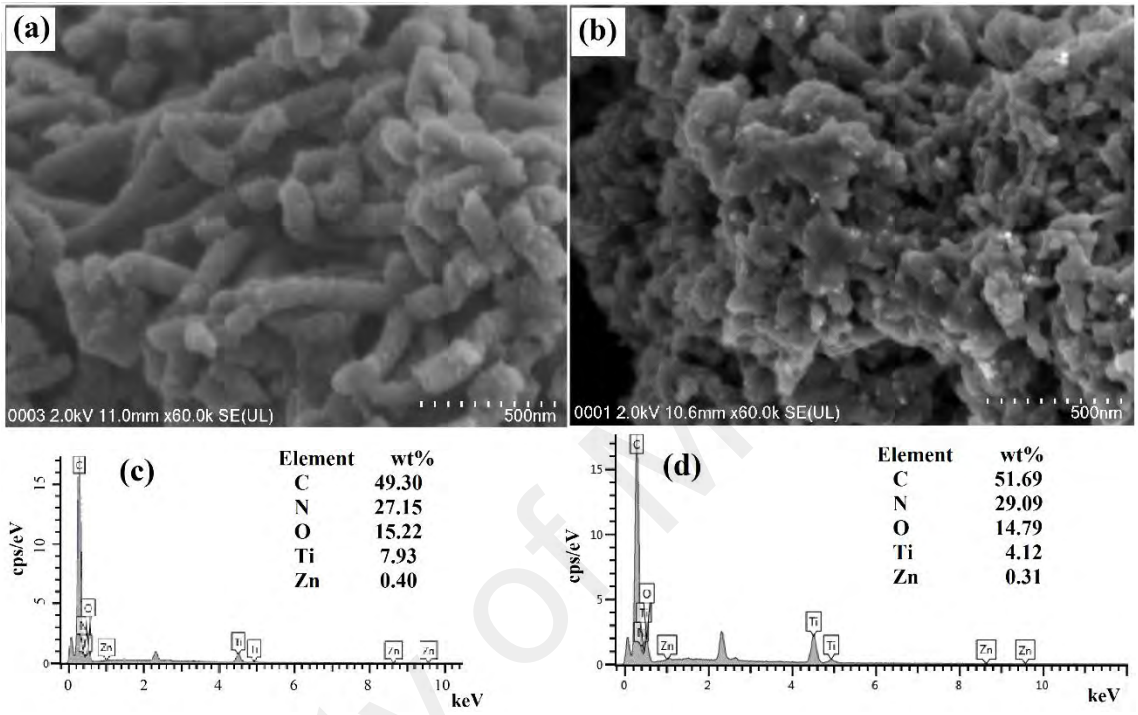

Figure 4.31: FESEM images of (a) PANI/Zn-doped TiO_2 NCs and (b) PANI/GO/Zn-doped TiO_2 NCs synthesized in the presence of $FeCl_3$ and their EDX spectra (c and d), respectively

4.3.1.5 TEM images TiO_2 NPs and Zn-doped TiO_2 NPs calcined at 500 °C for 5 h.

To predict the shape and size of TiO_2 and 3% Zn-doped TiO_2 NPs, the calcined sample at 500 °C was dispersed in a solvent (ethanol) under ultrasonicated for 30 min. Figure 4.32 displays the TEM images of TiO_2 NPs and Zn-doped TiO_2 NPs, respectively. It can be observed from Figure 4.32 (a and c) that the particles assume random shape, usually spherical and cubic in nature. This is likely because of the increase in the temperature and reaction time which results in the random shape of the nanoparticles (Mahmoudian et al., 2011b). The average size of the TiO_2 NPs and Zn-doped TiO_2 NPs calculated from the TEM micrographs were 19.94 ± 0.96 nm and 12.19

± 1.17 nm, respectively, which is by the results obtained from the XRD analysis. Therefore, this indicates that low percentage of Zn doping decreases the size of the TiO_2 NPs. The high-resolution TEM (HR-TEM) images in Figure 4.32 (b and d) of TiO_2 NPs and Zn-doped TiO_2 NPs, respectively, reveals the same *d* spacing of 0.35 for both TiO_2 and Zn-doped TiO_2 NPs.

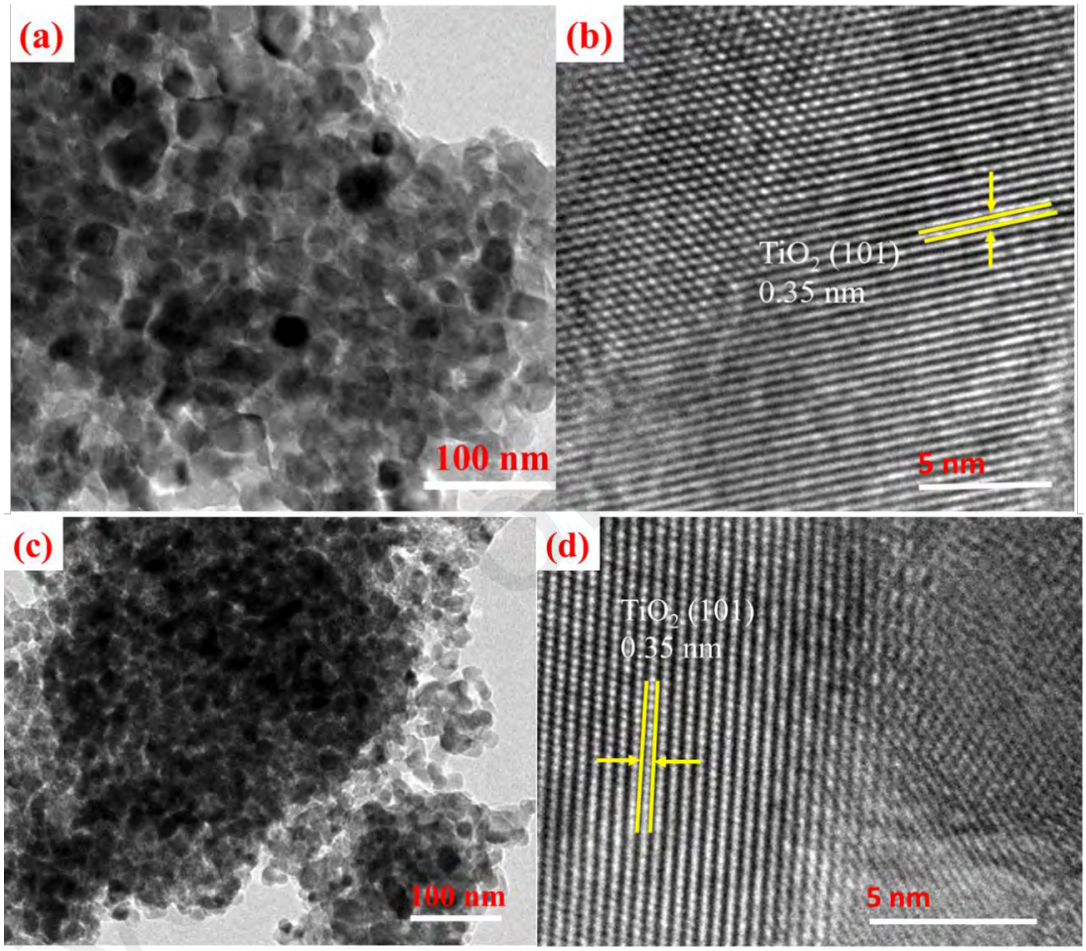

Figure 4.32: TEM images of (a and b) TiO_2 NPs, and (c and d) Zn-doped TiO_2 NPs, calcined at 500 **°C**

4.3.1.6 TEM images PANI/Zn-doped TiO_2 NCs, and PANI/GO/Zn-doped TiO_2 NCs.

Figure 4.33 displays the TEM images of PANI/Zn-doped TiO_2 NCs and PANI/GO/Zn-doped TiO_2 NCs. As can be observed from the TEM micrographs in Figure 4.33, the Zn-doped TiO_2 NPs are randomly distributed in the PANI matrix and tend to agglomerate along the PANI chains.

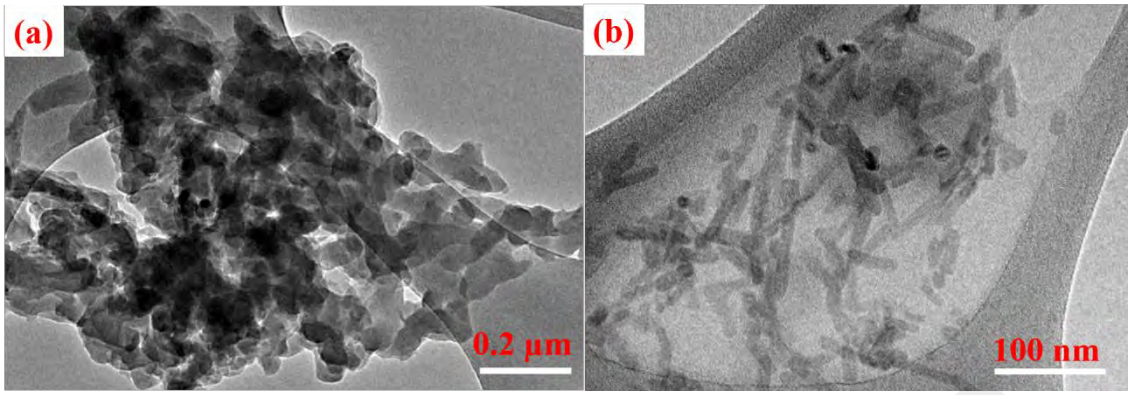

Figure 4.33: TEM images of (a) PANI/Zn-doped TiO_2 NCs and (b) PANI/GO/Zn-doped TiO_2 NCs

4.3.2 Electrochemical corrosion measurements

4.3.2.1 Open circuit potentials (OCP)

Figure 4.34 displays the OCP plots with the exposure time for the steel coated with (1) butvar-PANI/GO/Zn-doped TiO_2 NCs, (2) butvar-PANI/Zn-doped TiO_2 NCs, (3) butvar-PANI, and (4) butvar alone. The steel coated with the PANI/GO/Zn-doped TiO_2 NCs has higher potential compared to the steel coated with PANI/Zn-doped TiO_2 NCs, PANI and butvar, respectively. As shown in Figure 4.34, the OCP value of the PANI/GO/Zn-doped TiO_2 coated on steel decreases from 0.095 V to -0.03 V after nine (9) days of exposure in a solution of 3.5% NaCl which could be due to the electrolyte penetration to the steel surface.

The decreasing trend of the OCP values from 0.095 V to -0.115 V of the coatings incorporated with PANI/GO/Zn-doped TiO_2 NCs from the first day to 30 days of immersion time confirms that the breakdown of coatings was slow and gradual. Therefore the OCP values of PANI/GO/Zn-doped TiO_2 NCs demonstrate only small changes between 1 to 30 days of exposure time which confirms the high performance of this coating for corrosion protection. The passivity of the coating prepared with PANI significantly decreased just after 10 days of immersion in a solution of 3.5% NaCl. Furthermore, the OCP values of PANI/GO/Zn-doped TiO_2 NCs, PANI/Zn-doped TiO_2

NCs, PANI and steel coated with butvar alone after 30 days of immersion were -0.115 V, -0.198 V, -0.578 V and -0.875 V respectively. This confirms the excellent performance of the coatings prepared with PANI/GO/Zn-doped TiO_2 NCs against corrosion, compared to the coatings prepared with PANI/Zn-doped TiO_2 and PANI, respectively.

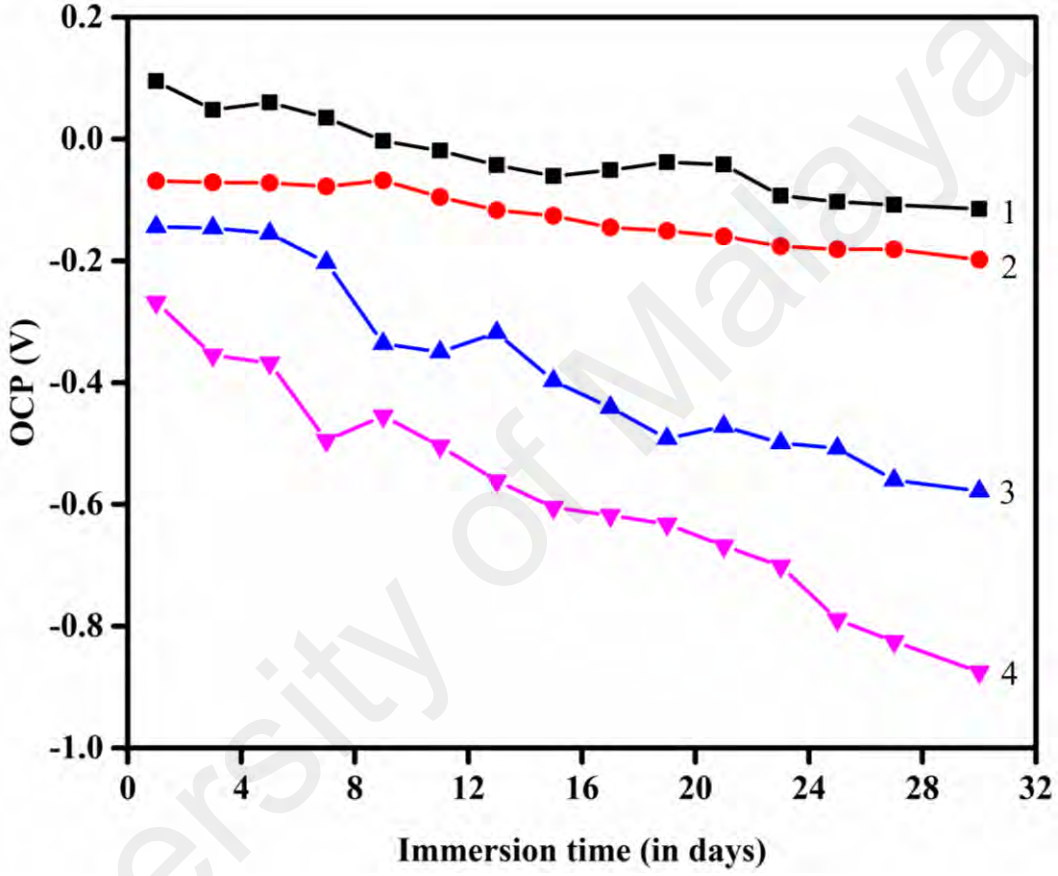

Figure 4.34: Open circuit potential (OCP) values with the immersion time (in days) in a 3.5% NaCl solution for steel coated with (1) Butvar-PANI/GO/Zn-doped TiO_2 NCs, (2) ButvarPANI/Zn-doped TiO_2 NCs, (3) Butvar-PANI, and (4) Butvar

4.3.2.2 Potentiodynamic polarization analysis

Tafel study is an excellent tool to estimate the instantaneous corrosion rate of steel (Neupane et al., 2015). Figure 4.35 displays the Tafel curves of steel coated with butvar, PANI, PANI/Zn-doped TiO_2 NCs and PANI/GO/Zn-doped TiO_2 NCs after 30 days of exposure to a solution of 3.5% NaCl. The corrosion potential (E_{corr}) of the steel coated with PANI/Zn-doped TiO_2 NCs and PANI/GO/Zn-doped TiO_2 NCs shifts to

more positive regions compared to that of butvar and PANI. In addition, the corrosion current decreases from 2.19 x 10^{-6} A cm^{-2} (coated steel with butvar) to 3.30 × 10^{-12} A cm^{-2} (coated steel with PANI/Zn-doped TiO_2 NCs) and 4.32 × 10^{-14} A cm^{-2} (coated steel with PANI/GO/Zn-doped TiO_2 NCs). The Tafel curve analysis indicates that the rate of corrosion of steel coated with PANI/GO/Zn-doped TiO_2 NCs is much lower compared to the coatings prepared with PANI/Zn-doped TiO_2 NCs and PANI, respectively. It is confirmed from the Tafel results that the presence of Zn-doped TiO_2 NPs and GO in the pigments could enhance the corrosion resistance of the steel surface. The electrochemical parameters obtained from the Tafel plots such as the corrosion potential (E_{corr}), corrosion current density (i_{corr}), polarization resistance (R_p) and corrosion rate (CR) are presented in Table 4.6

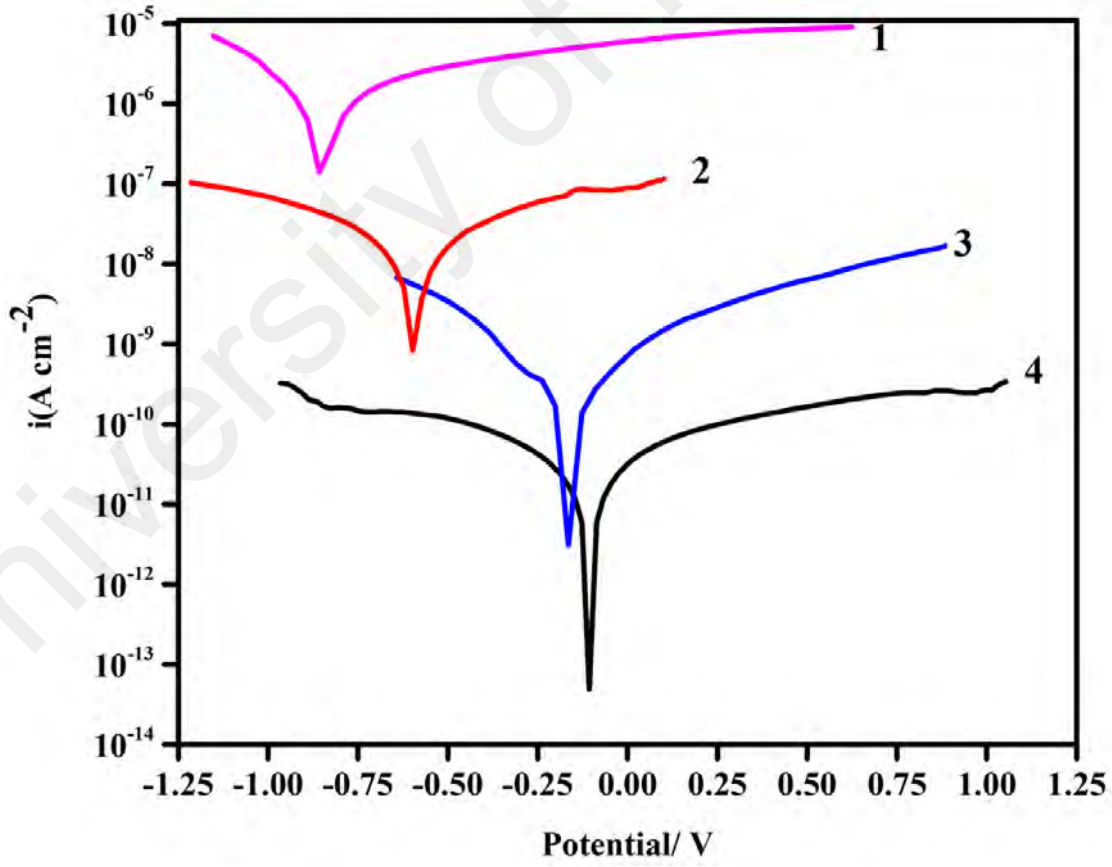

Figure 4.35: Polarization plots of steel coated with (1) butvar, (2) pure PANI, (3) PANI/Zn-doped TiO_2 NCs, and (4) PANI/GO/Zn-doped TiO_2 NCs after 30 days of exposure in 3.5% NaCl solution

Table 4.6: i_{corr}, β_c, β_a, R_p, E_{corr}, and corrosion rate (CR) values of the steel coated with butvar, butvar-PANI, butvar- PANI/Zn-doped TiO_2 NCs, and butvar- PANI/GO/Zn-doped TiO_2 NCs after 30 days of exposure time in 3.5% NaCl solution

Mild steel	i_{corr} (Acm^{-2})	β_c (V/dec)	β_a (V/dec)	R_p ($M\Omega\ cm^2$)	E_{corr} (V)	CR (mpy)
1. coated with butvar	2.19×10^{-6}	0.179	0.163	0.0018	-0.875	2.53×10^{-2}
2. coated with butvar-PANI	2.61×10^{-9}	0.092	0.140	0.6853	-0.577	3.07×10^{-5}
3. coated with butvar-PANI/Zn-doped TiO_2 NCs	3.30×10^{-12}	0.045	0.049	91.99	-0.198	3.89×10^{-8}
4. coated with butvar-PANI/GO/Zn-doped TiO_2/ NCs	4.32×10^{-14}	0.01	0.01	294.3	-0.113	5.09×10^{-10}

4.3.2.3 Electrochemical impedance spectroscopy (EIS) analysis

EIS is a great tool to study the electrochemical deterioration process of steels and their coated substrates. The Bode and Nyquist plots are the two great diagrams in EIS that can be employed to study the corrosion behaviors of coated materials on the steel substrates. The EIS analyses were performed between the frequencies of 100 kHz to 0.01 Hz, with an AC perturbation of 5 mV. Figure 4.36 displays the Nyquist plots of the coated steel after (a) 3 days of exposure, (b) after 15 days of exposure, (c) after 30 days of exposure, and (d) steel coated with PANI/GO/Zn-doped TiO_2 NCs after various days of exposure in 3.5% NaCl solution. From Figure 4.36a, it is observed that the semicircle diameter of the PANI/GO/Zn-doped TiO_2 is higher compared to the semicircle of PANI/Zn-doped TiO_2 after the same immersion time. This indicates that the presence of GO in the nanocomposites of PANI improves its corrosion resistance properties of the coated steel. These results suggest that the semicircle diameter on the real axis (Z_{re}) increases with the presence of GO and Zn-doped TiO_2 NPs. The results in Figure 4.36 prove the efficiency of the PANI/GO/Zn-doped TiO_2 NCs as a pigment for the corrosion protection of steel. The Nyquist plots of the steel coated with butvar (inset of Figure 4.36 (a, b and c) indicate two-time constants for the whole immersion time. The first semicircle (at higher frequencies) is associated with the formation of porous corrosion products which serve as a protective barrier. Whereas the second semicircle is associated with the charge transfer process which occurs underneath the surface of the steel coated with butvar and PANI (Zhu et al., 2017).

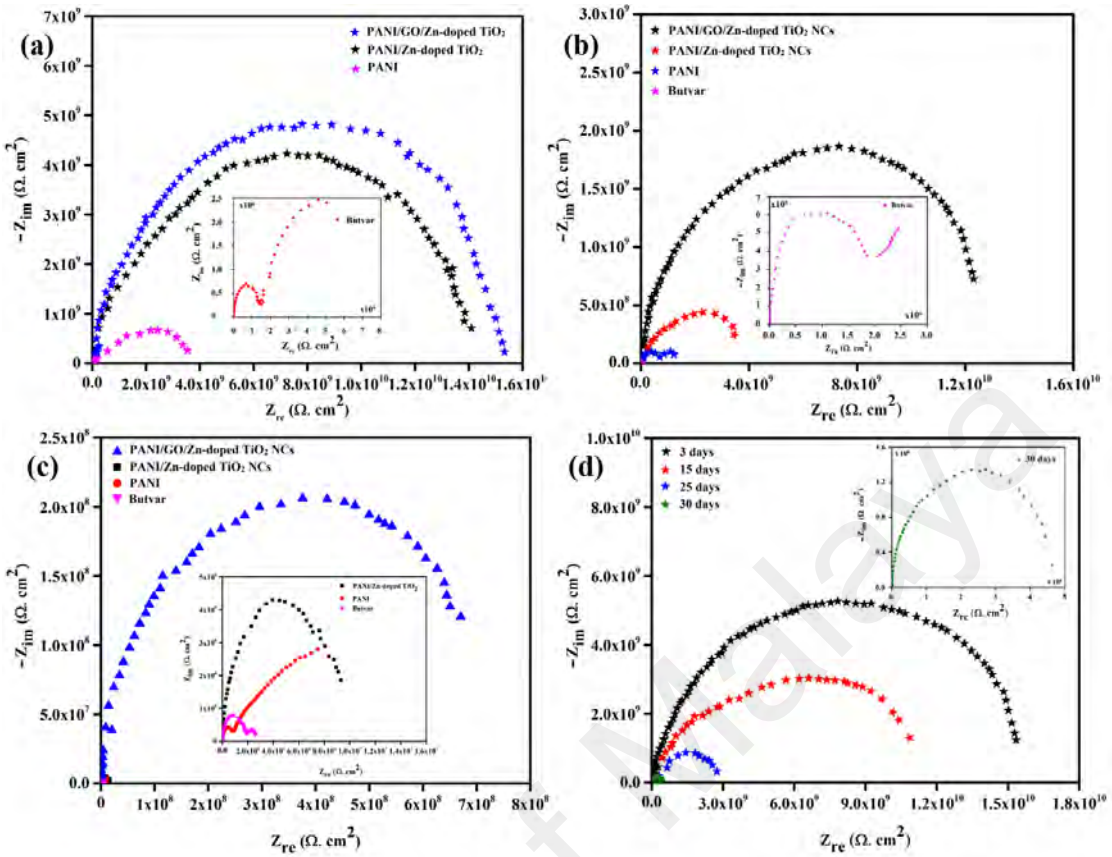

Figure 4.36: Nyquist plots of all samples immersed in 3.5% NaCl solution for the period of (a) 3 days, (b) 15 days, (c) 30 days, and (d) Nyquist plots of PAN/GO/Zn-doped TiO_2 NCs for different immersion period

Figure 4.37 illustrates the Bode magnitude and Bode phase diagrams, for all the materials after 3 days and 15 days of immersion time in 3.5% NaCl solution, respectively. It can be observed from Figure 4.37 (a and b) that the values of log |Z| for PANI/GO/Zn-doped TiO_2 NCs after 3 days and 15 days of exposure are 10.3 and 9.25, respectively. Whereas the log |Z| values for the steel coated with PANI/Zn-doped TiO_2 NCs after 3 days and 15 days of exposure are 9.43 and 8.50, respectively. The log |Z| value for the steel coated with PANI/Zn-doped TiO_2 NCs is nearly 7.15 for the immersion time of 30 days. However, it increases to 9.01 for the steel coated with PANI/GO/Zn-doped TiO_2 NCs (Figure 4.38a) for the same exposure time. These results show that steel coated with PANI/GO/Zn-doped TiO_2 NCs exhibits excellent corrosion protection properties as compared to the rest of the coatings prepared in this research for

the same exposure time. It can be observed from the EIS results that the log |Z| value decreases with the increase in exposure time. So, reduction in the log |Z| value is associated with the penetration of the electrolyte into the surface of the coated steel. Therefore, an increase in the coating capacitance and decrease in the resistance of coatings were observed.

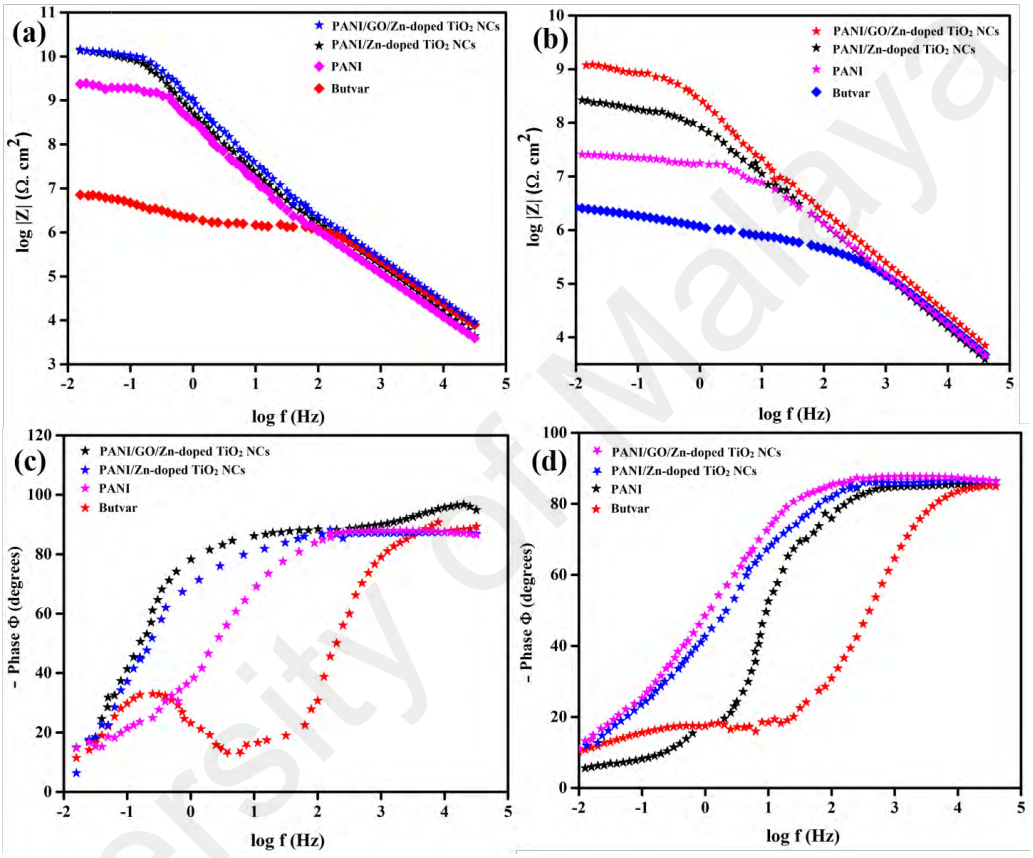

Figure 4.37: Bode magnitude of (a) 3 days, (b) 15 days, and Bode phase of (c) 3 days and (d) 15 days of exposure to 3.5% NaCl solution, respectively

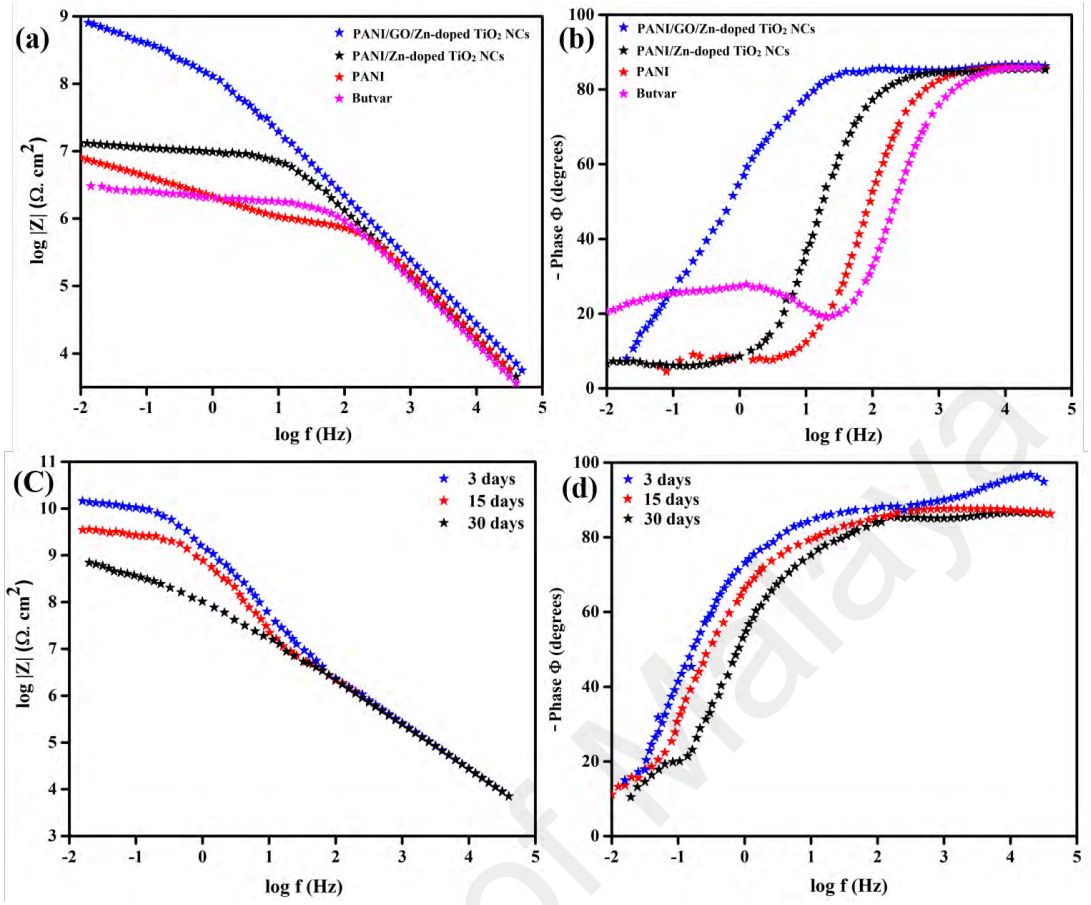

Figure 4.38: (a and b) Bode magnitude and Bode phase after 30 days of exposure in 3.5% NaCl solution and (c and d) Bode magnitude and Bode phase of PANI/GO/Zn-doped TiO_2 NCs coatings for various exposure time

The PANI /GO/Zn-doped TiO_2-electrolyte impedance parameters were obtained by the simulations using the FRA EXE software (see Table 4.7). The EIS results of the coatings were simulated using the $R_1(R_2Q)$ equivalent circuit model, and excellent correlations with the experimental and data were obtained. The circuit model comprises series of components, which consists of the bulk solution resistance (Rs, or R_1 in the circuit model) and the parallel combination of R_2 and Q. The parallel combination (R_2Q) consists of the constant phase element (CPE, or Q in the circuit model) due to the coating capacitance (C_c) and charge transfer resistance R_{ct} (R_2 in the circuit model) as the resistance of coatings. The CPE was used instead of pure capacitance in the simulation process due to the surface inhomogeneity and roughness (Amand et al.,

2013; Lu et al., 2017). The CPE impedance is given by equation 4.7 (Córdoba-Torres et al., 2015; Yan et al., 2013).

$$Z(CPE) = \mathrm{Y}_o^{-1}(j\omega)^{-n} \tag{4.7}$$

Where Y_o is the constant phase element, n is the exponent of CPE and ω is the angular frequency. The CPE parameter is dependent on Q and exponent "n". The conversion of Y_o to C_c is given by equation 4.8 (Hao et al., 2013; Yuan et al., 2016a).

$$C_c = \mathrm{Y}_o(\omega_m^{"})^{n-1} \tag{4.8}$$

where C_c is the coating capacitance, ω_m" is the angular frequency where the imaginary impedance reaches the maximum.

The weakness of the coatings can be evaluated from the values of R_c and C_c on exposure time as depicted in Figure 4.39. The R_c value shows the degree of electrolyte penetration through the coating, which decreases with the increase of exposure time, revealing a higher ionic conductivity and lower protective properties of the coatings due to the electrolyte diffusion (Pour-Ali et al., 2015; Pour-Ali et al., 2016). Also, the C_c values variation is an alternative method to identify the performance of the coating. The increase in the coating capacitance values (C_c) is proportional to the electrolyte uptake (Mahmoudian et al., 2011a). The effectiveness of the organic coating as an anti-corrosive agent may be due to the barrier effects which prevent the electrolyte from reaching the steel surface.

Table 4.7: Electrochemical impedance parameters of the PANI/GO/Zn-doped TiO_2 NCs coated on steel exposed in a solution of 3.5% NaCl

Time (in days)	R_c ($x10^9$ Ω cm^2)	Q/Y_o ($x10^{-9}$ $Ω^{-1}$ S^n cm^{-2})	n	C_c ($x10^{-9}$ F cm^{-2})	χ^2 value
1	3.6760	0.1199	0.9679	0.1272	0.0945
3	3.8931	0.1674	0.9630	0.1746	0.0116
5	3.3944	0.1687	0.9598	0.1758	0.0105
7	2.9571	0.1699	0.9506	0.2001	0.0137
11	2.6581	0.1722	0.9553	0.1851	0.0498
13	2.2592	0.1841	0.9413	0.2024	0.0108
15	2.1973	0.1991	0.9376	0.2202	0.0073
17	2.1647	0.2453	0.9261	0.3050	0.0937
21	1.9824	0.3360	0.9198	0.4021	0.0299
23	1.2592	0.3706	0.9108	0.4368	0.0122
25	0.7945	0.4013	0.9053	0.5187	0.0013
27	0.4034	0.5218	0.8942	0.7046	0.0498
30	0.0591	0.6718	0.8758	0.8996	0.0113

The exceptional corrosion protection performance of the PANI/GO/Zn-doped TiO_2 NCs is further established from the Bode plots shown in Figures 4.37 and 4.38. It can be seen that PANI/GO/Zn-doped TiO_2 NCs possesses better resistance properties than the rest of the coatings which could be linked to the ionic transport through the coatings. Also, the Bode phase angle values in both Figures 4.37 and 4.38 indicate that the coatings containing PANI/GO/Zn-doped TiO_2 and PANI/Zn-doped TiO_2 remain undamaged while others show signs of deterioration (Madhan et al., 2013). The outstanding corrosion resistance properties of the coatings incorporated with

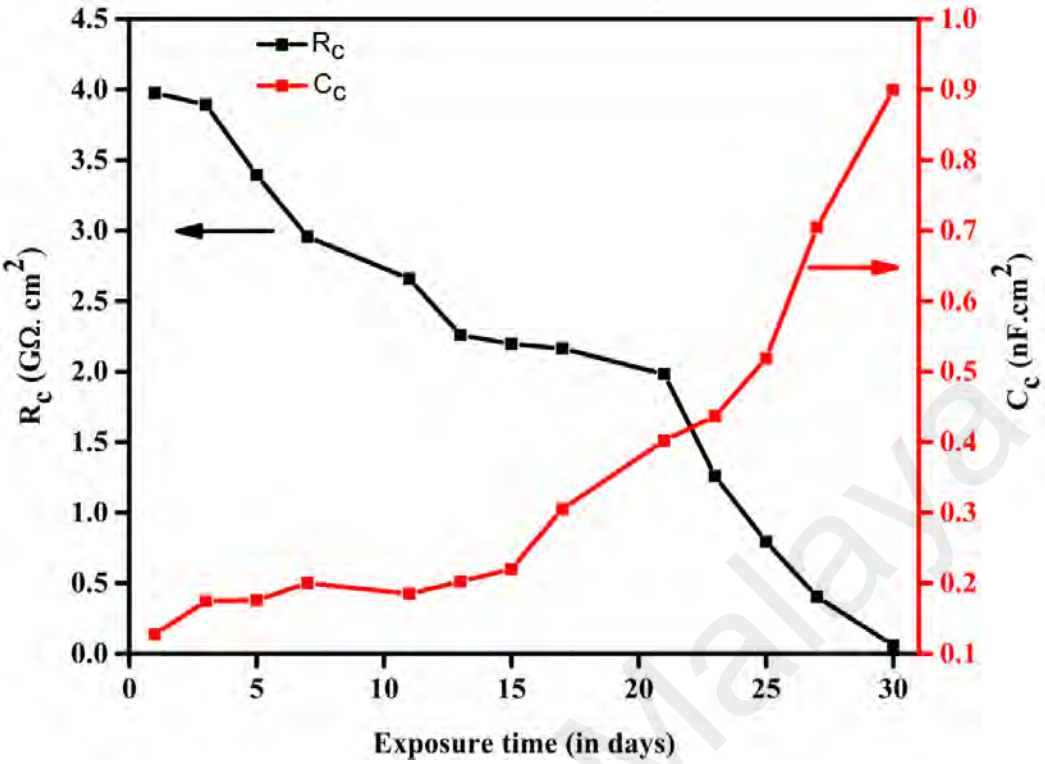

Figure 4.39: The difference in coating resistance R_c and the coating capacitance C_c, of the steel, coated with PANI/GO/Zn-doped TiO_2 NCs on the immersion time in a solution of 3.5% NaCl

PANI/GO/Zn-doped TiO_2 NCs could be due to barrier effect which hinders the corrosive agents from reaching the steel surface. It also promotes the passive layer formation and decreases reaction with the corrosive ions (Akhtari Zavareh et al., 2016). With the presence of GO and Zn-doped TiO_2 NPs in the coating, the electrical resistance of the coating is increased, consequently act as a barrier and decreases electrolyte infiltration through the coating (Batmanghelich & Ghorbani, 2013). The improvement of the barrier effect of PANI NCs against electrolyte diffusion is likely due to the presence of GO and Zn-doped TiO_2 in the nanocomposites (He et al., 2015). The polymerization of PANI was carried out in the presence of GO, and Zn-doped TiO_2 dispersed in the reaction medium by ultra-sonication, it is most likely that the PANI formed around these particles resulting in a core-shell-like structure where the Zn-doped TiO_2 is the core, and the PANI forms the shell. This type of material provides a higher surface area compared to the pure PANI. The major role of PANI in corrosion prevention is its redox nature where it absorbs the ions liberated during the corrosion

reaction of steel (Ladan et al., 2017). From the start of the corrosion reaction, a passive oxide layer on the steel surface is formed because of the doping and the release of the dopant ions. There is also a possibility of charge trapping process in the PANI/GO/Zn-doped TiO_2 NCs due to the n-type nature of the TiO_2 with a band gap of around 3.13 eV and p-type nature of PANI with a band gap of 2.1 eV (Grgur et al., 2015; Qiu et al., 2017). This could speed up the formation of a barrier at the electrolyte/steel interface which could prevent the charge transport across the layer.

CHAPTER 5: CONCLUSIONS AND FUTURE WORKS

This thesis reports the synthesis and characterization of three different nanocomposites of conducting polymers and utilized them as anti-corrosion agents for the protection of steel.

5.1 Conclusions

The conclusions on the performance of the synthesized nanocomposites for this research are itemized below:

1. Polypyrrole nanocomposites were synthesized in the presence of TiO_2 and Co-doped TiO_2 nanoparticles (NPs) by an *in situ* chemical oxidative polymerization. The synthesized nanocomposites were utilized as a pigment for anticorrosive coatings. The corrosion performance was analyzed by EIS and potentiodynamic polarization measurements in a solution of 3.5% NaCl solution. The EIS results show that the log |Z| of AISI 1018 coated with Co-doped TiO_2/PPy NTCs and TiO_2/PPy NTCs reached about 8.2 and 6.0 respectively after 30 days of exposure time in 3.5 % NaCl solution. The Co-doped TiO_2/PPy NTCs exhibited better performance in corrosion protection of steel surface than the TiO_2/PPy. The excellent corrosion prevention ability of Co-doped TiO_2/PPy was likely due to the following reasons: pyrrole monomer polymerization in the vicinity of nanoparticles increased the dispersion of PPy, and more dispersion was observed with the PPy prepared in the presence of Co-doped TiO_2 NPs compared to the PPy synthesized in the vicinity of TiO_2 NPs. The corrosion protection of PPy increased with the increase in PPy dispersion in the reaction medium. Also, pyrrole polymerization in the presence of NPs can decrease the size of the PPy thereby increasing the surface contact area of PPy which can interact well with the steel surface. The TEM results confirmed that the size of Co-doped TiO_2/PPy NTCs was smaller than the TiO_2/PPy NTCs, thereby creating more interaction

between the PPy nanotube and the AISI steel surface. Moreover, the OCP values of Co-doped TiO_2/PPy, TiO_2/PPy, PPy NT and steel after 30 days of immersion were -0.209 V, -0.390 V, -0.598 V and -0.795 V respectively. These results confirmed the better performance of the coatings incorporated with Co-doped TiO_2/PPy compared to the coatings incorporated with TiO_2/PPy NTCs and PPy NTs prepared for this experiment for the corrosion protection of steel.

2. This work reports a simple synthetic process of Co-doped TiO_2/GO/PANI NCs by an *in situ* chemical oxidative polymerization of aniline monomer in the presence of Co-doped TiO_2 NPs and GO. The results of the characterization indicate that the integrated nanocomposite comprised of nanoparticles of Co-doped TiO_2, GO sheets and PANI strands. The as-synthesized nanocomposites were used as a pigment for corrosion control. The corrosion protection properties of the nanocomposites were investigated in 3.5% NaCl using electrochemical impedance spectroscopy and potentiodynamic polarization measurements. The EIS results indicated that the log |Z| value for the carbon steel coated with Co-doped TiO_2/PANI NCs is approximately 7.4 for the immersion time of 30 days but increased to 9.2 for the steel coated with Co-doped TiO_2/GO/PANI NCs incorporated butvar for the same immersion time. The coating performance of the PANI nanocomposite incorporated with GO and Co-doped TiO_2 NPs exhibited better corrosion protection properties than the coatings incorporated with Co-doped TiO_2/PANI and bare PANI alone. The excellent performance of these coatings is likely due to the barrier effects, redox properties of PANI and the increased surface area for the liberation of dopants from the incorporation of the nano-size additive. Additionally, the OCP values of Co-doped TiO_2/GO/PANI, Co-doped TiO_2/PANI, PANI, and butvar after one month of immersion time were -0.072 V, -0.552 V, -0.688 V and -0.923 V, respectively.

3. This research reports an easy synthetic process of PANI NCs by an *in situ* chemical oxidative polymerization of aniline monomer in the presence of Zn-doped TiO_2 NPs and GO. The findings from the characterization carried out indicate that the integrated nanocomposite is made up of Zn-doped TiO_2 NPs in anatase phase, GO sheets and PANI strands. The as-prepared nanocomposites were utilized as an agent for corrosion protection of steel. The corrosion protection properties of the nanocomposites were studied in 3.5% NaCl by electrochemical impedance spectroscopy and potentiodynamic polarization measurements. The EIS results revealed that the log |Z| value for the steel coated with PANI/Zn-doped TiO_2 NCs is about 7.15 for the immersion time of 30 days, but increased to 9.01 for the steel coated with PANI/GO/Zn-doped TiO_2 NCs for the same exposure time. The corrosion resistance properties of the PANI nanocomposite incorporated with GO and Co-doped TiO_2 NPs was better than the coatings incorporated with PANI/Zn-doped TiO_2 and bare PANI alone. The excellent performance of these coatings is likely due to the barrier effects, redox properties of PANI and the increased surface area for the liberation of dopants from the incorporation of the agents. Additionally, the OCP values of PANI/GO/Zn-doped TiO_2 NCs, PANI/Zn-doped TiO_2 NCs, PANI, and butvar after 30 days of exposure were -0.115 V, -0.198 V, -0.578 V and -0.875 V, respectively.

5.2 Recommendations for future works

Nanocomposites of conducting polymers can be obtained with conducting polymers when they are prepared by an in-situ chemical polymerization in the presence of appropriate nanoparticles. The increase of the surface area of the polymer can enhance the efficiency of pigments for corrosion control. Synthesis of conducting polymer in the vicinity of nanoparticles and sometimes a reactive self-degraded soft-template can yield

several fine core-shell structures with outstanding properties. Furthermore, by choosing a suitable core in the structure of the core-shell, it is possible to increase the efficiency of the nanocomposites for corrosion control.

REFERENCES

Abbas, H., & Khedr, A. (1995). Influence of chromium on the corrosion behaviour of stainless steels in sulphuric acid containing halide ions. *Anti-Corrosion Methods and Materials, 42*(1), 11-16.

Abdollahi, H., Ershad-Langroudi, A., Salimi, A., & Rahimi, A. (2014). Anticorrosive coatings prepared using epoxy–silica hybrid nanocomposite materials. *Industrial & Engineering Chemistry Research, 53*(27), 10858-10869.

Akhtari Zavareh, M., Mohammed Sarhan, A. A. D., Akhtari Zavareh, P., & Basirun, W. J. (2016). Electrochemical corrosion behavior of carbon steel pipes coated with a protective ceramic layer using plasma and HVOF thermal spray techniques for oil and gas. *Ceramics International, 42*(2, Part B), 3397-3406.

Amand, S., Musiani, M., Orazem, M. E., Pébère, N., Tribollet, B., & Vivier, V. (2013). Constant-phase-element behavior caused by inhomogeneous water uptake in anti-corrosion coatings. *Electrochimica Acta, 87*, 693-700.

Amirudin, A., & Thieny, D. (1995). Application of electrochemical impedance spectroscopy to study the degradation of polymer-coated metals. *Progress in Organic Coatings, 26*(1), 1-28.

Arasi, A. Y., Jeyakumari, J. J. L., Sundaresan, B., Dhanalakshmi, V., & Anbarasan, R. (2009). The structural properties of poly (aniline)—analysis via FTIR spectroscopy. *Spectrochimica Acta Part A: Molecular and Biomolecular Spectroscopy, 74*(5), 1229-1234.

Araujo, W., Margarit, I., Ferreira, M., Mattos, O., & Neto, P. L. (2001). Undoped polyaniline anticorrosive properties. *Electrochimica Acta, 46*(9), 1307-1312.

Armes, S. P. (1987). Optimum reaction conditions for the polymerization of pyrrole by iron (III) chloride in aqueous solution. *Synthetic Metals, 20*(3), 365-371.

Ates, M. (2011). Review study of electrochemical impedance spectroscopy and equivalent electrical circuits of conducting polymers on carbon surfaces. *Progress in Organic Coatings, 71*(1), 1-10.

Athawale, A. A., Kulkarni, M. V., & Chabukswar, V. V. (2002). Studies on chemically synthesized soluble acrylic acid doped polyaniline. *Materials Chemistry and Physics, 73*(1), 106-110.

Atwa, S. M. H. (2010). *The Effect of Vapor Grown Carbon Nanofiber-modified Alkyd Paint Coatings on the Corrosion Behavior of Mild Steel.* Mississippi State University.

Ayad, M. M. (1994a). Influence of HCl on polypyrrole films prepared chemically from ferric chloride. *Journal of Polymer Science Part A: Polymer Chemistry, 32*(1), 9-14.

Ayad, M. M. (1994b). Optimum reaction conditions for polypyrrole film deposition with some iron (III) compounds. *Polymer International, 35*(1), 35-39.

Azim, S. S., Sathiyanarayanan, S., & Venkatachari, G. (2006). Anticorrosive properties of PANI–ATMP polymer containing organic coating. *Progress in Organic Coatings, 56*(2), 154-158.

Bai, X., Tran, T. H., Yu, D., Vimalanandan, A., Hu, X., & Rohwerder, M. (2015). Novel conducting polymer based composite coatings for corrosion protection of zinc. *Corrosion Science, 95*, 110-116.

Bardal, E. (2007). *Corrosion and protection*: Springer Science & Business Media.

Barkade, S. S., Pinjari, D. V., Singh, A. K., Gogate, P. R., Naik, J. B., Sonawane, S. H., . . . Pandit, A. B. (2013). Ultrasound assisted miniemulsion polymerization for preparation of polypyrrole–zinc oxide (PPy/ZnO) functional latex for liquefied petroleum gas sensing. *Industrial & Engineering Chemistry Research, 52*(23), 7704-7712.

Barsoukov, E., & Macdonald, J. R. (2005). *Impedance spectroscopy: theory, experiment, and applications*: John Wiley & Sons, Inc., Hoboken, New Jersey.

Batmanghelich, F., & Ghorbani, M. (2013). Effect of pH and carbon nanotube content on the corrosion behavior of electrophoretically deposited chitosan–hydroxyapatite–carbon nanotube composite coatings. *Ceramics International, 39*(5), 5393-5402.

Bhandari, H., Kumar, S. A., & Dhawan, S. (2012). *Conducting polymer nanocomposites for anticorrosive and antistatic applications* (Vol. 13): INTECH Open Access Publisher.

Bhattacharyya, K., Varma, S., Tripathi, A., Bharadwaj, S., & Tyagi, A. (2008). Effect of vanadia doping and its oxidation state on the photocatalytic activity of TiO_2 for gas-phase oxidation of ethene. *The Journal of Physical Chemistry C, 112*(48), 19102-19112.

Binitha, N. N., Yaakob, Z., & Resmi, R. (2010). Influence of synthesis methods on zirconium doped titania photocatalysts. *Central European Journal of Chemistry, 8*(1), 182-187.

Boeva, Z. A., & Sergeyev, V. (2014). Polyaniline: Synthesis, properties, and application. *Polymer Science Series C, 56*(1), 144-153.

Bonora, P. L., Deflorian, F., & Fedrizzi, L. (1996). Electrochemical impedance spectroscopy as a tool for investigating underpaint corrosion. *Electrochimica Acta, 41*(7), 1073-1082.

Bredas, J. L., & Street, G. B. (1985). Polarons, bipolarons, and solitons in conducting polymers. *Accounts of Chemical Research, 18*(10), 309-315.

Breslin, C. B., Fenelon, A. M., & Conroy, K. G. (2005). Surface engineering: corrosion protection using conducting polymers. *Materials & Design, 26*(3), 233-237.

Burda, C., Chen, X., Narayanan, R., & El-Sayed, M. A. (2005). Chemistry and properties of nanocrystals of different shapes. *Chemical Reviews, 105*(4), 1025-1102.

Byrappa, K., & Adschiri, T. (2007). Hydrothermal technology for nanotechnology. *Progress in Crystal Growth and Characterization of Materials, 53*(2), 117-166.

Byrappa, K., Lokanatha Rai, K., & Yoshimura, M. (2000). Hydrothermal preparation of TiO_2 and photocatalytic degradation of hexachlorocyclohexane and dichlorodiphenyltrichloromethane. *Environmental Technology, 21*(10), 1085-1090.

Cai, W., Piner, R. D., Stadermann, F. J., Park, S., Shaibat, M. A., Ishii, Y., . . . Stoller, M. (2008). Synthesis and solid-state NMR structural characterization of ^{13}C-labeled graphite oxide. *Science, 321*(5897), 1815-1817.

Canobre, S. C., Almeida, D. A., Fonseca, C. P., & Neves, S. (2009). Synthesis and characterization of hybrid composites based on carbon nanotubes. *Electrochimica Acta, 54*(26), 6383-6388.

Castagno, K. R. L., Azambuja, D. S., & Dalmoro, V. (2009). Polypyrrole electropolymerized on aluminum alloy 1100 doped with oxalate and tungstate anions. *Journal of Applied Electrochemistry, 39*(1), 93-100.

Cebada-Ricalde, M. C. (2014). *Synthesis and characterization of PANI-coated VGCNFs and evaluation of its use for corrosion inhibition.* Mississippi State University.

Chan, H., Teo, M., Khor, E., & Lim, C. (1989). Thermal analysis of conducting polymers part I. *Journal of Thermal Analysis, 35*(3), 765-774.

Chandrasekhar, P. (2013). *Conducting polymers, fundamentals and applications: a practical approach*: Springer Science & Business Media.

Chang, C.-H., Huang, T.-C., Peng, C.-W., Yeh, T.-C., Lu, H.-I., Hung, W.-I., . . . Yeh, J.-M. (2012). Novel anticorrosion coatings prepared from polyaniline/graphene composites. *Carbon, 50*(14), 5044-5051.

Chao, T. H., & March, J. (1988). A study of polypyrrole synthesized with oxidative transition metal ions. *Journal of Polymer Science Part A: Polymer Chemistry, 26*(3), 743-753.

Chaudhari, H., & Kelkar, D. (1997). Investigation of structure and electrical conductivity in doped polyaniline. *Polymer International, 42*(4), 380-384.

Chen, S.-A., & Lin, L.-C. (1995). Polyaniline doped by the new class of dopant, ionic salt: structure and properties. *Macromolecules, 28*(4), 1239-1245.

Chen, X., Issi, J. P., Devaux, J., & Billaud, D. (1995). Chemically oxidized polypyrrole: Influence of the experimental conditions on its electrical conductivity and morphology. *Polymer Engineering & Science, 35*(8), 642-647.

Chen, X., & Mao, S. S. (2007). Titanium dioxide nanomaterials: synthesis, properties, modifications, and applications. *Chemical Reviews, 107*(7), 2891-2959.

Cheng, X., Yu, X., & Xing, Z. (2012a). Characterization and mechanism analysis of N doped TiO_2 with visible light response and its enhanced visible activity. *Applied Surface Science, 258*(7), 3244-3248.

Cheng, X., Yu, X., & Xing, Z. (2012b). One-step synthesis of visible, active C N S-tridoped TiO_2 photocatalyst from biomolecule cystine. *Applied Surface Science, 258*(19), 7644-7650.

Chiang, C. K., Fincher Jr, C., Park, Y. W., Heeger, A. J., Shirakawa, H., Louis, E. J., . . . MacDiarmid, A. G. (1977). Electrical conductivity in doped polyacetylene. *Physical Review Letters, 39*(17), 1098.

Choudhury, B., & Choudhury, A. (2012). Luminescence characteristics of cobalt doped TiO_2 nanoparticles. *Journal of Luminescence, 132*(1), 178-184.

Chowdhury, D., Paul, A., & Chattopadhyay, A. (2005). Photocatalytic Polypyrrole− TiO_2− Nanoparticles Composite Thin Film Generated at the Air− Water Interface. *Langmuir, 21*(9), 4123-4128.

Ćirić-Marjanović, G. (2013a). Recent advances in polyaniline composites with metals, metalloids and nonmetals. *Synthetic Metals, 170*, 31-56.

Ćirić-Marjanović, G. (2013b). Recent advances in polyaniline research: Polymerization mechanisms, structural aspects, properties and applications. *Synthetic Metals, 177*, 1-47.

Ćirić-Marjanović, G. (2010). Polyaniline nanostructures. *Nanostructured Conductive Polymers*, 19-98.

Ćirić-Marjanović, G., Trchová, M., & Stejskal, J. (2008). The chemical oxidative polymerization of aniline in water: Raman spectroscopy. *Journal of Raman Spectroscopy, 39*(10), 1375-1387.

Clark, W. J., Ramsey, J. D., McCreery, R. L., & Frankel, G. S. (2002). A galvanic corrosion approach to investigating chromate effects on aluminum alloy 2024-T3. *Journal of The Electrochemical Society, 149*(5), B179-B185.

Cohen, S. (1995). Review: Replacements for chromium pretreatments on aluminum. *Corrosion, 51*(1), 71-78.

Córdoba-Torres, P., Mesquita, T. J., & Nogueira, R. P. (2015). Relationship between the Origin of Constant-Phase Element Behavior in Electrochemical Impedance Spectroscopy and Electrode Surface Structure. *The Journal of Physical Chemistry C, 119*(8), 4136-4147.

Cramer, S. D., & Covino, B. S. (2005). *ASM Handbook Volume 13b: Corrosion: Materials* (Vol. 13): ASM international.

Cramer, S. D., & Covino, B. S. (2006). *Corrosion: Environments and industries* (Vol. 13): ASM International.

Das, T. K., & Prusty, S. (2012). Review on conducting polymers and their applications. *Polymer-Plastics Technology and Engineering, 51*(14), 1487-1500.

de Souza, S., da Silva, J. E. P., de Torresi, S. I. C., Temperini, M. L., & Torresi, R. M. (2001). Polyaniline based acrylic blends for iron corrosion protection. *Electrochemical and Solid-State Letters, 4*(8), B27-B30.

DeBerry, D. W. (1985). Modification of the electrochemical and corrosion behavior of stainless steels with an electroactive coating. *Journal of The Electrochemical Society, 132*(5), 1022-1026.

Deshpande, P. P., Jadhav, N. G., Gelling, V. J., & Sazou, D. (2014). Conducting polymers for corrosion protection: a review. *Journal of Coatings Technology and Research, 11*(4), 473-494.

Deshpande, P. P., & Sazou, D. (2016). *Corrosion protection of metals by intrinsically conducting polymers*: CRC Press.

Despić, A., & Parkhutik, V. P. (1989). Electrochemistry of aluminum in aqueous solutions and physics of its anodic oxide. *Modern Aspects of Electrochemistry No. 20* (pp. 401-503): Springer.

Dhawan, S., & Trivedi, D. (1993). Thin conducting polypyrrole film on insulating surface and its applications. *Bulletin of Materials Science, 16*(5), 371-380.

Di Paola, A., Garcıa-López, E., Ikeda, S., Marcı, G., Ohtani, B., & Palmisano, L. (2002). Photocatalytic degradation of organic compounds in aqueous systems by transition metal doped polycrystalline TiO_2. *Catalysis Today, 75*(1), 87-93.

Diebold, U. (2003). The surface science of titanium dioxide. *Surface Science Reports, 48*(5), 53-229.

do Nascimento, G. M., & Temperini, M. L. (2008). Structure of polyaniline formed in different inorganic porous materials: A spectroscopic study. *European Polymer Journal, 44*(11), 3501-3511.

Dominis, A. J., Spinks, G. M., Kane-Maguire, L. A., & Wallace, G. G. (2002). A de-doping/re-doping study of organic soluble polyaniline. *Synthetic Metals, 129*(2), 165-172.

Dreyer, D. R., Park, S., Bielawski, C. W., & Ruoff, R. S. (2010). The chemistry of graphene oxide. *Chemical Society Reviews, 39*(1), 228-240.

Drobny, J. G. (2012). *Polymers for electricity and electronics: materials, properties, and applications*: John Wiley & Sons, Inc., Hoboken, New Jersey.

Eftekhari, A. (2011). *Nanostructured conductive polymers*: John Wiley & Sons, West Sussex, United Kingdom.

Eisazadeh, H., Spinks, G., & Wallace, G. (1992). *Electrochemical properties of conductive electroactive polymeric colloids.* Paper presented at the Materials forum.

Ezhilselvi, V., Nithin, J., Balaraju, J., & Subramanian, S. (2016). The influence of current density on the morphology and corrosion properties of MAO coatings on AZ31B magnesium alloy. *Surface and Coatings Technology, 288*, 221-229.

Ferreira, C., Domenech, S., & Lacaze, P. (2001). Synthesis and characterization of polypyrrole/TiO_2 composites on mild steel. *Journal of Applied Electrochemistry, 31*(1), 49-56.

Fontana, M. G. (1980). Corrosion science, corrosion engineering, and then what. *Materials Performance, 19*(1), 47-49.

Freund, M. S., & Deore, B. A. (2007). *Self-doped conducting polymers*: John Wiley & Sons Ltd., West Sussex, England.

Gangopadhyay, R., & De, A. (2000). Conducting polymer nanocomposites: a brief overview. *Chemistry of Materials, 12*(3), 608-622.

Ganguli, D. (1992). Sol-gel processing of materials for electronic and related applications. *Bulletin of Materials Science, 15*(5), 421-430.

Gao, W., Alemany, L. B., Ci, L., & Ajayan, P. M. (2009). New insights into the structure and reduction of graphite oxide. *Nature Chemistry, 1*(5), 403-408.

Gaponik, N. P., Talapin, D. V., Rogach, A. L., & Eychmuller, A. (2000). Electrochemical synthesis of CdTe nanocrystal/polypyrrole composites for optoelectronic applications. *Journal of Materials Chemistry, 10*(9), 2163-2166.

Gardini, G. (1973). The oxidation of monocyclic pyrroles. *Advances in Heterocyclic Chemistry, 15*, 67-98.

Gašparac, R., & Martin, C. R. (2001). Investigations of the mechanism of corrosion inhibition by polyaniline. Polyaniline-coated stainless steel in sulfuric acid solution. *Journal of The Electrochemical Society, 148*(4), B138-B145.

Geim, A. K., & Novoselov, K. S. (2007). The rise of graphene. *Nature Materials, 6*(3), 183-191.

Genies, E., Bidan, G., & Diaz, A. (1983). Spectroelectrochemical study of polypyrrole films. *Journal of Electroanalytical Chemistry and Interfacial Electrochemistry, 149*(1), 101-113.

Grgur, B., Elkais, A., Gvozdenović, M., Drmanić, S., Trišović, T. L., & Jugović, B. (2015). Corrosion of mild steel with composite polyaniline coatings using different formulations. *Progress in Organic Coatings, 79*, 17-24.

Günes, S., Neugebauer, H., & Sariciftci, N. S. (2007). Conjugated polymer-based organic solar cells. *Chemical Reviews, 107*(4), 1324-1338.

Guo, N., Liang, Y., Lan, S., Liu, L., Zhang, J., Ji, G., & Gan, S. (2014). Microscale hierarchical three-dimensional flowerlike TiO_2/PANI composite: synthesis, characterization, and its remarkable photocatalytic activity on organic dyes under UV-light and sunlight irradiation. *The Journal of Physical Chemistry C, 118*(32), 18343-18355.

Gupta, S. M., & Tripathi, M. (2012). A review on the synthesis of TiO_2 nanoparticles by solution route. *Central European Journal of Chemistry, 10*(2), 279-294.

Han, C., & Elsenbaumer, R. (1989). Protonic acids: generally applicable dopants for conducting polymers. *Synthetic Metals, 30*(1), 123-131.

Han, M. G., Lee, Y. J., Byun, S. W., & Im, S. S. (2001). Physical properties and thermal transition of polyaniline film. *Synthetic Metals, 124*(2), 337-343.

Han, Y. (2009). Synthesis and characterization of montmorillonite/polypyrrole nanocomposite. *Polymer Composites, 30*(1), 66-69.

Hany, P., Genies, E., & Santier, C. (1989). Polyanilines with covalently bonded alkyl sulfonates as doping agent. Synthesis and properties. *Synthetic Metals, 31*(3), 369-378.

Hao, Y., Liu, F., & Han, E.-H. (2013). Protection of epoxy coatings containing polyaniline modified ultra-short glass fibers. *Progress in Organic Coatings, 76*(4), 571-580.

Hasannejad, H., Shahrabi, T., Jafarian, M., & Rouhaghdam, A. S. (2011). EIS study of nano crystalline Ni-cerium oxide coating electrodeposition mechanism. *Journal of Alloys and Compounds, 509*(5), 1924-1930.

Hasanov, R., & Bilgiç, S. (2009). Monolayer and bilayer conducting polymer coatings for corrosion protection of steel in 1M H_2SO_4 solution. *Progress in Organic Coatings, 64*(4), 435-445.

He, X., Wu, L.-l., Wang, J.-j., Zhang, T., Sun, H., & Shuai, N. (2015). Layer-by-layer assembly deposition of graphene oxide on poly (lactic acid) films to improve the barrier properties. *High Performance Polymers, 27*(3), 318-325.

Heeger, A. J., Kivelson, S., Schrieffer, J., & Su, W.-P. (1988). Solitons in conducting polymers. *Reviews of Modern Physics, 60*(3), 781.

Hosseini, M., Bagheri, R., & Najjar, R. (2011). Electropolymerization of polypyrrole and polypyrrole-ZnO nanocomposites on mild steel and its corrosion protection performance. *Journal of Applied Polymer Science, 121*(6), 3159-3166.

Hu, W., Peng, C., Luo, W., Lv, M., Li, X., Li, D., . . . Fan, C. (2010). Graphene-based antibacterial paper. *ACS Nano, 4*(7), 4317-4323.

Hua, M.-Y., Su, Y.-N., & Chen, S.-A. (2000). Water-soluble self-acid-doped conducting polyaniline: poly (aniline-co-N-propylbenzenesulfonic acid-aniline). *Polymer, 41*(2), 813-815.

Huang, J., & Kaner, R. B. (2004). A general chemical route to polyaniline nanofibers. *Journal of the American Chemical Society, 126*(3), 851-855.

Huang, W.-S., Humphrey, B. D., & MacDiarmid, A. G. (1986). Polyaniline, a novel conducting polymer. Morphology and chemistry of its oxidation and reduction in aqueous electrolytes. *Journal of the Chemical Society, Faraday Transactions 1: Physical Chemistry in Condensed Phases, 82*(8), 2385-2400.

Hummers, W. S., & Offeman, R. E. (1958). Preparation of Graphitic Oxide. *Journal of the American Chemical Society, 80*(6), 1339-1339.

Hurd, J., Ault, J. P., & Barbero, L. (1995). Chromate conversion coating elimination from 500 series armor-grade aluminum. *Metal Finishing, 93*(11), 28-30.

Hussin, M. H., Rahim, A. A., Ibrahim, M. N. M., & Brosse, N. (2015). Improved corrosion inhibition of mild steel by chemically modified lignin polymers from Elaeis guineensis agricultural waste. *Materials Chemistry and Physics, 163*, 201-212.

Ito, S., Murata, K., Teshima, S., Aizawa, R., Asako, Y., Takahashi, K., & Hoffman, B. M. (1998). Simple synthesis of water-soluble conducting polyaniline. *Synthetic Metals, 96*(2), 161-163.

Jadhav, N., Jensen, M. B., & Gelling, V. (2015). Tungstate and vanadate-doped polypyrrole/aluminum flake composite coatings for the corrosion protection of aluminum 2024-T3. *Journal of Coatings Technology and Research, 12*(2), 259-276.

Jadhav, N., Vetter, C. A., & Gelling, V. J. (2013). The effect of polymer morphology on the performance of a corrosion inhibiting polypyrrole/aluminum flake composite pigment. *Electrochimica Acta, 102*, 28-43.

Janata, J., & Josowicz, M. (2003). Conducting polymers in electronic chemical sensors. *Nature materials, 2*(1), 19-24.

Jeon, I.-Y., & Baek, J.-B. (2010). Nanocomposites derived from polymers and inorganic nanoparticles. *Materials, 3*(6), 3654-3674.

Jiang, J., Ai, L., & Li, L. (2009). Multifunctional polypyrrole/strontium hexaferrite composite microspheres: preparation, characterization, and properties. *The Journal of Physical Chemistry B, 113*(5), 1376-1380.

Jiang, M.-Y., Wu, L.-K., Hu, J.-M., & Zhang, J.-Q. (2015a). Silane-incorporated epoxy coatings on aluminum alloy (AA2024). Part 1: Improved corrosion performance. *Corrosion Science, 92*, 118-126.

Jiang, M.-Y., Wu, L.-K., Hu, J.-M., & Zhang, J.-Q. (2015b). Silane-incorporated epoxy coatings on aluminum alloy (AA2024). Part 2: Mechanistic investigations. *Corrosion Science, 92*, 127-135.

Jorcin, J.-B., Orazem, M. E., Pébère, N., & Tribollet, B. (2006). CPE analysis by local electrochemical impedance spectroscopy. *Electrochimica Acta, 51*(8–9), 1473-1479.

Kamaraj, K., Karpakam, V., Sathiyanarayanan, S., & Venkatachari, G. (2010). Electrosysnthesis of poly (aniline-co-m-amino benzoic acid) for corrosion protection of steel. *Materials Chemistry and Physics, 122*(1), 123-128.

Kang, E., Neoh, K., & Tan, K. (1998). Polyaniline: a polymer with many interesting intrinsic redox states. *Progress in Polymer Science, 23*(2), 277-324.

Kar, P. (2013). *Doping in Conjugated Polymers*: Wiley and Sons, Inc. Hoboken, New Jersey.

Karthik, K., Pandian, S. K., Kumar, K. S., & Jaya, N. V. (2010). Influence of dopant level on structural, optical and magnetic properties of Co-doped anatase TiO_2 nanoparticles. *Applied Surface Science, 256*(14), 4757-4760.

Katoch, A., Burkhart, M., Hwang, T., & Kim, S. S. (2012). Synthesis of polyaniline/TiO_2 hybrid nanoplates via a sol–gel chemical method. *Chemical Engineering Journal, 192*, 262-268.

Khanna, P. K., Kulkarni, M. V., Singh, N., Lonkar, S. P., Subbarao, V. V. V. S., & Kasi Viswanath, A. (2006). Synthesis of HCl doped polyaniline–CdS nanocomposite by use of organometallic cadmium precursor. *Materials Chemistry and Physics, 95*(1), 24-28.

Khataee, A. (2009). Photocatalytic removal of CI Basic Red 46 on immobilized TiO_2 nanoparticles: Artificial neural network modelling. *Environmental Technology, 30*(11), 1155-1168.

Khataee, A., & Kasiri, M. B. (2010). Photocatalytic degradation of organic dyes in the presence of nanostructured titanium dioxide: influence of the chemical structure of dyes. *Journal of Molecular Catalysis A: Chemical, 328*(1), 8-26.

Khataee, A., & Mansoori, G. A. (2011). *Nanostructured titanium dioxide materials: properties, preparation and applications*: World Scientific, Singapore.

Kim, B., Park, D., Joo, J., Yu, S., & Lee, S. (2005). Synthesis, characteristics, and field emission of doped and de-doped polypyrrole, polyaniline, poly (3, 4-ethylenedioxythiophene) nanotubes and nanowires. *Synthetic Metals, 150*(3), 279-284.

Kim, C.-S., Moon, B. K., Park, J.-H., Chung, S. T., & Son, S.-M. (2003). Synthesis of nanocrystalline TiO_2 in toluene by a solvothermal route. *Journal of Crystal Growth, 254*(3), 405-410.

Kim, D., Lee, J., Kim, C., Kang, E., & Tan, K. (1995). Protonation and doping behavior of polypyrrole films and powders. *Synthetic Metals, 69*(1), 501-502.

Kim, G.-S., Kim, Y.-S., Seo, H.-K., & Shin, H.-S. (2006). Hydrothermal synthesis of titanate nanotubes followed by electrodeposition process. *Korean Journal of Chemical Engineering, 23*(6), 1037-1045.

Kim, J., Cote, L. J., Kim, F., Yuan, W., Shull, K. R., & Huang, J. (2010). Graphene oxide sheets at interfaces. *Journal of the American Chemical Society, 132*(23), 8180-8186.

Kim, Y. J., Chai, S. Y., & Lee, W. I. (2007). Control of TiO_2 structures from robust hollow microspheres to highly dispersible nanoparticles in a tetrabutylammonium hydroxide solution. *Langmuir, 23*(19), 9567-9571.

Kinlen, P. J., Menon, V., & Ding, Y. (1999). A mechanistic investigation of polyaniline corrosion protection using the scanning reference electrode technique. *Journal of The Electrochemical Society, 146*(10), 3690-3695.

Koch, G. H. (2002). *Historic congressional study: Corrosion costs and preventive strategies in the United States*. NACE International, Houston.

Kofstad, P. (1972). *Nonstoichiometry, diffusion, and electrical conductivity in binary metal oxides* (Vol. 155): Wiley-Interscience, New York.

Kogan, I., Abalyaeva, V., & Gedrovich, G. (1994). Electrochemical synthesis of polyaniline on tantalum and stainless-steel electrodes. *Synthetic Metals, 63*(2), 153-156.

Kolen'ko, Y. V., Kovnir, K. A., Gavrilov, A. I., Garshev, A. V., Meskin, P. E., Churagulov, B. R., . . . Van Tendeloo, G. (2005). Structural, Textural, and Electronic Properties of a Nanosized Mesoporous $Zn_xTi_{1-x}O_{2-x}$ Solid Solution Prepared by a Supercritical Drying Route. *The Journal of Physical Chemistry B, 109*(43), 20303-20309.

Kraljić, M., Mandić, Z., & Duić, L. (2003). Inhibition of steel corrosion by polyaniline coatings. *Corrosion Science, 45*(1), 181-198.

Kulkarni, M. V., Viswanath, A. K., Marimuthu, R., & Seth, T. (2004a). Spectroscopic, transport, and morphological studies of polyaniline doped with inorganic acids. *Polymer Engineering & Science, 44*(9), 1676-1681.

Kulkarni, M. V., Viswanath, A. K., Marimuthu, R., & Seth, T. (2004b). Synthesis and characterization of polyaniline doped with organic acids. *Journal of Polymer Science Part A: Polymer Chemistry, 42*(8), 2043-2049.

Kumar, D., & Sharma, R. (1998). Advances in conductive polymers. *European Polymer Journal, 34*(8), 1053-1060.

Kumar, N. A., Choi, H.-J., Shin, Y. R., Chang, D. W., Dai, L., & Baek, J.-B. (2012). Polyaniline-grafted reduced graphene oxide for efficient electrochemical supercapacitors. *ACS Nano, 6*(2), 1715-1723.

Kuwabata, S., Okamoto, K., & Yoneyama, H. (1988). Conductivity of polypyrrole films doped with aromatic sulphonate derivatives. *Journal of the Chemical Society,*

Faraday Transactions 1: Physical Chemistry in Condensed Phases, 84(7), 2317-2326.

Ladan, M., Basirun, W. J., Kazi, S. N., & Rahman, F. A. (2017). Corrosion protection of AISI 1018 steel using Co-doped TiO_2/polypyrrole nanocomposites in 3.5% NaCl solution. *Materials Chemistry and Physics, 192*, 361-373.

Lai, C., Li, G., Dou, Y., & Gao, X. (2010). Mesoporous polyaniline or polypyrrole/anatase TiO_2 nanocomposite as anode materials for lithium-ion batteries. *Electrochimica Acta, 55*(15), 4567-4572.

Lee, K., Mazare, A., & Schmuki, P. (2014). One-dimensional titanium dioxide nanomaterials: nanotubes. *Chemical Reviews, 114*(19), 9385-9454.

Lenz, D. M., Delamar, M., & Ferreira, C. A. (2003). Application of polypyrrole/TiO_2 composite films as corrosion protection of mild steel. *Journal of Electroanalytical Chemistry, 540*, 35-44.

Li, C., Bai, H., & Shi, G. (2009). Conducting polymer nanomaterials: electrosynthesis and applications. *Chemical Society Reviews, 38*(8), 2397-2409.

Li, D., Müller, M. B., Gilje, S., Kaner, R. B., & Wallace, G. G. (2008). Processable aqueous dispersions of graphene nanosheets. *Nature Nanotechnology, 3*(2), 101-105.

Li, W., Zhang, Q., Zheng, G., Seh, Z. W., Yao, H., & Cui, Y. (2013a). Understanding the Role of Different Conductive Polymers in Improving the Nanostructured Sulfur Cathode Performance. *Nano Letters, 13*(11), 5534-5540.

Li, X. L., Peng, Q., Yi, J. X., Wang, X., & Li, Y. D. (2006). Near monodisperse TiO_2 nanoparticles and nanorods. *Chemistry-a European Journal, 12*(8), 2383-2391.

Li, Y., Lu, D., & Wong, C. (2010). Intrinsically Conducting Polymers (ICPs) *Electrical Conductive Adhesives with Nanotechnologies* (pp. 361-424): Springer.

Li, Y., Yu, Y., Wu, L., & Zhi, J. (2013b). Processable polyaniline/titania nanocomposites with good photocatalytic and conductivity properties prepared via peroxo-titanium complex catalyzed emulsion polymerization approach. *Applied Surface Science, 273*, 135-143.

Lin, H.-K., & Chen, S.-A. (2000). Synthesis of new water-soluble self-doped polyaniline. *Macromolecules, 33*(22), 8117-8118.

Liu, C., Yang, D., Jiao, Y., Tian, Y., Wang, Y., & Jiang, Z. (2013). Biomimetic synthesis of TiO_2–SiO_2–Ag nanocomposites with enhanced visible-light photocatalytic activity. *ACS Applied Materials & Interfaces, 5*(9), 3824-3832.

Liu, J.-M., Sun, L., Hwang, J.-H., & Yang, S. C. (1992). *Novel Template Guided Synthesis of Poly Aniline.* Paper presented at the MRS Proceedings.

Liu, J.-M., & Yang, S. C. (1991). Novel colloidal polyaniline fibrils made by template guided chemical polymerization. *Journal of the Chemical Society, Chemical Communications*(21), 1529-1531.

Liu, J., Hua, L., Li, S., & Yu, M. (2015). Graphene dip coatings: An effective anticorrosion barrier on aluminum. *Applied Surface Science, 327*, 241-245.

Liu, N., Chen, X., Zhang, J., & Schwank, J. W. (2014). A review on TiO_2-based nanotubes synthesized via hydrothermal method: formation mechanism, structure modification, and photocatalytic applications. *Catalysis Today, 225*, 34-51.

Long, Y.-Z., Li, M.-M., Gu, C., Wan, M., Duvail, J.-L., Liu, Z., & Fan, Z. (2011). Recent advances in synthesis, physical properties and applications of conducting polymer nanotubes and nanofibers. *Progress in Polymer Science, 36*(10), 1415-1442.

Loveday, D., Peterson, P., & Rodgers, B. (2004). Evaluation of organic coatings with electrochemical impedance spectroscopy. Part 2: Application of EIS to coatings. *JCT Coatingstech, 1*(10), 88-93.

Lu, H., Zhang, S., Li, W., Cui, Y., & Yang, T. (2017). Synthesis of Graphene Oxide-Based Sulfonated Oligoanilines Coatings for Synergistically Enhanced Corrosion Protection in 3.5% NaCl Solution. *ACS Applied Materials & Interfaces, 9*(4), 4034-4043.

Luo, Q., Bao, L., Wang, D., Li, X., & An, J. (2012). Preparation and strongly enhanced visible light photocatalytic activity of TiO_2 nanoparticles modified by conjugated derivatives of polyisoprene. *The Journal of Physical Chemistry C, 116*(49), 25806-25815.

MacDiarmid, A. G. (1997). Polyaniline and polypyrrole: where are we headed? *Synthetic Metals, 84*(1-3), 27-34.

MacDiarmid, A. G. (2001). "Synthetic metals": A novel role for organic polymers (Nobel lecture). *Angewandte Chemie International Edition, 40*(14), 2581-2590.

Macdonald, D. D. (2006). Reflections on the history of electrochemical impedance spectroscopy. *Electrochimica Acta, 51*(8), 1376-1388.

Macedo, M., Margarit-Mattos, I. C. P., Fragata, F. d. L., Jorcin, J.-B., Pébère, N., & Mattos, O. R. (2009). Contribution to a better understanding of different behaviour patterns observed with organic coatings evaluated by electrochemical impedance spectroscopy. *Corrosion Science, 51*(6), 1322-1327.

Machida, S., Miyata, S., & Techagumpuch, A. (1989). Chemical synthesis of highly electrically conductive polypyrrole. *Synthetic Metals, 31*(3), 311-318.

Maddison, D., & Tansley, T. (1992). Variable range hopping in polypyrrole films of a range of conductivities and preparation methods. *Journal of Applied Physics, 72*(10), 4677-4682.

Madhan Kumar, A., & Rajendran, N. (2013). Electrochemical aspects and in vitro biocompatibility of polypyrrole/TiO_2 ceramic nanocomposite coatings on 316L SS for orthopedic implants. *Ceramics International, 39*(5), 5639-5650.

Mahmoudian, M., Alias, Y., & Basirun, W. (2012). Effect of narrow diameter polyaniline nanotubes and nanofibers in polyvinyl butyral coating on corrosion protective performance of mild steel. *Progress in Organic Coatings, 75*(4), 301-308.

Mahmoudian, M., Alias, Y., Basirun, W., & Ebadi, M. (2013). Effects of different polypyrrole/TiO_2 nanocomposite morphologies in polyvinyl butyral coatings for preventing the corrosion of mild steel. *Applied Surface Science, 268*, 302-311.

Mahmoudian, M., Basirun, W., & Alias, Y. (2011a). Synthesis and characterization of poly (N-methylpyrrole)/TiO_2 composites on steel. *Applied Surface Science, 257*(8), 3702-3708.

Mahmoudian, M., Basirun, W., & Alias, Y. (2011b). Synthesis of polypyrrole/Ni-doped TiO_2 nanocomposites (NCs) as a protective pigment in organic coating. *Progress in Organic Coatings, 71*(1), 56-64.

Mahmoudian, M., Basirun, W., Alias, Y., & Ebadi, M. (2011c). Synthesis and characterization of polypyrrole/Sn-doped TiO_2 nanocomposites (NCs) as a protective pigment. *Applied Surface Science, 257*(20), 8317-8325.

Majumdar, S., Saikia, U., & Mahanta, D. (2015). Polyaniline-Coated Filter Papers: Cost Effective Hybrid Materials for Adsorption of Dyes. *Journal of Chemical & Engineering Data, 60*(11), 3382-3391.

Mansoori, G. A., Bastami, T. R., Ahmadpour, A., & Eshaghi, Z. (2008). Environmental application of nanotechnology. *Annual Review of Nano Research, 2*(2), 1-73.

Merisalu, M., Kahro, T., Kozlova, J., Niilisk, A., Nikolajev, A., Marandi, M., . . . Sammelselg, V. (2015). Graphene–polypyrrole thin hybrid corrosion resistant coatings for copper. *Synthetic Metals, 200*, 16-23.

Mi, H., Zhang, X., Yang, S., Ye, X., & Luo, J. (2008). Polyaniline nanofibers as the electrode material for supercapacitors. *Materials Chemistry and Physics, 112*(1), 127-131.

Michalik, A., & Rohwerder, M. (2005). Conducting polymers for corrosion protection: a critical view. *Zeitschrift für Physikalische Chemie, 219*(11/2005), 1547-1559.

Ming, H. N. (2011). Fabrication and characterization of graphene hydrogel via hydrothermal approach as a scaffold for preliminary study of cell growth. *International journal of nanomedicine, 6*.

Moliton, A., & Hiorns, R. C. (2004). Review of electronic and optical properties of semiconducting π-conjugated polymers: applications in optoelectronics. *Polymer International, 53*(10), 1397-1412.

Moret, M. P., Zallen, R., Vijay, D. P., & Desu, S. B. (2000). Brookite-rich titania films made by pulsed laser deposition. *Thin Solid Films, 366*(1), 8-10.

Mott, N. F., & Davis, E. A. (2012). *Electronic processes in non-crystalline materials*: OUP Oxford.

Mugundan, S., Rajamannan, B., Viruthagiri, G., Shanmugam, N., Gobi, R., & Praveen, P. (2015). Synthesis and characterization of undoped and cobalt-doped TiO_2 nanoparticles via sol–gel technique. *Applied Nanoscience, 5*(4), 449-456.

Narayana, R. L., Matheswaran, M., Aziz, A. A., & Saravanan, P. (2011). Photocatalytic decolourization of basic green dye by pure and Fe, Co doped TiO_2 under daylight illumination. *Desalination, 269*(1), 249-253.

Navío, J. A., Colón, G., Macías, M., Real, C., & Litter, M. I. (1999). Iron-doped titania semiconductor powders prepared by a sol–gel method. Part I: synthesis and characterization. *Applied Catalysis A: General, 177*(1), 111-120.

Neupane, M. P., Lee, S., Kang, J., Park, I. S., Bae, T. S., & Lee, M. H. (2015). Surface characterization and corrosion behavior of silanized magnesium coated with graphene for biomedical application. *Materials Chemistry and Physics, 163*, 229-235.

Noufi, R., Nozik, A. J., White, J., & Warren, L. F. (1982). Enhanced stability of photoelectrodes with electrogenerated polyaniline films. *Journal of The Electrochemical Society, 129*(10), 2261-2265.

Olad, A., Barati, M., & Shirmohammadi, H. (2011). Conductivity and anticorrosion performance of polyaniline/zinc composites: investigation of zinc particle size and distribution effect. *Progress in Organic Coatings, 72*(4), 599-604.

Paliwoda-Porebska, G., Stratmann, M., Rohwerder, M., Potje-Kamloth, K., Lu, Y., Pich, A. Z., & Adler, H.-J. (2005). On the development of polypyrrole coatings with self-healing properties for iron corrosion protection. *Corrosion Science, 47*(12), 3216-3233.

Paredes, J., Villar-Rodil, S., Martínez-Alonso, A., & Tascon, J. (2008). Graphene oxide dispersions in organic solvents. *Langmuir, 24*(19), 10560-10564.

Park, S., & Ruoff, R. S. (2009). Chemical methods for the production of graphenes. *Nature Nanotechnology, 4*(4), 217-224.

Passiniemi, P., & Väkiparta, K. (1995). Characterizaton of polyaniline blends with AC impedance measurements. *Synthetic Metals, 69*(1), 237-238.

Pawar, S., Patil, S., Mane, A., Raut, B., & Patil, V. (2009). Growth, characterization and gas sensing properties of polyaniline thin films. *Arch Appl Sci Res, 1*(2), 109-114.

Pawar, S. G., Patil, S. L., Chougule, M. A., Mane, A. T., Jundale, D. M., & Patil, V. B. (2010). Synthesis and Characterization of Polyaniline:TiO_2 Nanocomposites.

International Journal of Polymeric Materials and Polymeric Biomaterials, 59(10), 777-785.

Pei, S., & Cheng, H.-M. (2012). The reduction of graphene oxide. *Carbon, 50*(9), 3210-3228.

Pour-Ali, S., Dehghanian, C., & Kosari, A. (2015). Corrosion protection of the reinforcing steels in chloride-laden concrete environment through epoxy/polyaniline–camphorsulfonate nanocomposite coating. *Corrosion Science, 90*, 239-247.

Pour-Ali, S., Kiani-Rashid, A., Babakhani, A., & Davoodi, A. (2016). Enhanced protective properties of epoxy/polyaniline-camphorsulfonate nanocomposite coating on an ultrafine-grained metallic surface. *Applied Surface Science, 376*, 121-132.

Przyłuski, J., Zagorska, M., Proń, A., Kucharski, Z., & Suwalski, J. (1987). Synthesis and characterization of conducting polypyrrole-containing iron complexes. *Journal of Physics and Chemistry of Solids, 48*(7), 635-640.

Qi, X., Vetter, C., Harper, A. C., & Gelling, V. J. (2008). Electrochemical investigations into polypyrrole/aluminum flake pigmented coatings. *Progress in Organic Coatings, 63*(3), 345-351.

Qian, Y., Chen, Q., Chen, Z., Fan, C., & Zhou, G. (1993). Preparation of ultrafine powders of TiO_2 by hydrothermal H_2O_2 oxidation starting from metallic Ti. *Journal of Materials Chemistry, 3*(2), 203-205.

Qiu, S., Chen, C., Cui, M., Li, W., Zhao, H., & Wang, L. (2017). Corrosion protection performance of waterborne epoxy coatings containing self-doped polyaniline nanofiber. *Applied Surface Science, 407*, 213-222.

Racicot, R., Clark, R., Liu, H., Yang, S., Alias, M., & Brown, R. (1995). *Anti-corrosion studies of novel conductive polymer coatings on aluminum alloys.* Paper presented at the MRS Proceedings.

Racicot, R., Yang, S., & Brown, R. (1997). *Corrosion protection comparison of a chromate conversion coating to a novel conductive polymer coating on aluminum alloys*. NACE International, Houston, Tx (United States).

Radhakrishnan, S., Siju, C., Mahanta, D., Patil, S., & Madras, G. (2009). Conducting polyaniline–nano-TiO_2 composites for smart corrosion resistant coatings. *Electrochimica Acta, 54*(4), 1249-1254.

Ramezanzadeh, B., Niroumandrad, S., Ahmadi, A., Mahdavian, M., & Moghadam, M. M. (2016). Enhancement of barrier and corrosion protection performance of an epoxy coating through wet transfer of amino functionalized graphene oxide. *Corrosion Science, 103*, 283-304.

Ranka, P., Sethi, V., & Contractor, A. Q. (2016). Characterizing the oxidation level of polyaniline (PANI) at the interface of PANI/TiO_2 nanoparticles under white light illumination. *Thin Solid Films, 615*, 44-55.

Rapi, S., Bocchi, V., & Gardini, G. P. (1988). Conducting polypyrrole by chemical synthesis in water. *Synthetic Metals, 24*(3), 217-221.

Revie, R. W. (2008). *Corrosion and corrosion control*: John Wiley & Sons, Inc., Hoboken, New Jersey.

Rohwerder, M. (2009). Conducting polymers for corrosion protection: a review. *International Journal of Materials Research, 100*(10), 1331-1342.

Sabouri, M., Shahrabi, T., Faridi, H. R., & Hosseini, M. G. (2009). Polypyrrole and polypyrrole–tungstate electropolymerization coatings on carbon steel and evaluating their corrosion protection performance via electrochemical impedance spectroscopy. *Progress in Organic Coatings, 64*(4), 429-434.

Sato, N. (1998). *Electrochemistry at metal and semiconductor electrodes*: Elsevier Science B.V., Amsterdam, The Netherlands.

Sazou, D., Kourouzidou, M., & Pavlidou, E. (2007). Potentiodynamic and potentiostatic deposition of polyaniline on stainless steel: Electrochemical and structural studies for a potential application to corrosion control. *Electrochimica Acta, 52*(13), 4385-4397.

Sedriks, A. J. (1996). *Corrosion of stainless steel, 2. edition*: John Wiley and Sons, Inc., New York, NY (United States).

Shabani Shayeh, J., Ehsani, A., Ganjali, M. R., Norouzi, P., & Jaleh, B. (2015). Conductive polymer/reduced graphene oxide/Au nanoparticles as efficient composite materials in electrochemical supercapacitors. *Applied Surface Science, 353*, 594-599.

Shaw, B. A., & Kelly, R. G. (2006). What is corrosion? *Electrochemical Society Interface, 15*(1), 24-26.

Shen, J., Yan, B., Shi, M., Ma, H., Li, N., & Ye, M. (2011). One step hydrothermal synthesis of TiO_2-reduced graphene oxide sheets. *Journal of Materials Chemistry, 21*(10), 3415-3421.

Shen, S., Wang, X., Chen, T., Feng, Z., & Li, C. (2014). Transfer of Photoinduced Electrons in Anatase–Rutile TiO_2 Determined by Time-Resolved Mid-Infrared Spectroscopy. *The Journal of Physical Chemistry C, 118*(24), 12661-12668.

Shimidzu, T., Ohtani, A., & Honda, K. (1988). Charge-controllable poly pyrrole/poly electrolyte composite membranes: Part III. Electrochemical deionization system constructed by anion-exchangeable and cation-exchangeable polypyrrole electrodes. *Journal of Electroanalytical Chemistry and Interfacial Electrochemistry, 251*(2), 323-337.

Shirakawa, H., Louis, E. J., MacDiarmid, A. G., Chiang, C. K., & Heeger, A. J. (1977). Synthesis of electrically conducting organic polymers: halogen derivatives of polyacetylene,(CH)x. *Journal of the Chemical Society, Chemical Communications*(16), 578-580.

Singh, R., Narula, A. K., Tandon, R., Mansingh, A., & Chandra, S. (1996). Mechanism of charge transport in polypyrrole, poly (N-methyl pyrrole) and their copolymers. *Journal of applied physics, 79*(3), 1476-1480.

Singh, V., Joung, D., Zhai, L., Das, S., Khondaker, S. I., & Seal, S. (2011). Graphene based materials: past, present and future. *Progress in materials science, 56*(8), 1178-1271.

Skotheim, T. A. (1997). *Handbook of conducting polymers*: CRC press.

Sōmiya, S., & Roy, R. (2000). Hydrothermal synthesis of fine oxide powders. *Bulletin of Materials Science, 23*(6), 453-460.

Sonawane, R., Kale, B., & Dongare, M. (2004). Preparation and photo-catalytic activity of Fe-TiO_2 thin films prepared by sol–gel dip coating. *Materials Chemistry and Physics, 85*(1), 52-57.

Sookhakian, M., Amin, Y., Basirun, W., Tajabadi, M., & Kamarulzaman, N. (2014). Synthesis, structural, and optical properties of type-II ZnO–ZnS core–shell nanostructure. *Journal of Luminescence, 145*, 244-252.

Sotzing, G. A., Reynolds, J. R., Katritzky, A. R., Soloducho, J., Belyakov, S., & Musgrave, R. (1996). Poly [bis (pyrrol-2-yl) arylenes]: Conducting polymers from low oxidation potential monomers based on pyrrole via electropolymerization. *Macromolecules, 29*(5), 1679-1684.

Spinks, G. M., Dominis, A. J., Wallace, G. G., & Tallman, D. E. (2002). Electroactive conducting polymers for corrosion control. *Journal of Solid State Electrochemistry, 6*(2), 85-100.

Stejskal, J., Sapurina, I., & Trchová, M. (2010). Polyaniline nanostructures and the role of aniline oligomers in their formation. *Progress in Polymer Science, 35*(12), 1420-1481.

Stejskal, J., Sapurina, I., Trchová, M., & Konyushenko, E. N. (2008). Oxidation of aniline: polyaniline granules, nanotubes, and oligoaniline microspheres. *Macromolecules, 41*(10), 3530-3536.

Stejskal, J., & Trchová, M. (2012). Aniline oligomers versus polyaniline. *Polymer International, 61*(2), 240-251.

Stenger-Smith, J. D. (1998). Intrinsically electrically conducting polymers. Synthesis, characterization, and their applications. *Progress in Polymer Science, 23*(1), 57-79.

Stir, M., Traykova, T., Nicula, R., Burkel, E., Baehtz, C., Knapp, M., & Lathe, C. (2003). In situ high-pressure and high-temperature diffraction experiments on pure and Ag-doped TiO_2 nanopowders. *Nuclear Instruments and Methods in Physics Research Section B: Beam Interactions with Materials and Atoms, 199*, 59-63.

Strandwitz, N. C., Nonoguchi, Y., Boettcher, S. W., & Stucky, G. D. (2010). In situ photopolymerization of pyrrole in mesoporous TiO_2. *Langmuir, 26*(8), 5319-5322.

Su, H., Wang, T., Zhang, S., Song, J., Mao, C., Niu, H., . . . Tian, Y. (2012). Facile synthesis of polyaniline/TiO_2/graphene oxide composite for high performance supercapacitors. *Solid State Sciences, 14*(6), 677-681.

Su, W.-P., Schrieffer, J., & Heeger, A. (1980). Soliton excitations in polyacetylene. *Physical Review B, 22*(4), 2099.

Sun, Q., Schork, F. J., & Deng, Y. (2007). Water-based polymer/clay nanocomposite suspension for improving water and moisture barrier in coating. *Composites Science and Technology, 67*(9), 1823-1829.

Tallman, D. E., Spinks, G., Dominis, A., & Wallace, G. G. (2002). Electroactive conducting polymers for corrosion control. *Journal of Solid State Electrochemistry, 6*(2), 73-84.

Thompson, N. G., Yunovich, M., & Dunmire, D. (2007). Cost of corrosion and corrosion maintenance strategies. *Corrosion Reviews, 25*(3-4), 247-262.

Tripathi, S., Kumar, A., & Hashmi, S. (2006). Electrochemical redox supercapacitors using PVdF-HFP based gel electrolytes and polypyrrole as conducting polymer electrode. *Solid State Ionics, 177*(33), 2979-2985.

Troch-Nagels, G., Winand, R., Weymeersch, A., & Renard, L. (1992). Electron conducting organic coating of mild steel by electropolymerization. *Journal of Applied Electrochemistry, 22*(8), 756-764.

Tseng, I.-H., Chang, W.-C., & Wu, J. C. (2002). Photoreduction of CO_2 using sol–gel derived titania and titania-supported copper catalysts. *Applied Catalysis B: Environmental, 37*(1), 37-48.

Tseng, I.-H., Wu, J. C., & Chou, H.-Y. (2004). Effects of sol–gel procedures on the photocatalysis of Cu/TiO_2 in CO_2 photoreduction. *Journal of Catalysis, 221*(2), 432-440.

Twite, R., & Bierwagen, G. (1998). Review of alternatives to chromate for corrosion protection of aluminum aerospace alloys. *Progress in Organic Coatings, 33*(2), 91-100.

Vakili, H., Ramezanzadeh, B., & Amini, R. (2015). The corrosion performance and adhesion properties of the epoxy coating applied on the steel substrates treated by cerium-based conversion coatings. *Corrosion Science, 94*, 466-475.

Venison, J. (1973). Structural Steel Painting: The International Decorative Paints. *Allen Devices and Co., Ltd., Bristol, England*, 5-6.

Walker, J. A., Warren, L., & Witucki, E. (1988). New chemically prepared conducting "pyrrole blacks". *Journal of Polymer Science Part A: Polymer Chemistry, 26*(5), 1285-1294.

Wang, H., Hao, Q., Yang, X., Lu, L., & Wang, X. (2009). Graphene oxide doped polyaniline for supercapacitors. *Electrochemistry Communications, 11*(6), 1158-1161.

Wang, L.-X., Li, X.-G., & Yang, Y.-L. (2001). Preparation, properties and applications of polypyrroles. *Reactive and Functional Polymers, 47*(2), 125-139.

Wang, X.-H., Wang, L.-X., Jing, X.-B., & Wang, F.-S. (1995). Synthesis and characterization of chlorinated polyaniline. *Synthetic Metals, 69*(1), 149-150.

Wang, X., Zhuang, J., Peng, Q., & Li, Y. (2005). A general strategy for nanocrystal synthesis. *Nature, 437*(7055), 121-124.

Wattanawikkam, C., & Pecharapa, W. (2015). Synthesis and Characterization of Zn-Doped TiO_2 Nanoparticles via Sonochemical Method. *Integrated Ferroelectrics, 165*(1), 167-175.

Wei, H., Wang, Y., Guo, J., Shen, N. Z., Jiang, D., Zhang, X., . . . Shao, L. (2015). Advanced micro/nanocapsules for self-healing smart anticorrosion coatings. *Journal of Materials Chemistry A, 3*(2), 469-480.

Wei, Y., Sun, Y., & Tang, X. (1989). Autoacceleration and kinetics of electrochemical polymerization of aniline. *The Journal of Physical Chemistry, 93*(12), 4878-4881.

Wen, B.-M., Liu, C.-Y., & Liu, Y. (2005a). Solvothermal synthesis of ultralong single-crystalline TiO_2 nanowires. *New Journal of Chemistry, 29*(7), 969-971.

Wen, B., Liu, C., & Liu, Y. (2005b). Bamboo-shaped Ag-doped TiO_2 nanowires with heterojunctions. *Inorganic Chemistry, 44*(19), 6503-6505.

Wessling, B. (1994). Passivation of metals by coating with polyaniline: corrosion potential shift and morphological changes. *Advanced Materials, 6*(3), 226-228.

Wessling, B. (1996). Corrosion prevention with an organic metal (polyaniline): surface ennobling, passivation, corrosion test results. *Materials and Corrosion, 47*(8), 439-445.

Wong, C. L., Tan, Y. N., & Mohamed, A. R. (2011). A review on the formation of titania nanotube photocatalysts by hydrothermal treatment. *Journal of Environmental Management, 92*(7), 1669-1680.

Wu, J.-M., Zhang, T.-W., Zeng, Y.-W., Hayakawa, S., Tsuru, K., & Osaka, A. (2005). Large-scale preparation of ordered titania nanorods with enhanced photocatalytic activity. *Langmuir, 21*(15), 6995-7002.

Wu, J. C.-S., & Chen, C.-H. (2004). A visible-light response vanadium-doped titania nanocatalyst by sol–gel method. *Journal of Photochemistry and Photobiology A: Chemistry, 163*(3), 509-515.

Xie, K., Li, J., Lai, Y., Zhang, Z. a., Liu, Y., Zhang, G., & Huang, H. (2011). Polyaniline nanowire array encapsulated in titania nanotubes as a superior electrode for supercapacitors. *Nanoscale, 3*(5), 2202-2207.

Yan, J., Feng, S., Lu, H., Wang, J., Zheng, J., Zhao, J., . . . Zhu, Z. (2010a). Alcohol induced liquid-phase synthesis of rutile titania nanotubes. *Materials Science and Engineering: B, 172*(2), 114-120.

Yan, M., Vetter, C. A., & Gelling, V. J. (2010b). Electrochemical investigations of polypyrrole aluminum flake coupling. *Electrochimica Acta, 55*(20), 5576-5583.

Yan, M., Vetter, C. A., & Gelling, V. J. (2013). Corrosion inhibition performance of polypyrrole Al flake composite coatings for Al alloys. *Corrosion Science, 70*, 37-45.

Yang, S., & Gao, L. (2006). Fabrication and shape-evolution of nanostructured TiO_2 via a sol–solvothermal process based on benzene–water interfaces. *Materials Chemistry and Physics, 99*(2), 437-440.

Yin, K., & Lu, L. (2003). Parametric study on the electrochemical impedance spectroscopy of organic-coated steels in hydrochloric acid solutions. *Journal of Coatings Technology, 75*(941), 65-72.

Yoon, S.-B., Yoon, E.-H., & Kim, K.-B. (2011). Electrochemical properties of leucoemeraldine, emeraldine, and pernigraniline forms of polyaniline/multi-wall carbon nanotube nanocomposites for supercapacitor applications. *Journal of Power Sources, 196*(24), 10791-10797.

Yuan, R., Wu, S., Wang, B., Liu, Z., Mu, L., Ji, T., . . . Zhu, J. (2016a). Superamphiphobicity and electroactivity enabled dual physical/chemical protections in novel anticorrosive nanocomposite coatings. *Polymer, 85*, 37-46.

Yuan, X., Yue, Z., Chen, X., Wen, S., Li, L., & Feng, T. (2015). EIS study of effective capacitance and water uptake behaviors of silicone-epoxy hybrid coatings on mild steel. *Progress in Organic Coatings, 86*, 41-48.

Yuan, X., Yue, Z. F., Liu, Z. Q., Wen, S. F., Li, L., & Feng, T. (2016b). Effect of siloxane-modified polyacrylate on water uptake and anticorrosion mechanism of silicone–epoxy coatings. *Journal of Coatings Technology and Research, 13*(1), 123-132.

Zallen, R., & Moret, M. (2006). The optical absorption edge of brookite TiO_2. *Solid State Communications, 137*(3), 154-157.

Zarras, P., & Stenger-Smith, J. (2014). *Electroactive polymer (EAP) coatings for corrosion protection of metals*: Woodhead Publishing: Cambridge, UK.

Zeybek, B., Aksun, E., & Üğe, A. (2015). Investigation of corrosion protection performance of poly (N-methylpyrrole)-dodecylsulfate/multi-walled carbon nanotubes composite coatings on the stainless steel. *Materials Chemistry and Physics, 163*, 11-23.

Zhang, R. B., & Gao, L. (2002). *Synthesis of nanosized TiO_2 by hydrolysis of alkoxide titanium in micelles.* Paper presented at the Key Engineering Materials.

Zhong, C., Tang, X., & Cheng, Y. (2008). Corrosion of steel under the defected coating studied by localized electrochemical impedance spectroscopy. *Electrochimica Acta, 53*(14), 4740-4747.

Zhu, J., Wei, S., Zhang, L., Mao, Y., Ryu, J., Mavinakuli, P., . . . Guo, Z. (2010a). Conductive polypyrrole/tungsten oxide metacomposites with negative permittivity. *The Journal of Physical Chemistry C, 114*(39), 16335-16342.

Zhu, M., Wang, R., Chen, C., Zhang, H. B., & Zhang, G. J. (2017). Comparison of corrosion behavior of Ti_3SiC_2 and Ti_3AlC_2 in NaCl solutions with Ti. *Ceramics International, 43*(7), 5708-5714.

Zhu, Y., Murali, S., Cai, W., Li, X., Suk, J. W., Potts, J. R., & Ruoff, R. S. (2010b). Graphene and graphene oxide: synthesis, properties, and applications. *Advanced Materials, 22*(35), 3906-3924.

LIST OF PUBLICATIONS AND PAPERS PRESENTED

JOURNAL ARTICLES (Published/Accepted)

1. Basirun, W. J., Saeed, I. M., Ghadimi, H., **Ladan, M**., Mahmoudian, M. R., Ebadi, M., . . . Endut, Z. (2016). Lead Corrosion and Formation of Lead Oxides from a Lead-air Cell in Methanesulfonic Acid. *Journal of New Materials for Electrochemical Systems, 19*(4).
2. **Ladan, M**., Basirun, W. J., Kazi, S. N., & Rahman, F. A. (2017). Corrosion protection of AISI 1018 steel using Co-doped TiO_2/Polypyrrole nanocomposites in 3.5% NaCl solution. *Materials Chemistry and Physics*, 192, 361-373

CONFERENCE PAPER

Magaji Ladan, Wan Jeffrey Basirun, Kazi Salim Newaz, Shehu Habibu and Muntaka Dahiru. POLYPYRROLE NANOCOMPOSITES FOR CORROSION CONTROL. 5th International Science Postgraduate Conference 2017. 7-8 March| Pulai Springs Resort, Johor Bahru, Malaysia.